Master Thesis

Feasibility of semi-artificial photosynthesis

carried out for the purpose of obtaining the degree of

Diplom-Ingenieur (Dipl. – Ing or DI)

submitted at TU Wien

Faculty of Mechanical and Industrial Engineering

by

Maximilian MEIßNITZER, BSc

Matr. No.: 01426382

under the supervision of

Univ. Prof. Dipl.-Ing. Dr.nat.techn. Oliver Spadiut

Institute of Chemical, Environmental and Bioscience Engineering,

Research Unit Biochemical Engineering

DATE, PLACE

SIGNATURE

This work has been supported by VERBUND AG. within the framework of the VERBUND X ACCELERATOR program.

I confirm, that the printing of this thesis requires the approval of the examination board.

Affidavit

I declare in lieu of oath, that I wrote this thesis and carried out the associated research myself, using only the literature cited in this volume. If text passages from sources are used literally, they are marked as such.

I confirm that this work is original and has not been submitted for examination elsewhere, nor is it currently under consideration for a thesis elsewhere.

I acknowledge that the submitted work will be checked electronically-technically using suitable and state-of-the-art means (plagiarism detection software). On the one hand, this ensures that the submitted work was prepared according to the high-quality standards within the applicable rules to ensure good scientific practice "Code of Conduct" at the TU Wien. On the other hand, a comparison with other student theses avoids violations of my personal copyright.

PLACE AN DATE	SIGNATURE

Kurzfassung

Grüner Wasserstoff, erzeugt mittels erneuerbarer Energien, wird eine Schlüsselrolle in der Dekarbonisierung einer Reihe von industriellen Zweigen einnehmen. Da erneuerbarer Strom Mangelware ist, steigt zunehmend das Interesse an photokatalytischen Wasserstoff aus Wasserzerlegung. In 2020 schlugen Pannwitz et al. einen neuen biomimetischen Ansatz vor, wobei das Photosystem aus Pflanzen oder Algen gemeinsam mit einer Hydrogenase in eine Doppellipidschicht eingebracht wird, um einen biobasierten Photokatalysator zur Wasserspaltung zu konstruieren[1]. Jedoch sind konventionelle Phospholipide, unter hohen Temperaturen, niedrigen pH-Werten und im oxidativen Milieu instabil – Bedingungen typisch für photokatalyische Wasserstofferzeugung. Diese Arbeit beschreibt einen verbesserten Ansatz für ein halbsynthetisches photosynthetisches System, basierend auf stabileren photoaktiven Tetraederlipid-Liposomen – PhotoSomen. Das Ziel dieser Arbeit besteht in einer Machbarkeitsstudie mit einer Kostenschätzung für den Scale-up einer semisynthetischen Wasserstoff Produktion basierend auf dem PhotoSome Photokatalysator.

Eine Übersicht über die Wasserstoff Wertschöpfungskette mit aktuellen und zukünftigen Wasserstoffbedarf, Standards und Anforderungen gemeinsam mit einem Vergleich von, im speziellen grünen, Wasserstoffproduktionsmethoden in Bezug auf Technologie - Reifegrad und Wirtschaftlichkeit mit einem Fokus auf solaren und photokatalytischen Wasserstoff wird präsentiert.

PhotoSomen werden beschrieben und eine Abschätzung über Stabilitäten, Limitation und Optionen der Hauptkomponenten, Photosensitizer, Ladungsträger und katalytischen Zentrum abgegeben. Durch diesen Einblick wurde ein sicherer Gastrennprozess des explosiven Knallgases basierend auf Inertisierung durch Stickstoff erarbeitet und ein Basic Prozessdesign mit einer Analyse aller Unit Operationen durchgeführt. Für die Skalierung wurden 2 Konzepte, eines basierende auf einer 2-stufigen Gaspermeation mit nachgeschalteter Druckwechseladsorption (PSA-KONZEPT) und ein zweites basierend auf einem hypothetischen elektrochemischen Wasserstoffkompressor (EHC-KONZEPT), mit einer täglichen Wasserstoffproduktion vergleichbar zu einem 1 MW Elektrolyseur betrachtet. Systeme ausschließlich basierend auf Druckwechseladsorption oder cryogene Gastrennung wurden aufgrund der niedrigen Wasserstoffkonzentration durch die Verdünnung im Feed Gasstrom vorab verworfen. Da noch keine elektrochemische Trennung via EHC von einem verdünnten Knallgas in der Literatur beschrieben wurde, wurde eine Trennung eines H_2 - O_2 - CO_2 Gasgemisches untersucht. Dabei konnten bei einem Potential von 1 V, 15,5% des Wasserstoffs mit einem Energieaufwand von 33,3 kWh/kg H_2, äquivalent zu 100,07% des unteren Heizwerts von H_2 abgetrennt werden. An den Current Collector Platten wurde starke Oxidation beobachtet. Basierend auf einer 7% Solar to Hydrogen Effizienz und einer Lebensdauer der PhotoSomen von 6 Monaten, würde das System ca. 80000 m^2 an Reaktorfläche benötigen. Das PSA-Konzept erreicht Wasserstoff Produktionskosten von 41,16 €/kgH_2 und das EHC-Konzept 30,49 €/kgH_2 bei einer Tagesproduktion von 483 kg. Der Leistungsbedarf für das PSA-Konzept beträgt 5,429 MW und 3,532 MW für das EHC – KONZEPT. Damit wird Wasserstoff ohne Netto-Energiegewinn erzeugt. Die größten Herausforderungen für einen kosteneffizienten PhotoSome Prozess sind der hohe Energiebedarf der Gastrennung, die hohen Lipidkosten und der Edelstahlkosten der Photoreaktor Panele. Die Unstetigkeit der Sonnenstrahlung, Temperaturen unterhalb des Gefrierpunkts und das reale Verhalten der Photosomen sind offene Fragen. Ein suspendiertes Einzelkatalysator-PhotoSome Wasserstoffproduktionssystem ist damit nicht wirtschaftlich. Weitere Arbeiten sollten den Fokus auf die Synthese von höherwertigen Produkten wie Azetat und Ameisensäure mittels PhotoSomen setzen.

Abstract

Green hydrogen, produced from renewables, will play a key role in decarbonization in a wide range of industries. As renewables remain in short supply, hydrogen from photocatalytic water splitting is gaining more interest as an alternative. Pannwitz et al. proposed 2020 a novel approach by mimicking nature and embedding photosystems and hydrogenase in artificial bilipid layers for hydrogen production[1]. However, conventional phospholipids are unstable at high temperatures, low pH and oxidative conditions – conditions that arise during water splitting. This paper proposes a new approach for this semi-artificial photosynthetic system (SAPS) based on more stable photosynthetic tetrahedral lipid (TEL) liposomes – PhotoSomes. The goal of this thesis is a feasibility study for a potential scale-up of the semi-artificial photosynthetic particulate, suspended, fully biological, lipid-based PhotoSome hydrogen production process. An overview of the H_2 value chain with current and future H_2 demand, standards and requirements is presented. H_2 production methods, especially green H_2 methods have been described and compared on their level of development and cost-effectiveness with a focus on solar H_2 and photocatalytic production methods. A holistic review of publications on H_2-producing semi-artificial photosynthetic photocatalytic systems has been written.

The PhotoSomes are described and studies about stability, limitations and options for the main components photosensitizer, charge carrier and catalytic center are given. Based on this insight a safe separation approach for the potentially explosive oxyhydrogen gas mixture based on dilution by nitrogen was developed. A basic process design, with an analysis of all unit operations was carried out.

For the scale – up and cost analysis 2 concepts, one based on a 2-stage gas permeation and pressure swing adsorption (PSA-CONCEPT) and a second based on a hypothetical electrochemical hydrogen compressor (EHC-CONCEPT) for hydrogen separation, with a daily hydrogen production comparable to a 1 MW electrolyzer have been designed for comparison. A pure PSA system and a cryogenic separation were ruled out in advance because of the low hydrogen concentration in the diluted gas stream.

As an electrochemical hydrogen separation via EHC of a diluted oxyhydrogen gas mixture hasn't been described in literature, a separation of a H_2 - O_2 - CO_2 gas mixture was carried out. 15.5% of H_2 were separated at a potential of 1 V and an energy consumption of 33.3 kWh/kg H_2 equivalent to 100.07% of the lower heating value of hydrogen. Heavy oxidation occurred on the current collector plates.

Based on a 7% solar to hydrogen efficiency and a lifetime of 6 months of the PhotoSomes, the system would require an area of around 80 000 m^2. The PSA-CONCEPT achieved a cost of 41.16 €/kg H_2 and the EHC-CONCEPT of 30.49 €/kgH_2 at a daily production of 483 kgH_2. The power requirement during operation reaches 5.429 MW for the PSA - CONCEPT and 3.532 MW EHC – CONCEPT producing hydrogen without net energy gain. The biggest obstacles for a cost-effective PhotoSome process are the energy consumption of the gas separation process, the cost of TEL lipids and the cost of stainless steel for construction of the photoreactor. The inherent intermittence of solar irradiation, subzero temperatures, and the actual behavior of PhotoSomes remain open questions.

A suspended single catalyst PhotoSome hydrogen production system is not cost-effective!

Further research should focus on the synthesis of higher-value products such as acetate and formate, avoiding a flammable gas atmosphere in the first place.

List of Abbreviations:

A

AEM ..... alkaline anion exchange membrane
AQY ..... apparent quantum yield
ATP ..... adenosine triphosphate
AWE ..... alkaline water electrolyzers
AWS ..... assisted water splitting

B

bR ..... bacteriorhodopsin
bRsyn ..... synthetic bacterorhodotpsin

C

CB ..... conduction band
CBM ..... conduction band minimum
CCUS ..... carbon capture, utilization and storage
CD ..... Carbon Dots
CIP ..... cleaning in place

D

Db ..... Desulfomicrobium baculatum
DCMU ..... 3-(3,4-dichlorophenyl)-1,1-dimethylurea
DDP ..... diketopyrrolopyrrole
DET ..... direct electron transfer
DF ..... Dark fermentation

F

FRET ..... Förster resonance energy transfer

H

H_2 ..... Hydrogen
H_2ase. ..... Hydrogenase
HHV ..... higher heating value
HTE ..... High temperature electrolysis

I

IO ..... inverse opal
IPCC ... Intergovernmental Panel on Climate Change
IQY ..... internal quantum yield
ITO ..... Indium Tin Oxide

L

LFL ..... lower flammability limit
LHC ..... light harvesting complex
LHV ..... Lower heating value
LOC ..... limiting oxygen concentration

M

MFC ..... Mass Flow Controller
MPA ..... 3- mercaptopropionic acid

N

N_2ase ..... Nitrogenase
NADPH ..... nicotinamide adenine dinucleotide phosphate

O

OWS ..... overall water splitting
oxyH_2 ..... oxyhydrogen

P

PBR ..... photobioreactor
PEM ..... proton exchange membrane
PMS ..... N-methylphenazonium methyl sulfate
PMsyn ..... synthetic purple membrane
POX ..... partial oxidation
PR ..... photo reactor
PS1 ..... photosystem 1
PS2 ..... photosystem 2
PSA ..... Pressure Swing Adsorption

Q

QE ..... quantum efficiency
QY ..... quantum yield

R

RHE ..... reversible H2 electrode
RuP ..... Ru tris(bipyridine)

S

SAPS ..... semi artificial photosynthetic system
SED ..... sacrificial electron donor
SMR ..... steam methane reforming
SOE ..... solid oxide electrolyzers
STH ..... Solar to H2 efficiency

T

TEL ..... archaeal tetrahedral lipid
TOF_{cat} ..... turnover frequency
TON_{cat} ..... turnover number
TRL ..... Technology Readiness Level

U

UFL ..... upper flammability limit
UP ..... unit operation

V

VB ..... valence band
VBM ..... valence band maximum

List of Symbols and Constants

A_i	surface [m²]
E^0	standard potential [V]
K_o	Cost factor o
M_i	molar mass component i [kg/mol]
P_u	Power, unit operation u [W]
Q_i	permeance component i *[mol/(m².s.Pa)]*
S_{i_j}	selectivity component i to component j
T_u	Temperature unit operation u [K]
$X_{m,i}$	adsorption loading, adsorbents m, component I [mol_i/kg_m]
$Yield_u$ or$Y_{i,u}$	yield component i, operation u [-]
$c_{p,i}$	specific heat capacity [J/mol*K]
d_i, L_i	Dimension [m]
$f_{in,u}$	inflation factor unit operation u [-]
j_{photo}	photocurrent [mA/cm²]
p_f	partial pressure feed side [Pa]
p_p	partial pressure permeate side [Pa]
t_u	process time unit operation u [s]
$x_{i,j}$	molar fraction, component i membrane element j
η_{STH}	solar to hydrogen efficiency [%]
η_u	efficiency unit operation u [%]
η_u	efficiency unit operation u [-]
σ_{PSA}	safety factor [-]
ΔH	reaction enthalpy [J]
$h\nu$	light energy
$r_{\$/€}$	exchange rate $/€
$\Delta G^0_{()}$	free Gibb energy [J]
AQY	apparent quantum yield
EQY	external quantum yield
$\phi\ (\lambda)$	quantum yield, also QY, [%]
$\dot{x}_{i,j}$	molar fraction component I, flow j
$\dot{n}_{i,j}$	molar flow component i
$\dot{m}_{i,j}$	mass flow component i, flow j
$\dot{W}_{out}$	electrical power output [W]
$\dot{W}_{in}$	electrical power input [W]
$\dot{V}_{i,J}$	volumetric flow component i, flow j
$\dot{Q}_{cool,HE}$	heat flow [W/m²]

List of Unit Operations

PHOTOSOME PRODUCTION

PBR	photo bio reactor
DS	disc separator
HS	resuspension and holding step
HPH	high pressure homogenization
F1	microfiltration
UC	ultracentrifuge
FOR	static T-mixer (formulation)
F2	ultrafiltration

PHOTOREACTOR

PR	photo reactor
RO	reverse osmoses water purification.

GASSEPARATION

MSS1	membrane separation stage 1
MSS2	membrane separation stage 2
EHC	electrochemical hydrogen compressor
O2S	oxygen separation
N2R	nitrogen recovery
MAS	membrane air separation
DE-OXO	de-oxo catalyst
PSA	pressure swing adsorption

GPi	gas compressor i
GVPi	gas vacuum pump i
HEi	heat exchanger i

Table of Content

1. Introduction

Global warming and the shift to renewables, energy independence, energy storage and soaring energy prices are the biggest challenges of our time. A rapid reduction of greenhouse gas emissions, global and local, is unavoidable. In a worldwide attempt to limit the fundamental changes to the ecosystem associated with climate change, the 195 signatory countries of the 2015 Paris Agreement on climate change agreed to ramp up their efforts to reduce their CO_2 emissions over the next century. To accomplish this task, the Intergovernmental Panel on Climate Change (IPCC) concluded that net global CO_2 emissions would have to reach a net zero by 2100 to limit global warming to 1.5°C[2]. In 2021 Global CO_2 emissions rose by 4.8% to 34.9 $GtCO_2$[3]. To achieve the 1.5°C limit set by the Paris Agreement, 8% reductions are needed per year to limit anthropogenic warming to 1.5 °C by 2100 with a 67% likelihood[3].

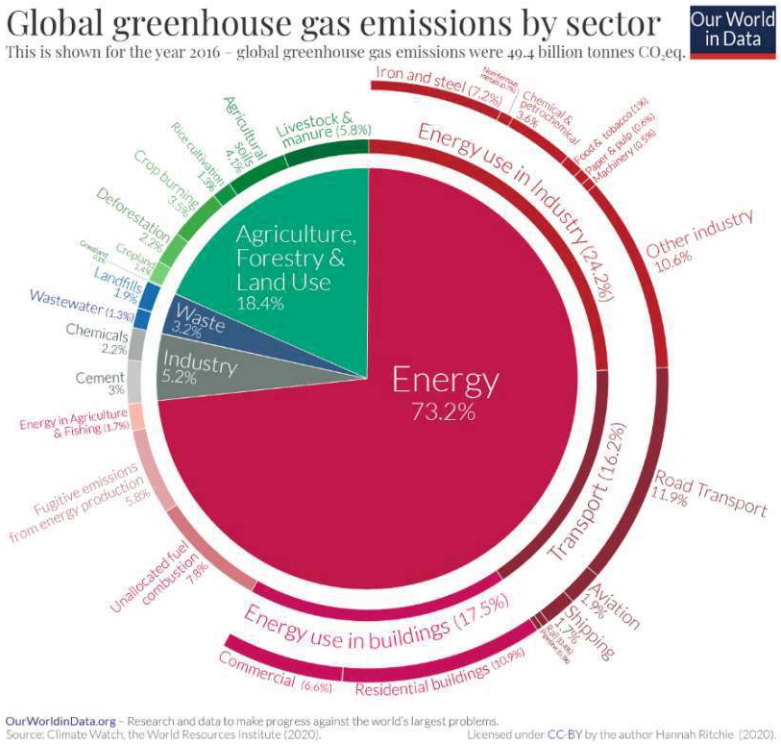

Fig. 1 Global greenhouse gas emissions by sector 2016 reproduced from OurWorldinData.org by Hannah Ritchie (2020) under CC-BY: Source:[4]

Most greenhouse gas emissions today are related to energy use, production and industry, making the transformation to renewable energy sources and the development of new green sources for feedstock chemicals inevitable. In order to achieve this shift away from fossil fuels and into renewable energy sources, a few obstacles must be overcome.

First, the intermittence problem. As the electric grid is a flow bases system, electricity must be produced at the moment of demand. However, sufficient electricity, especially wind – and solar power, might not be available at this instant. Therefore, power storage is paramount to provide stability and resilience to the grid.

Secondly hard-to-abate-emissions, notably in industries such as aviation, shipping, iron, cement and steel production, chemical manufacturing, with applications of high-temperature industrial heat, long-distance and long-haul road transport but also heat for buildings, particularly in dense urban environments or off -grid applications, have been notoriously difficult to decarbonize. These emissions occur in processes where electricity is currently not a viable energy form at the point of

end use and where direct electricity-based solutions come at high costs or with technical drawbacks. Besides the technological issues, missing infrastructure and supply chains are further hurdles. Green H_2, produced from renewable energy sources, solves these challenges. If produced at competitive prices and at a large scale, green H_2 would lay the foundation for the so-called "H_2 economy", an industrial system in which the dominant role of the energy carrier and fuel is performed by H_2 together with electricity. Also, H_2 is vital as green feedstock for the decarbonized chemical industry.

The benefits of H_2 have been routinely cited. Since H_2 combustion only emits water vapor, no greenhouse gases, particulates, sulfur oxides or ground-level ozone are produced using H_2. If H_2 is used in a fuel cell, even thermal NO_x emissions can be prevented. Replacing carbon-containing fuels with H_2 could lead to a reduction of local air pollution, improving environmental and health outcomes. Produced with renewable local resources, green H_2 will improve energy security and access. Especially during a time of soaring energy prices, the difficulties of dependence on a few oil and gas-producing nations for energy has become apparent as never before. Countries with high-quality resources for H_2 production are widely dispersed around the globe. Current energy exporting countries are finding themselves with renewable energy resources for a zero carbon - H_2 trade, to help bridge the gap during seasonal fluctuations. [5]

By converting electricity to H_2, stored H_2 can help alongside alternatives such as batteries and pumped-storage – hydropower to match energy supply and demand. As an energy carrier, piped H_2 or blended H_2 transported in existing natural gas pipelines, could supplement existing powerlines in energy transport. For the energy transformation to become a reality, vast quantities of green H_2 must be produced. However, existing technologies, photovoltaic cells, face a resource bottleneck at the required scale [6] necessary to accommodate expected demand and for example, copper and dysprosium are regarded as limiting resources in the scale-up of wind power in Germany[7]. Surprisingly water splitting also occurs in nature in a process called photosynthesis. Powered by sunlight, a combination of 2 biocatalysts, so-called enzymes, can produce H_2 from water. These enzymes can be manufactured with readily available resources, all around the world in a CO_2 negative process, reducing dependence on high-tech resource-rich countries such as China.

The goal of this master thesis is to evaluate the economic potential, technological limitation and showstoppers of a lipid-based semi-artificial photosynthetic system (SAPS) for green H_2 production.

2. Introduction into H_2

2.1. H_2 Properties

H_2 is the lightest chemical element with the atomic number 1 and symbol H. At standard conditions, H_2 exists as the diatomic gaseous H_2 molecule. Most H_2 on earth exists as water and is also found in a wide range of organic compounds. It is a non-toxic, odorless, tasteless, colorless gas. Due to its high flame velocity, broad ignition range and low ignition energy, it is highly flammable. This is partly mitigated by its high buoyancy and diffusivity, which causes it to dissipate quickly. Relative to carbon-based fuels, H_2 has a high combustion velocity. Because of its non-luminous flame, it is difficult to monitor and to detect fires and leaks[5]. H_2 has, compared to gasoline, an outstanding energy density per unit of mass however, a very low energy density per volume.

Properties	H_2	Comparison
Density (gaseous)	0.089 kg/m^3 (0°C, 1 bar)	1/10 of natural gas
Density (liquid)	70.79 kg/m^3 (-253°C, 1bar)	1/6 of natural gas
Boiling point	-252.76°C (1 bar)	90° below LNG
Energy per unit of Mass (LHV)	120.1 MJ/kg	3x that of gasoline
Energy density (ambient cond., LHV)	0.01 MJ/L	1/3 of natural gas
Specific energy (liquefied, LHV)	8.5 MJ/L	1/3 of LNG
Flame velocity	3.46 m/s	8x methane
Range of flammability in air	4 - 77 vol%	6x wider than methane
Range of explosivity in air	13 – 65 vol%	5x wider than methane
Diffusion coefficient in air	0.61*10^{-4} m^2/s	3x higher than methane
Autoignition temperature	585 °C	220 °C for gasoline
Ignition energy	0.02 MJ	1/10 of methane
Flame temperature	2045 °C	160 °C lower than gasoline

Tab. 1 physical properties of H_2 - Sources[5], [8]

2.2. Current H_2 production and consumption

Today, H_2 is almost entirely produced from unabated fossil fuels, either from natural gas or as a by-product of chemical processes. Only China produces significant amounts of H_2 from coal. Approximately 60% of H_2 is produced in "dedicated" production facilities as a primary product. By 2021 global H_2 production rose to 94 million tons (Mt)[1], releasing more than 900 Mt CO_2, slightly more than the annual CO_2 emissions of Indonesia and the United Kingdom combined [5], [9, p. 284]. 62% of H_2 is produced from natural gas without carbon capture, utilization and storage (CCUS). 19% are produced from coal, 18% as a by-product of naphtha reforming at refineries for other on-site refinery processes. Oil accounts for less than 1% of H_2 production. The largest part of low-emission H_2 is produced from fossil fuels with CCUS, accounting for 0,7% of overall H_2 production. Water electrolysis currently plays an insignificant role, however it's share increased by 20% compared to 2020 [9].

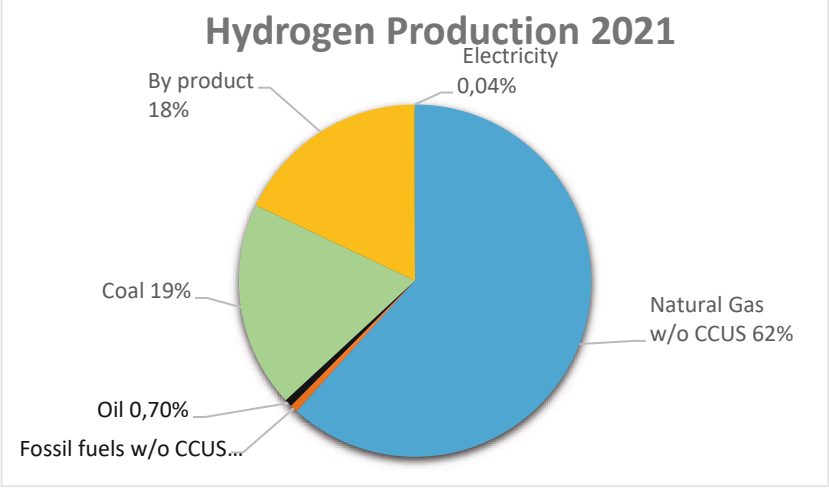

Fig. 2H2 production mix 2020/21, Data Source: [9, p. 71]

[1] This includes 74 Mt H_2 of pure hydrogen production and around 20 Mt H_2 mixed with carbon-containing gases in methanol production and steel manufacturing. It excludes around 30 Mt H_2 present in residual gases from industrial processes used for heat and electricity generation[5], [9, p. 284]:

Steam methane reforming (SMR), the main H_2 production method, is preferred due to its mature technology and heavy use in the industry[10]. Most H_2 is produced close to its end-use point, with resources extracted in the same country[5].

2.3. H_2 consumption

In 2020 global H_2 demand rose to about 90 Mt H_2, 40 Mt were consumed in refineries either as an energy source, cracking agent for hydration of liquid oils, to remove sulfur and N_2 compounds or as feedstock. The chemical industries' H_2 demand amounts to slightly more than 45 Mt H_2 as feedstock, with methanol production accounting for about one quarter and ammonia production for about three-quarters of consumption. Steel production with the direct reduced iron process consumes the remaining 5 Mt H_2 [11]. Less than 0.01 Mt per year of pure H_2 is used in fuel cell vehicles. Among other processes making use of H_2, the synthesis of aniline from nitrobenzene, the synthesis of hexamethylenediamine and the removal of trace amounts of oxygen in corrosion protection[12].

2.4. Categorization of H_2

To provide a clear labeling system, H_2 often is categorized, depending on the energy source of its production method, into black, gray, brown, blue, and green H_2. "Gray" stands for H_2 from fossil fuels, sometimes with further subdivision into "black", "gray" or "brown" for coal, natural gas and lignite-based H_2 production. "Blue" is used for fossil fuel-based H_2 production with CCUS to reduce CO_2 emissions. "Green" H_2 stands for production from renewable energy sources.

2.5. The Cost of H_2

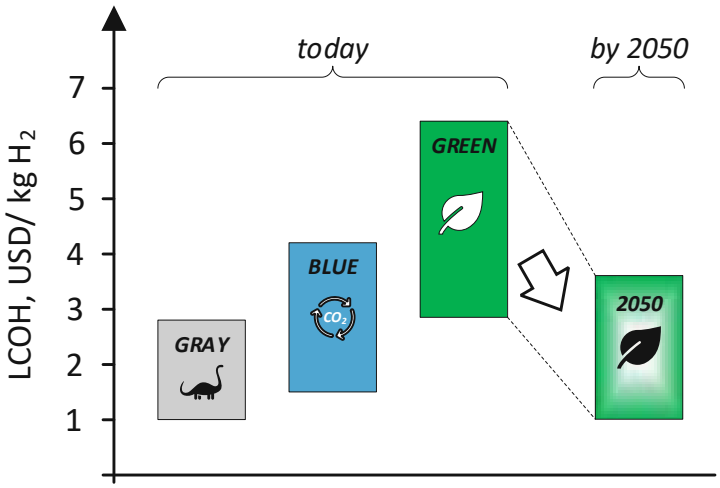

Fig. 3 The cost of H_2, Data Source:[13]

The cost of H_2 strongly depends on primary energy cost. Centralized production processes tend to be cheaper. Since H_2 will have to compete with natural gas and electricity powering and heating buildings, it is estimated that green H_2 will likely be in a price range of 1.5 - 3 USD/kg by 2050 [5]. The average global H_2 production cost for steam methane reforming (SMR) – H_2 amounts to 0.07 €/kWh, for coal gasification H_2 to 0.10 €/kWh. PV-based H_2 in Europe amounts to 2 €/kWh. In December 2019 the H_2 commercial price amounted to 0.42 €/kWh about 3 times more expensive than diesel [14]. The production cost for green H_2 is significantly higher compared to conventional methods. However it is only a matter of time for novel, highly efficient, green H_2 production methods to get cheaper with the introduction of advanced materials and innovative technologies [10].

2.6. Storage, Compression and Transport of H_2

Given that H_2 has a higher energy density per unit of mass compared to methane and gasoline, one might think H_2 is the perfect energy carrier but storage, compression and transport of H_2 face similar challenges such as low volumetric density, high boiloff and H_2 embrittlement. To move the same amount of energy with piped H_2 compared to natural gas, a larger gas volume must be transported. Resulting in, on one hand larger and/or fast flowing pipelines and larger storage tanks compared to the existing infrastructure. Therefore, significant effort went into increasing the volumetric energy density of H_2. H_2 can be liquefied, compressed, absorbed, converted to a H_2 carrier like methanol or ammonia, or absorbed by a liquid organic H_2 carrier fuel such a toluene, stored in metal hydrides, or stored in large underground salt caverns or depleted natural gas reservoirs.

H_2 STORAGE				
Storage form	***Energy Density***		***Density***	***Source***
	kJ kg^{-1}	MJ m^{-3}	kg m^{-3}	
H_2 gas (ambient 0.1 MPa)	120000	10	0.09	[8]
H_2 gas at 20 MPa	120000	1900	15.9	[8]
H_2 gas at 70 MPa	120000	5600	-	[15]
H_2, liquid	120000	8700	71.9	[8]
H_2 in metal hydrides	2000-9000	5000-15000	-	[8]
H_2 in metal hydrides, typical	2100	11450	5480	[8]
Methane (natural gas) at 0.1 MPa	56000	37.4	0.68	[8]
Methanol	21000	17000	0.79	[8]
Ammonia	22500	11500	0.73	[16]
POWERPASTE Fraunhofer IFAM	5760	68.4	-	[17]

Tab. 2 Comparison of H_2 storage forms

The most cost-effective way to store H_2 is in its gaseous form, for most application. Pressurized H_2 is usually stored between 150-300 bar with high pressure storage reaching up to 700 bar. These pressure vessels should be lightweight, easy to work with and inexpensive but also must withstand H_2 embrittlement. Carbon fiber reinforced plastics are an obvious choice, however due to their low thermal conductivity, they must be kept below a certain temperature during the exothermic filling of the tank to not exceed safety standards.

Metal hydrides can store and release H_2 based on a temperature-dependent absorption mechanism. Typically, they hold 1-2% of their weight in H_2. Challenges are the supply of heat or the need of a heat generation / transfer system, the time lag between initial heating and release of H_2 and limited reusability in case of impurities. This system offers a higher energy density compared to liquid and compressed H_2 at the cost of the high overall system weight. N_2 - and boron-based hydrides are quite promising alternatives due to their high H_2 content but still require further research into catalysts providing higher H_2 release rates. Gaseous H_2 storage in carbon nanotubes has also been studied, offering even higher storage capabilities compared to metal hydrates but this technology is still in early development. Capillary storage is based on physical gas absorption and is limited by the energy demand for H_2 release and long-term durability. Liquid H_2 storage is an energy-intensive process. As H_2 liquefies below -250 °C about one third of the H_2's energy content is necessary for the liquefication process. Cryogenic systems have high requirements on the material and airtight insulation to minimize boiloff. Further constraints are venting systems for the boil-off to keep the system at constant pressure. Specialized liquid H_2 handling equipment and processes such as airtight fitting and

lines are required since at these temperatures, air would freeze and block the flow. However, liquid H_2 energy offers a low overall system weight at high volumetric energy density. Cryo-compressed H_2 storage is an innovative approach that combines compression with liquefication, simply a two phases system with vapor in the headspace and liquid H_2. This system is more complex, bulkier, heavier and contains lower-density fuel but reduces overall fuel energy loss during liquefaction compared to liquid H_2 storage and is limited only to a few niche applications where liquid and gaseous H_2 is needed. [15]

Compression of H_2

H_2 compressors are classified into two groups, nonmechanical and mechanical. Mechanical compressors work on the principle of volumetric displacement and offer mature technology, easy accessibility, low-cost and easy maintenance. Examples of this are reciprocating piston compressors, diaphragm compressors and Ionic liquid compressors. Disadvantages are the high number of moving parts requiring lubrication and maintenance, as well as high power consumption. Nonmechanical systems are cryo-compressors, adsorption compressors metal hydride H_2 storage compressors and electrochemical H_2 compressors. [18]

Transportation of H_2

Transportation of H_2 will rely on compression, liquification or incorporation into larger molecules because of its lower volumetric energy density. Today most H_2 is distributed as compressed and liquified H_2 by truck. Pipelines – "*piped H_2*" – offer the lowest transmission cost. H_2 pipelines already exist, mainly within or between chemical industrial plants. Existing natural gas pipelines could be converted to pure H_2, requiring significant investment into new equipment as valves and compressors. Blended H_2 offers an intermediate solution based on existing natural gas infrastructure. Here H_2 is blended into natural gas. Regulation in Austria allows blends up to 10 vol% H_2. For shipped H_2, studies have shown that over 1500 km it is more cost-effective to ship H_2 liquified or as liquid organic H_2 carrier or ammonia than as compressed H_2. [5]

2.7. Standards for H_2 fuel and equipment

Currently, there are only a few standards for H_2. The quality requirements depend strongly on the application of H_2. The standards ISO/DIS 14687, DIN EN 17124, SAE J2719 and GB/T 3634.2-2011 describe quality requirements for H_2 as a fuel for stationary and mobile fuel cells by the minimum concentration of H_2 and max. concentration of other gases or trace elements. These are applied as a reference but not always. H_2 requirements might also be defined by the degree of purity. For instance, a degree of purity of 5.0 is the equivalent of 99.999% H_2 and 3.0 to 99.9% H_2 [19]. In Austria, the standard ÖVGW G B210 sets the requirements for piped natural gas. Currently up to 10% H_2 can be added to the natural gas as a carbon free replacement gas. At this point the ASME B 31.12 – H_2 piping and pipelines should also be mentioned. The analysis of H_2 fuel for PEM purposes is standardized by DIN ISO 21087.

Standard:	***H_2 PEM applications, DIN EN 17124, ISO 14687 (Type I/II D)***	***ISO 14687 Typ I, E, Kat3***
application:	mobile PEM	stationary PEM
H_2	99.97 %	> 99.9 %
Non H_2-Gases	300 µmol/mol	<0.1%
Water	5 µmol/mol	no condensation at ambient conditions
non methane hydrocarbons	2 µmol/mol	< 2 µmol/mol
methane	100 µmol/mol	< 100 µmol/mol
oxygen	5 µmol/mol	< 50 µmol/mol
helium	300 µmol/mol	< 0.1 %
N_2	300 µmol/mol	
argon	300 µmol/mol	
CO_2	2 µmol/mol	2 µmol/mol
CO	0.2 µmol/mol	0.2 µmol/mol
overall sulfur	0.004 µmol/mol	0.004 µmol/mol
HCHO	0.2 µmol/mol	0.2 µmol/mol
HCOOH	0.2 µmol/mol	0.2 µmol/mol
ammonia	0.1 µmol/mol	0.1 µmol/mol
halides	0.05 µmol/mol	0.05 µmol/mol
fog, dust, fluids	1 mg/kg	-
airborne particles	-	< 1 mg/kg
size of particles	-	< 75 µm

Tab. 3 most applied H_2 standards, Source:[20]

Based on these main criteria for this study are 99.97% H_2 purity, max CO_2 concentration of 2 µmol/mol and max. water content of 5 µmol/mol.

3. H_2 production methods

H_2 production methods are classified either by the natural resources used to extract H_2 for instance hydrocarbons and water or by the primary energy source as fossil fuels or by its primary energy source such as fossil, electrical, biochemical, biological and solar.

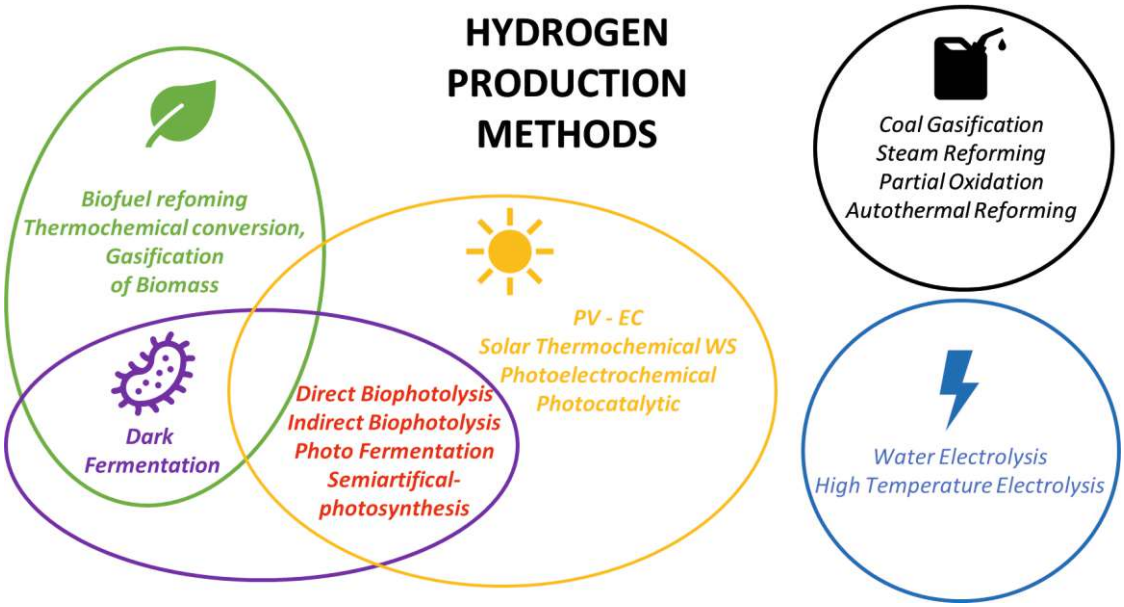

Fig. 4 H_2 production methods

3.1. Gray H_2 production methods

This chapter offers an overview of current fossil-based H_2 production methods. These methods operate at high temperatures, often exceeding 700°C, are energy intensive, require purification steps and are associated with N_2, sulfur, heavy metals contaminated ash and high CO_2 emissions [12].

Gray H_2 production methods are coal gasification, reforming with steam methane reforming, steam reforming, partial oxidation, autothermal reforming, thermal cracking – water thermolysis and thermochemical water splitting.

Coal gasification is a two-step process. In a first step, coal is partially oxidized at high temperatures and pressures by using steam and O_2-producing syngas, a gas mixture consisting predominantly of H_2, CO, steam and CO_2. Secondly, the H_2 concentration is further increased by converting the CO with additional steam and a catalyst to CO_2 and H_2 by water gas shift reaction. Followed by a gas purification step, generally through a pressure swing adsorption (PSA), to eliminate the remaining sulfuric acid, elemental sulfur and other impurities in order to produce pure H_2. There are several different process variants. Due to the feedstock, coal gasification leads to high CO_2 emissions. Currently the cost of H_2 via gasification is slightly higher than that of steam reforming. Even though fuel cost is lower compared to SMR, capital cost is significant. Coal gasification for H_2 production is mainly practiced in China. [10]

Steam reforming is an endothermic process producing a syngas mixture of CO and H_2 by a reaction of hydrocarbons with steam in the presence of a nickel-based catalyst at temperatures of 750-1000°C. In a second step the H_2 content is increased in an exothermic water gas shift reaction, converting the CO with H_2O to CO_2 and H_2. To ensure a complete reaction of the CO, the water gas shift reaction is split into a high temperature, between 500 – 300°C and a low temperature at 200°C step with different catalysts. To remove the CO_2 at the end, several different methods, including adsorption, absorption and membrane separation, are in use. Feedstocks for steam reforming could be methane, ethanol, and Fischer-Tropsch distillates.

As ***steam methane reforming*** (SMR) it is regarded as the most deployed H_2 production method accounting for 48% of worldwide H_2 production. The endothermic SMR process operates at

temperatures between 700 – 1000°C and in a pressure range between 3 and 25 bar with a Co-Ni catalyst. H_2 is produced under the following reactions:

$$CH_4(g) + H_2O + heat \longrightarrow CO + 3H_2 \quad \Delta H_R: -\frac{206kJ}{mol} \ (Eq\ 3.0)$$

$$CO + H_2O \longrightarrow CO_2 + H_2 + heat \ (Eq\ 3.1)$$

The CO concentration is reduced via a high-temperature shift converter below 1000ppm and further reduced to less than 10 ppm in a PSA. H_2 with a purity of 99.9995% is produced. Compared to partial oxidation and autothermal reforming, SMR is a highly efficient process with lower emissions and lower cost of large production units. However, it is a complex system and sensitive to changes in natural gas qualities. [10]

In ***partial oxidation*** (POX), the fuel is partially combusted with O_2 to produce carbon monoxide and H_2. Since this is an exothermic reaction, an external heat source is not required. The product gas can further be converted by a water gas shift reaction to higher H_2 content. This process does not require a catalyst and is more tolerant to sulfur compared to steam and ATR.

The ***autothermal reforming*** (ATR) process is a combination of POX and steam reforming. In a thermo reactor, hydrocarbons react with O_2 and steam in a catalyzed reaction to produce syngas, a mixture of CO and H_2. This process operates without an external heat source and is powered by heat exchange between the exothermic partial oxidation and the endothermic steam reforming reaction. These 2 reactions can be carried out in a single combined reactor or 2 separate gas-heated reactors. The ATR process operates at 1900°C in the combustions zone and at about 900 - 1100°C in the conversion zone. The produced syngas then can further be converted in a water gas shift reaction to increasing the H_2 content. Compared to POX, ATR operates at lower pressures. Since ATR and POX need additional oxygen separation processes, they are more complex and are therefore more expensive than steam reforming. ATR and POX systems are compared to SMR, smaller, simpler and cheaper at a smaller scale, however they operate at lower efficiency and H_2 purification and higher emissions are remaining challenges. [10]

Thermal cracking of hydrocarbons produces H_2 by breaking down hydrocarbons under high temperatures, in an oxygen free atmosphere to obtain in a catalyzed reaction carbon and H_2. The thermal cracking of methane is described as follows:

$$CH_4 \longrightarrow C + 2H_2 \left(\Delta H = \frac{75.6kJ}{mol}\right), (Eq\ 3.2)$$

The biggest advantage of thermal cracking is H_2 production without CO_2 emission. The H_2 is easily separated from the by-product carbon. To power this endothermic reaction about 10% of methane feed is needed as input energy. [21]

The second process based on thermal dissociation is the one-step thermal water splitting process called ***water thermolysis***. To achieve a high degree of dissociation, high temperatures and pressures are needed. In case of 3000K and 1 bar approximately, the reaction has a degree of dissociation of 65%. For the required separation of the H_2, oxygen, water vapor mixture the product gas must be cooled down since there are no stable membranes available above 2500K. To eliminate oxygen - H_2 recombination the product gas has to be cooled down quickly to about 1500 - 2000K. Palladium membranes for H_2 separation can also prevent recombination. [10]

Thermochemical water splitting is a process applying high-temperature heat to drive a series of chemical reaction to produce H_2. Since all chemicals are reused in the process within each cycle, the

process only requires water to produce O_2 and H_2. The key advantages are that the process does not require any catalysts to speed up or initiate the reaction, moderate operating temperatures between 600 and 1200K, low power input requirement and product gas separation without the need for special membranes. There are several thermochemical water splitting cycles described in literature. However, the S-I cycle is regarded as the most technically feasible one. It consists of the following reactions.

$$H_2SO_{4(aq)} \xrightarrow{heat\ (300-500°C)} H_2O_{(g)} + SO_{3(g)}, (Eq\ 3.3)$$

$$SO_{3(g)} \xrightarrow{heat\ (800-900°C)} \frac{1}{2}O_{2(g)} + SO_{2(g)}, (Eq\ 3.4)$$

$$SO_{2(g)} + I_{2(g)} + 2H_2O_{(l)} \rightarrow 2HI_{(g)} + H_2SO_{4(aq)} + \Delta H, (Eq\ 3.5)$$

$$2HI_{(g)} \xrightarrow{heat\ (425-450°C)} H_{2(g)} + I_{2(g)}, (Eq\ 3.6)$$

The S-I has no side reactions or undesired byproducts. But the heat requirements for the endothermic reactions of the water splitting cycle are quite high. Heat from biomass, solar, nuclear or heat recovered from industrial processes could drive this process in a sustainably. [10] This green H_2 method is described in more detail in chapter 3.5.2.

3.2. Green H_2 production methods

The interest in research and implementation of green H_2 production has been growing lately. Green H_2 production methods are roughly grouped into electrical, biomass - based and solar methods supplemented by several hybrid methods.

Comparison Green H2 Production Methods						
Power Source	***H2 Production Method***	***Principle***	***Performance***	***Limiting Factors***	***Cost***	***Source***
Electric	PEM Electrolysis	Decomposition of water to H_2 and O_2 due to the electric current passing through the electrolyzer	***TRL 10 Commercialized*** 64-82% HHV 4.5-7.5 kWh/Nm^3	use of noble materials, high membrane cost, low durability, acidic environment	Strongly depended on price/ source of electricity: green H2 prices: 1.08-16.01 $	[22]
Electric	Alkaline Electrolysis		***TRL 10 Commercialized*** 67-84% HHV 4.5-7 kWh/Nm^3	corrosive electrolyte, low H_2 purity, slow startup, low current density,		[22]
Electric	AEM Electrolysis		***TRL 10 Commercialized*** ~4.8 kWh/Nm^3	Low ionic conductivity, low membrane stability, low lifetime		[22]
Electric	SOE-Electrolysis		***TRL 8 Precommercialized*** ~90%HHV 2.5-3.5kWh/Nm^3	unstable electrodes, safety and sealing problems, bulky design, use of brittle materials		[22]
Electric Biomethane (plastic waste)	Plasma Arc pyrolysis	A process that splits natural gas (mostly methane) into H_2 and carbon black (soot) due to the activity a plasma.	***TRL 9 Precommercialized***	not cost competitive to SMR yet, low TRL for non - recycle plastic waste plasma pyrolysis	2-3 €	[23]
Electric	Sono-chemical	Forming of radicals after implosion of cavitation bubble	***TRL 2*** $5.46*10^{-6}$ - $8.59*10^{-6}$ µmol/h for H_2O/O_2 bubble or 20-30 µmol/kWh for H_2O/Ar bubble	*Low TRL*	no data	[24]
Biological waste	Biomass Steam Gasification, Supercritical water gasification, Fast pyrolysis	endothermic dissociation of biomass at high temperature to produce syngas - often coupled with water gas shift reaction	***TRL 8 precommercialized*** [wt%, g H_2 / 100 g biomass] 7-4g Steam gasification, 5-3g Supercritical water gasification 3-2g Fast Pyrolysis palm empty fruit bunch gasification: up to 127g H_2/kg biomass with 75 vol% H_2	more research in cost-effective catalyst, catalytic selectivity and stability needed, Costly biomass supply, Corrosion, Tar production, Gas purification	12.75-9.5 €/kg.	[25], [26]
Biological waste	Dark fermentation	Biological decomposition of biological waste, H_2 as main product and value-added byproduct (often volatile fatty acids)	***TRL 5*** theoretical: 4 mol H_2/ mol glucose with optimized cell cultures: 5.6 mol H_2/mol glucose	strain optimization, substrate pretreatment, local availability of sufficient amounts of substrate, Gas treatment	18.7 $ hybrid system: 2.8-2.5 $	[27]

Biological waste + Solar	Photo fermentation	During photo fermentation, the production of bio H_2 occurs in the absence of oxygen but in the presence of light by the help of photoheterotrophic bacteria. Release of H_2 and CO_2	***TRL 5*** theoretical: 8 mol H_2/mol glucose practical: 1.1 - 2,8 mol H_2/mol glucose	low H_2 rates, H_2 separation, pretreatment of substrate,	3.7 $/kg hybrid system: 2.8-2.5$	[27], [28]
Solar	PV-EC	PV Cell connected to electrolyzer unit	***TRL 8*** **Precommercialized** up to 30% STH	Optimized PV to Fuel cell area ratio	0.90€ (Pt/IrO_4) 1.44 € (Co_3O_4)	[29]
Solar	Photo electro chemical PEC	Electrochemical (half-)cell with at least one photoelectrode with suitable bandgaps to allow for water splitting. Production of H_2/O_2 in separate compartments possible	***TRL 5*** dual unbias photoelectrodes STH <1% PV integrated PEC STH>20%	low yields, corrosion	8.43 $ @ STH 10%; 2.9-18.8$	[30], [31]
Solar	Photocatalytic PC	Semiconductor based (suspended)photocatalyst with cocatalysts capable of water splitting	***TRL 5***	gas separation, low yields	$1.50 – 2.30	[31]
Solar	SAPSs PC	Similar to PC - photocatalyst with constructed partly with biological components	***TRL 3*** STH 1.8% white light; up to STH 9% monochromatic light	gas separation, photostability, bio-/artificial Interface, charge transfer	no data	[32]
Solar	SAPSs PEC	Similar to PEC – Photocatalyst: semi-biological construct	***TRL 3*** 5.4±0.3 % STH	photostability, bio-/artificial interface, charge transfer	no data	[33]
Solar	Bio photolysis	Water is directly converted to H_2 by solar light via N_2ase and H_2ase	***TRL 5*** direct bio photolysis 2% STH indirect bio-photolysis 0.5-2% STH	oxygen inhibition, despite high theoretical yields - low real yields	3.10 $	[34]
Solar / high temperature heat	Solar- thermo chemical	thermochemical processes using chemical redox reactions, 2-, 3-, 4 step thermochemical water splitting cycles can generate H_2 more efficiently due to reducing temperatures.	***TRL 8*** up to 25% STH thermal efficiencies over 50%	chemical stability of equipment	8.4$ - 2.6$	[35], [36]

Tab. 4 Comparison of Green H_2 Production Methods

3.3. Electrical H_2 Productions Methods

The carbon footprint and classification of electrical H_2 production methods depends on electrical power source. When powered by renewable electricity, they are considered as green. Electrical H_2 production methods are water electrolysis, high temperature heat electrolysis, plasma composition and sono-chemical H_2 production.

Water electrolysis is the most important industrial water splitting process for pure H_2 generation. Water is split into H_2 and oxygen through the application of electrical current. An electrolyzer unit comprises of an anode and cathode immersed in an electrolyte. When electrical current is applied, H_2 is produced at the cathode – and oxygen on the anode side as:

$$2H_2O \longrightarrow 2H_2 + O_2, (Eq\ 3.7)$$

Increased temperatures decrease the electrical energy demand. [10] There are 4 different types of electrolyzers in operation, proton exchange membrane (PEM) electrolyzers, alkaline water electrolyzers (AWE), alkaline anion exchange membranes (AEM) and solid oxide electrolyzers (SOE). These systems are either commercialized or at pre-commercial stage with efficiencies between 64%-90% of higher heating value (HHV). PEM and SOE systems reach stack lifetimes below 40000 hr achieving H_2 purities up to 99.999%. An in-depth review of the current status of electrolyzers has been written by Nasser et al. [22] High temperature, or solid oxide electrolysis (HTE) splits steam into O_2 and H_2 at temperatures between 700 and 1000 °C. HTE requires less electrical energy compared to room temperature electrolysis because of higher efficiencies at increased temperatures. HTE requires a significant heat input to evaporate the water and heat the steam to operating temperatures. Can be provided either by external heat sources or direct steam injection. With high-temperature heat sources such as solar geothermal and solar, HTE can produces H_2 with CO_2 emissions close to 0. To overcome these challenging operating conditions, system components must provide physical and chemical stability at high ionic concentrations, high operating temperatures as well as low electrical conductivities even in contact with extremely reducing and oxidizing mediums. Especially electrodes need to be porous with enhanced electrical and thermal conductivities and be chemically stable in extremely reducing and oxidizing environments. [10]

Plasma arc decomposition, also known as high-temperature pyrolysis, is a process that splits natural gas (mostly methane) or biomethane into H_2 and carbon black (soot), due to plasma. Compared to thermal cracking, plasms arc decomposition is capable of breaking down heavy oil fractions and organic matter. The plasma gas is supplied by electrodes and methane is introduced from the top inlet of the reactor. The carbon stays back at the bottom of the reactor while pure H_2 is generated. It is estimated that the cost of plasma arc decomposition is no less than 5% lower compared to large-scale SMR combined with carbon capture. If this process is powered by renewable energy, no CO_2 is emitted. [21] Plasma pyrolysis is already deployed at precommercial scale TRL 8-9 with expected cost 2-3 €/kg H_2 [23]. If supplied by biomethane and renewable electricity.

3.4. Biomass based H_2 production.

Biomass-based H_2 production methods are either thermochemical, biochemical or biochemical–solar methods.

Biomass-based resources for H_2 production are grouped into 4 groups:

i. Forest wastes (tree and bush cutting, residues from wood cutting and processing)
ii. Purposely grown energy plants
iii. Agricultural waste: animal and plant waste
iv. Urban and Industrial waste (sewage sludge, industrial wastes...)

The mass fraction of H element in biomass is ~6%, which is equivalent to 0.672 m^3 gaseous H2 produced by 1 kg biomass, accounting for more than 40% of the total energy of biomass. [26]

3.4.1. Thermochemical conversion of biomass

The production of green H_2 via thermal valorization of biomass via syngas reforming with steam gasification, supercritical water gasification and or bio-oil reforming with fast pyrolysis coupled with water gas shift reaction.

In general terms, the biomass conversion is described by:

$$\alpha C_l H_m O_n + \beta H_2O \xrightarrow{heat} aH_2 + bCO + dCH_4 + eC + fTar, (Eq\ 3.8)$$

As an unwanted byproduct, tar impacts the reaction negatively. With solid biomass, the following biomass gasification takes place.:

$$C_x H_y + xH_2O \xrightarrow{high\ temperature\ heat} \left(\frac{y}{2} + x\right) H_2 + xCO, (Eq\ 3.9)$$

Current research into biomass gasification strongly focuses on the development of new, cost-effective catalysts increasing H_2 selectivity and content in the product gas. Alkaline earth metallic catalysts, metal and metallic oxides catalysts, natural mineral catalysts and hybrid catalysts are investigated [26]. The average H_2 production in (wt%, g H_2 / 100 g biomass) ranges between 7-4 g for steam gasification, 5-3 g for supercritical water gasification and 3-2 g for fast pyrolysis. Therefore gasification is regarded more promising in industrial production because of its high H_2 yield and efficiency [26]. Recent experiments with palm empty fruit bunch achieved up to 127 g H_2/kg biomass with 75 vol% H_2 [25]. More research is still needed into the development of cost-effective catalysts to increase H_2 production, reduce the gasification temperature and promote tar cracking. Even though the selectivity of catalysts has already improved, stability and recyclability remain an issue for scale-up [26]. The main challenges on the way to commercialization of biomass gasification include unreliability of the gasification equipment, the inability to produce the gasification products according to the specification of the clients and the lack of secondary pollution handling of gasification. Also the exorbitant high biomass transportation cost and gas purification for fuel cell grade H_2 remain an issue [37]. Fixed, moveable, and fluidized bed reactors are used for biomass gasification. Depending on the heat input requirement, the process can be thermal or autothermal [10].

3.4.2. Dark fermentation

Dark fermentation (DF) is a biological H_2 production method by heterotrophic microorganisms in the absence of O_2 and light. A wide array of low-value organic waste streams can act as possible feedstocks. Hereby organic substrates, carbohydrates, are turned into organic compounds with simultaneous production of molecular H_2. Compared to photo-fermentation, dark fermentation is more promising because of higher H_2 production rates and treatment capacity for organic wastes. With glucose as a model substrate in dark fermentation, several biochemical pathways can lead to H_2 production, determining theoretical H_2 yields and byproducts, acetate and butyrate being the most common ones, setting the theoretical stoichiometric limit for H_2 production. [38] In dark fermentation CO_2 is emitted.

$$Acetic\ acid\ pathway: C_6H_{12}O_6 + 2H_2O \rightarrow 2CH_3COOH + 2CO_2 + 4H_2, \ (Eq\ 3.10)$$

$$Butyric\ acid\ pathway: C_6H_{12}O_6 \rightarrow CH_3CH_2CH_2COOH + 2CO_2 + 2H_2, \ (Eq\ 3.11)$$

With butyric acid as a final product, a theoretical stoichiometric H_2 yield of 2 mol per mole of glucose (i.e., 272ml H_2/g hexose at 25°C), with acetic acid 4 mole of H_2 per mol of glucose (i.e., 544ml H_2/g hexose at 25°C) also known as Thauer limit can be reached. The most efficient known bio-H_2 producer is *Clostridium sp.* with H_2 yields of 1.5 – 3 mol H_2/mol hexose [39]. Overcoming the Thauer limit was achieved with an artificially designed microbial consortium of *E. aerogenes* and *C. acetobutylicum* in a ratio of 1:10000, yielding 5.6 mol H_2/mol glucose [40].

To improve the efficiency of dark fermentation , biorefineries concepts incorporate DF as a first-stage process to produce a precursor for a value-added product. DF can also be coupled into a 2 stage hybrid process with photofermentation to increase H_2 yield and overcome fatty acid inhibition. In order to increase sustainability, DF has been coupled with biomethane production, improving the energy recovery from the DF residues. The advantages of DF are continuous, light-independent H_2 production, low required energy input and simplicity in scale-up. The biggest challenge in DF towards scale-up and process optimization are the biocatalyst nature and its metabolism, syntropy and interactions among microbes, nature of the feedstock, feedstock pretreatment, H_2 inhibition, substrate nature and composition, redox and temperature conditions, reactor configuration and gas treatment. Therefore new strategies in pretreatment, genetic engineering and optimizations of microbial cultures, integrated DF processes and substrate optimizations are being explored. [38]

A 1000 L DF pilot scale system has been already developed, producing 76.3 m^3 of H_2 with a COD removal and energy conversion efficiency of 18.1 kg/m^3 and 37.9% [41]. To the best of our knowledge, no studies have reported the DF process at industrial- or full scale. Detailed reviews on DF have been published by Ghimire et al. [42]. The process design for dark fermentation depends mostly on substrates, limiting the operational conditions of bioreactors such as culture temperature (mesophilic or thermophilic), reactor configuration (reactor types, wet, semi-dry or dry conditions) and feeding mode (mono substrate or co-substrates). Besides a range of solar biological H_2 production methods, dark fermentation can be seen as the only purely biological H_2 production method, as it is solely powered by biomass. Dark fermentation is still in pilot-scale phase at TRL 5.

3.5. Solar H_2 production methods

Fossil production methods need to be replaced because of their carbon footprint however, electricity from renewable sources is in short supply and biological resources are limited and often used for other processes, the production solar green H_2 is of great interest and offers great potential. Solar H_2 production methods can be summarized in photocatalytic, photo electrochemical, photovoltaic – electrochemical, solar thermochemical and photobiological.

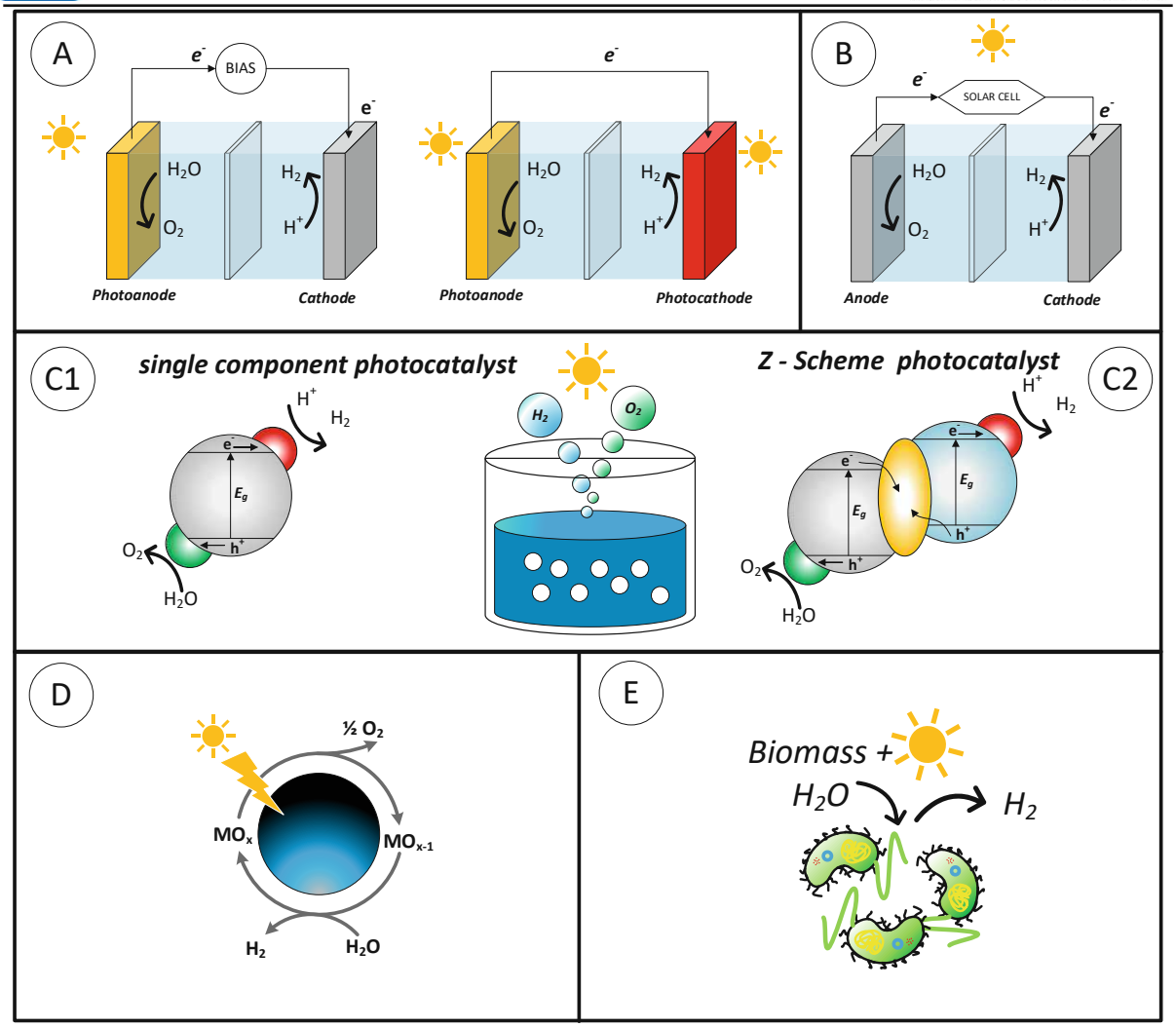

Fig. 5 Solar H_2 Production Methods: ; A, Photo electro chemical (PEC); B, Photovoltaic - electrochemical (PV - EC); C, Photocatalytic (PC); D, solar thermochemical (STC); E, Photothermal catalytic from hydrocarbons (STC); F, Photobiological graphic modified but based on picture from Solar-Driven H_2 Production: Recent Advances, Challenges, and Future Perspectives by Hui Song, Shunqin Luo, Hengming Huang, Bowen Deng, and Jinhua Ye, ACS Energy Letters 2022 7 (3), 1043-106 , DOI: 10.1021/acsenergylett.1c02591 with permission under CC-BY 3.0 Source: [43, p. 1045]

	Method	Efficiency
A	photoelectrochemical (PEC)	~19.3%
B	photovoltaic– electrochemical (PV-EC)	~32%
C	photocatalytic (PC)	5%
D	solar thermo chemical (STC)	<25%
E	photobiological (PB) H_2	1–3%

Tab. 5 Overview solar H2 production methods and efficiencies

3.5.1. Photo Biological H_2 production

Biological H_2 production is defined as H_2 production with bacteria and microalgae from water, biomass or organic wastes by photobiological or biological pathways. In nature, H_2 is a byproduct at the anaerobic conversion of organic matter to volatile acids, which are metabolized by methane bacteria and do not accumulate in the environment. Essential for the production of bio H_2 are H_2-producing enzymes such as N_2ase and H_2ase.

3.5.1.1. Biophotolysis and Photo fermentation

Biophotolysis and photo fermentation are processes of H_2 production from water by sunlight energy using biological systems. Biophotolysis processes can be classified into 3 categories, direct, indirect and photo fermentation. These processes are catalyzed by H_2ase and N_2ase. N_2ase is responsible for the main amount of H_2. Under anaerobic conditions N_2ase uses electrons and ATP (adenosine triphosphate) to produce H_2 and ADP (Adenosine diphosphate).:[27]

$$2H^+2e^- + 4ATP \rightarrow H_2 + 4ADP + P_i, \qquad (Eq\ 3.12)$$

3.5.1.2. Direct biophotolysis

Direct biophotolysis is a biological process producing H_2 by water splitting powered by sunlight with microorganisms capable of photosynthesis such as cyanobacteria or eukaryotic microalgae under anaerobic conditions catalyzed by H_2ase as follows:

$$2H_2O + Solar\ Energy \longrightarrow 2H_2 + O_2, \qquad (Eq\ 3.13)$$

This process is limited by the oxygen sensitivity of the H_2ase known as oxygen inhibition. Bio photolysis biggest advantage is H_2 production at moderate temperature and pressures. Direct bio-photolysis is reaching solar to H_2 efficiencies of 2%. [34] It hasn't been commercialized yet.

3.5.1.3. Indirect biophotolysis

Indirect biophotolysis solves the O_2 sensitivity limitation by separation of the O_2 and H_2 producing reactions. The CO_2 acts in this 2-step reaction as an electron carrier. The algae first fixate the CO_2 as a carbohydrate, then produces H_2 in a dark fermentation process as follows:

Step 1 CO_2 fixation: $12H_2O + 6CO_2 \longrightarrow C_6H_{12}O_6 + 6O_2, (Eq\ 3.14)$

Step 2 fermentation: $C_6H_{12}O_6 + 12H_2O \longrightarrow 12H_2 + 6CO_2, (Eq\ 3.15)$

The advantage of indirect bio photolysis to direct photolysis is the separation of O_2 and H_2 generation avoiding O_2 inhibition of H_2 evolution. It reaches STH efficiencies of 0.5-2.5%. [34]

3.5.1.4. Photo fermentation

Photo fermentation is an anoxic or anaerobic process utilizing sunlight as the energy input for converting organic substrates into H_2 and CO_2 by photosynthetic bacteria or purple non-sulfur bacteria. Photo fermentation is compelling for removing environmental pollutants and industrial organic wastes, along with the generation of renewable H_2. The theoretical H_2 yield is 8 mol of H_2/mol of glucose, practical yields of 1.1 – 2.8 mol H_2/mol of substrate have been reached. Challenges for photo fermentation are, oxygen removal to avoid inhibition, low efficiency of light conversion (1-5%), dependency on sunlight cycle. [28]

To overcome yield limitation, photo fermentation can be coupled as a second stage with dark fermentation, utilizing volatile fatty acids produced by dark fermentation. Pilot systems have been tested with pH control to control gradual acidification by production of organic acids with molasse by using the purple non-sulfur bacterium *Rhodobacter capsulatus.* Producing for 48h high purity H_2 with a yield of 0.69 mol H_2/(m^3*h) [44]. The implementation of the process is difficult because of the

required surface for light collection. The construction of high surface-to-volume ratio photo bioreactors for direct solar radiation absorption is challenging.

3.5.2. Solar thermal H_2 production methods - (Hybrid-) Thermochemical Cycles

As thermolysis of water requires extremely high temperatures, thermochemical H_2 production processes have been developed. By using chemical redox reactions utilizing metal oxides in 2 to 4 step thermochemical processes, more efficient H_2 production at lower temperatures is possible. In general, the higher the number of cycles/steps, the lower the required max. temperature of the system. To further decrease the required temperature, cost and effort for byproduct treatment and corrosion by toxic chemicals as well as increase efficiency, hybrid cycles with an electrochemical have been developed. Hereby water molecules are split via a repetitive pathway consisting of a series of intermediate reactions with the aid of several reactive species. The system operates in a closed loop consuming only water. Advantages are that the required temperature is between 1800°C and 500°C, and the system operates without electricity and no oxygen-H_2 membranes for separation are needed. [35]

Compared to thermochemical water splitting cycles, hybrid thermochemical cycles operate at lower temperatures, allowing the usage of lower-quality heat sources such as recovered heat. Hybrid thermochemical cycles are powered by external electrical and thermal power sources. Among the studied hybrid thermochemical cycles, the 5 step Cu-Cl cycle distinguishes itself by low operating temperature of 550°C, it consists of 3 endothermic, one electrochemical and one drying process. Municipal waste incineration, concentrated solar processes, industrial processes could supply the required low temperature heat sustainably. [10] STH efficiencies for solar/thermal systems have been reported to 25.8% [36]. A 100kW pilot plant system has been realized at the Plataforma Solar de Almerı´ [45].

3.6. Photocatalysis and Photochemical Method

Photocatalysis is a process that converts photonic energy directly into chemical energy, in this case, H_2, without the intermediate step of “grid-like” electrical energy. Photocatalytic systems are separated into Photovoltaic electrolysis (PV-EC), Photoelectrochemical PEC and Photocatalytic PC Methods.

3.6.1. Photovoltaic Electrolysis PV - EC

Photovoltaic-supported electrolysis is the most mature technology for solar H_2. Commercialized PV cells are connected by 2 wires to an external commercial PEM electrolyzer, producing H_2 and O_2 in separate compartments by water splitting. This so-called “external” PV-EC system has been commercialized already. However, there are also several integrated designs directly incorporating and (electrically via interfacial connections) connecting the electrolyzer to the PV cell. These integrated designs have been developed to pilot scale.[46] The PV cell has to provide a photovoltage above 1.6 V to overcome overpotential losses. Compared to the simpler design and lower cost of PC systems, PV-EC offers higher STH efficiencies than PC additionally, the H_2 and O_2 can be produced in separate compartment using proton/anion exchange membranes lowering the explosion hazard, avoiding gas separation and lowering losses by backreactions with the trade-off of higher overpotentials. Some PV-EC concepts allow positioning of the photo absorber outside of the electrolyzer, improving chemical stability against corrosion in the electrolyte. A InGaP/GaAs/ GaInNAsSb triple-junction solar cell connected with a PEM electrolyzer, achieved a record average ~30% STH efficiency over a 48-h test [47]. Challenges for scale-up of PV-EC systems are economic feasibility, optimized PV-to-electrolyzer area ratio, fabrication process, chemical stability of coatings and fuel separation [29], [46]. Studies have shown that PV-EC should be able to achieve ~0.90 \$/kgH_2 with noble metal catalysts (Pt/IrO_2) and \$ 1.44/kg H_2 (Ni/Co_3O_4) for earth-abundant catalysts [29]. An in-depth review

about *"Scalable Photovoltaic-Electrochemical Cells for H_2 Production from Water - Recent Advances"* has been written by Lee et al. [46].

3.6.2. Performance Metrics

Since evolution rate of O_2 and H_2, often defined in mol·h^{-1} and mol·h^{-1}·g^{-1}, strongly depends on measurement pressure, intensity of light source, structure of instrument, other metrics are used to accurately compare photocatalysts and processes.

Solar to H_2 efficiency (STH) η_{STH} [%] is calculated with I solar radiation power input, W_{out} electrical power out - and W_{in} input as follows:

$$\eta_{STH} = \frac{\dot{W}_{out} + \dot{W}_{in}}{\dot{I}} = \frac{j_{photo}(V_{redox} - V_{bias})}{\dot{I}}, \qquad (Eq\ 3.16)$$

At around 298K V_{redox} is about 1.23 V in neutral conditions. Without applied bias (V_{bias}=0 V) and at a solar radiation of AM 1.5G (I=1000 W) STH is directly calculated from the photocurrent j_{photo} [mA/cm^2] with: [10]

$$\eta_{STH} = 1.23 \cdot j_{photo}, \qquad (Eq\ 3.17)$$

The evolution rate of O_2 and H_2 defined in mol·h^{-1} and mol·h^{-1}·g^{-1}.

Besides STH, some publications use quantum yield (QY) and quantum efficiency (QE). with further differentiation into apparent, internal, and external.

According to IUPAC – definition, QY and QE can be used interchangeably in case of a primary photochemical process, an elementary chemical process undergone by an *electronically excited* molecular entity and yielding a *primary photoproduct*.

Quantum yield, Φ is defined as:

Number of defined events occurring per photon absorbed by the system. The quantum yield is:

$$\phi\ (\lambda) = \frac{number\ of\ events}{number\ of\ photons\ absorbed}, \qquad (Eq\ 3.18)$$

For a photochemical reaction:

$$\phi(\lambda) = \frac{amount\ of\ reactant\ consumed\ or\ product\ formed}{number\ of\ photons\ absorbed} (Eq\ 3.19)$$

The term quantum yield applies only for monochromatic excitation.[48]

The apparent quantum yield (AQY) or external quantum yield (EQY) is calculated by dividing the measured rate of product formation by the rate of photon absorption, multiplied by the number of electrons transferred photocatalytically. [1]

$$AQY[\%] = EQY\ [\%] = \frac{number\ of\ reacted\ electrons}{number\ of\ incident\ photons} \cdot 100\%, \qquad (Eq\ 3.20)$$

Since the rate of absorbed photon, especially by suspensions of particulate photocatalysts is difficult to measure, for the AQY it is assumed that all incident photos are absorbed by the photocatalyst. AQY varies with light intensity and wavelength and is, is according to definition, measured at monochromatic wavelengths.[49]

The internal quantum yield (IQY) or true quantum yield (QY) is defined as the ratio of the number of charge carriers collected by the solar cell to the number of photons absorbed by the cell and is related to EQY [50].

$$IQY[\%] = QY\ [\%] = \frac{number\ of\ reacted\ electrons}{number\ of\ absorbed\ photons} \cdot 100\% = \frac{EQY}{1 - R - T} \cdot 100\%, (Eq\ 3.21)$$

Faradaic efficiency (FE) In the H_2 evolution reaction , faradaic efficiency is defined as the ratio of the experimentally detected amount of objective gas to the amount of theoretically generated gas [51].

To quantify the catalytic activity the units turnover number and turnover frequency are used. The turnover number (TON_{cat}) is a product generation rate, defined as the number of moles of product per mole of catalyst per unit time and turnover frequency (TOF_{cat}) is a unit of the product generation rate, given as the number of moles of products, produced per mole of catalyst in the system and per unit time [1]. Long term stability and durability of the photocatalyst are also important metrics to evaluate H_2 production performance [43].

3.6.3. Basics of photocatalytic water splitting and photocatalytic schemes

The photocatalytic water splitting process only utilizes light and a particulate photocatalyst to split water, in an endothermic process, under mild conditions into gaseous H_2 and O_2. This is expressed in 2 half reactions:

$$\boldsymbol{OER}:\ 2H_2O + 4h^+ \longrightarrow O_2 + 4H^+ \quad E^0(pH\ 7) = (0.82V)$$

$$\boldsymbol{HER}:\ 2H^+ + 2e^- \longrightarrow H_2 \quad E^0(pH\ 7) = (-0.41\ V)$$

$$H_2O + h\nu \rightarrow H_2 + \frac{1}{2}O_2 \quad \Delta G^0_{(298K)} = +273kJ\ mol\ (H_2O)^{-1}\ (Eq\ 3.22)$$

In theory, the conversion of photonic in chemical energy in an overall water splitting reaction is a 3-step process:

First of all, electron – hole pairs are created when the incident light energy on the photocatalyst is equal or greater than the bandgap (E_g), the potential between the valence band (VB) and conduction band (CB) of the photocatalyst. The electron is lifted to the conduction band into an excited state, creating a hole in the valence band of the photocatalyst. To allow for overall water splitting the conduction band minimum (CBM) must be more negative than the reduction potential of H^+ to H_2 ($E_{H+/H2}$., -0.41V vs. NHE at pH=7) and the valence band maximum (VBM) more positive than the oxidation potential of H_2O to O_2 ($E_{H2O/O2}$, 0.82V vs. NHE at pH=7).

Then in a second step, after irradiation, photogenerated holes and electrons migrate to the surface. The generated electron – hole pairs recombining to a large part, releasing heat or light. This is followed, thirdly by a catalytic redox reaction on the surface active sights, oxidizing water on the VB and reducing H^+ on the CB as seen in Fig. 6 (a) and (b). [49]

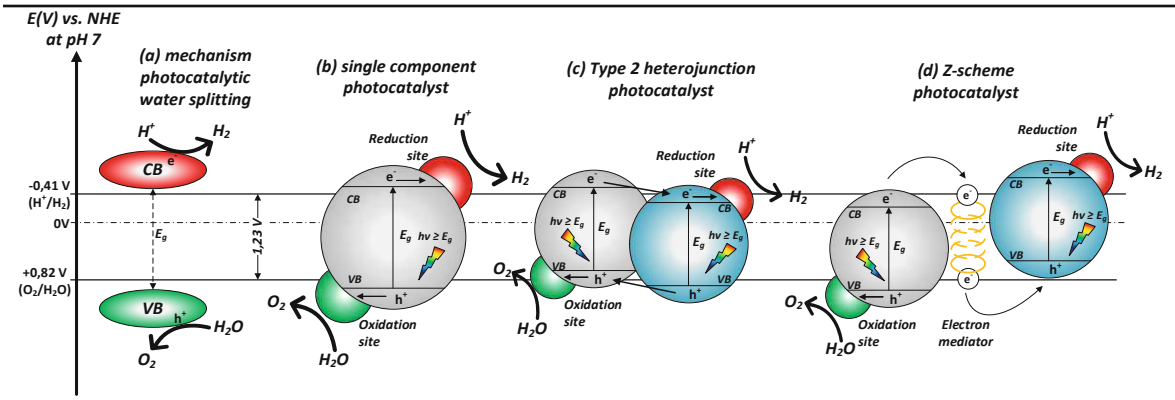

Fig. 6 Overall water splitting scheme and the mechanisms of the 3 main categories of photocatalysts.

A single component photocatalyst should have a small enough band gap to be activated by low energy light and possess sufficient CB and VB potential, a strong redox potential, to allow for unassisted overall water splitting. Achieving these mutually exclusive requirements poses a significant challenge in the development of single component photocatalysts. Also, single-component photocatalyst suffer from rapid recombination of photogenerated electron–hole pairs. [52]

To overcome these shortcomings, heterojunction, and Z-scheme photocatalysts have been developed as shown in Fig. 7(c) and (d). Here two 2 separate photocatalyst, with different edge band potentials are combined by either interfacial electron transport – heterojunctions or some kind of electron mediator, into a Z-scheme photocatalyst, allowing for better charge separation if the electron transfer occurs quicker than the recombination. In addition, a broader utilization of the solar spectrum is reached by the application of 2 different photocatalysts.

Z-scheme photocatalysts are further categorized by their electron mediator system. *PS-A/PS-D* system uses ionic redox pairs that work reversibly. A photosensitizer–conductor setup - *PS–C-PS* substitutes the redox pair with either a metal conductor, carbon nanotubes or carbon quantum dots. The next step was the development of a mediator free *PS-PS* Z-scheme photocatalyst. Here the solid-solid contact interface develops an internal electrical field for vectorial, interfacial, electron flow. The main difference to heterojunctions lies the in the vectorial electron flow that occurs by the simultaneous generation of holes upon excitation by light forcing the photogenerated electron from PS2 to combine with the holes from PS1. This allows for stronger redox abilities and a lower change in Gibbs free energy of Z-scheme systems compared to single component and heterojunction photocatalysts. [52]

The Z – scheme is inspired by the most important photocatalytic process in nature – photosynthesis.

3.6.4. Photosynthesis

Water splitting also occurs in nature, for instance, as an intermediate step in photosynthesis. This process captures solar energy and stores it by producing organic carbon compounds and O_2 from light. Hereby electrons from water reduce CO_2 to a (CH_2O) – block for carbohydrate buildup and H_2O is oxidized to O_2. The carbohydrate buildup from CO_2 is split into a light-dependent reaction of photophosphorylation to produce adenosine triphosphate (ATP) and reduced nicotinamide adenine dinucleotide phosphate (NADPH) and the dark reaction to reduce CO_2 to carbohydrates.

$$2H_2O + 8\,photons + 2\,NADP^+ + 3\,ADP + 3\,P_i \longrightarrow 2H^+ + O_2 + 2\,NADPH + 3\,ATP, (Eq\ 3.23)$$

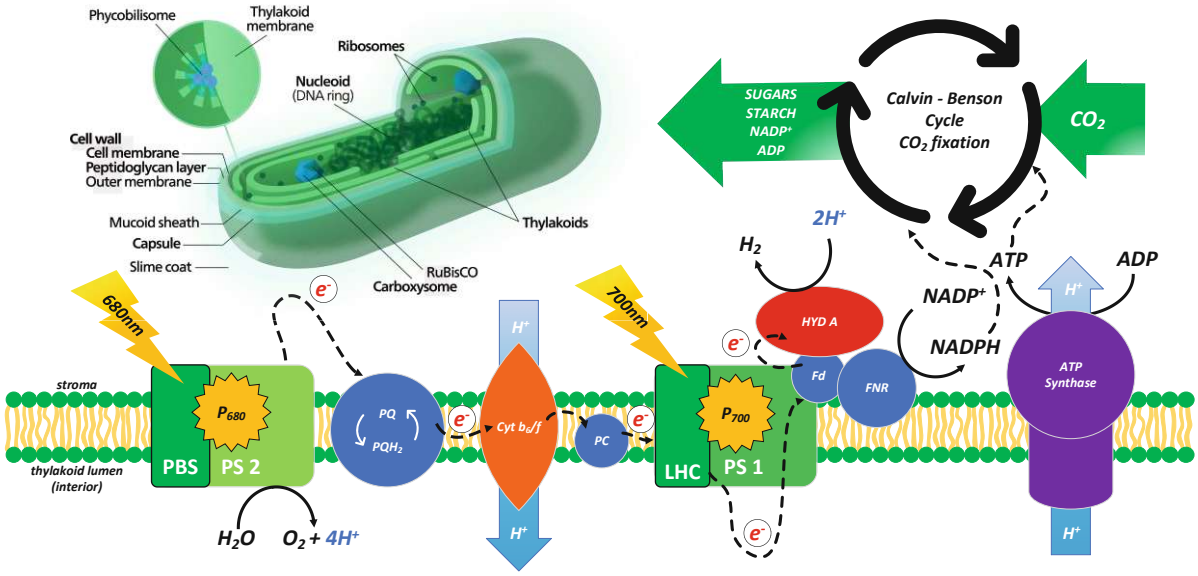

Fig. 7 Photosynthesis - Schematic view of a thylakoid membrane of a cyanobacteria, own work + 3D - model cyanobacteria by Kelvin song - CC BY-SA 3.0[53]

Prokaryotic cyanobacteria and eukaryotic green algae have different photosynthetic active centers. Cyanobacteria have thylakoid membranes located in the cytoplasm and eukaryotic algae cells in the organelles called chloroplasts. The thylakoid membrane is a bilipid membrane that separates the inner "lumen" from the outer "stroma" side and carries the light-harvesting antennae or light-harvesting complex (LHC), the photoreaction centers photosystem 1 (PS1) and photosystem 2 (PS2), cytochrome b_6/f and ATP synthase. [54]

The light harvesting antennae deliver photons to PS1 and PS2 over multiprotein complexes such as chlorophylls, carotenoids, or phycobilisomes. A photon excites chlorophyll P680 in PS2 and creates a e^- hole oxidizing H_2O to molecular O_2. The e^- is shuttled by multiple redox carriers inside the lipid membrane from the excited P680*over cytochrome b_6f to chlorophyll P700 in PS1, creating a proton H^+ gradient for ATP synthesis. In PS1, light excites a e^- to P700*, which again by multiple redox mediators and after an intermediate step at a ferredoxin protein complex, powers NADP reductase to convert $NADP^+$ to NADPH. [54], [55]

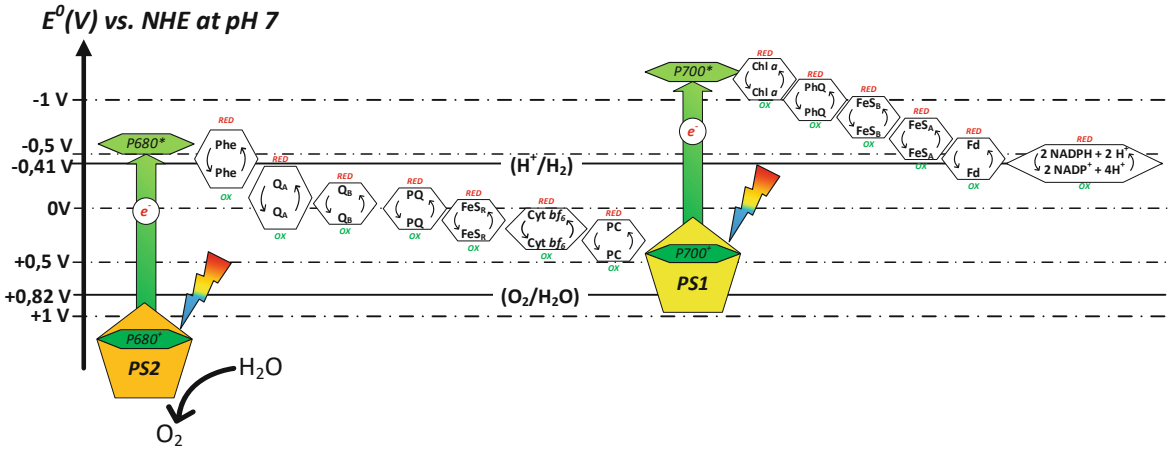

Fig. 8 Schematic Z-Scheme electron transfer in oxygenic phototrophs

This gives a theoretical quantum yield of 12.5%, since 2 NADPH are needed for the reduction of one CO_2 and the reduction of $NADP^+$, two e^- required, which again need two photons for transport from H_2O to $NADP^+$ [54].

The dark reaction, also known as the Calvin-Benson-Bassham cycle and described as follows:

$$CO_2 + 2NADPH + 3\,ATP + 2H^+ \xrightarrow{RuBisCO} (CH_2O) + 2NADP^+ + 3\,ADP + 3P_i + H_2O, (Eq\ 3.24)$$

As this thesis is mainly focused on photocatalytic water splitting for H_2 production, the Calvin-Benson-Bassham cycle won't be further discussed here.

Natural photosynthesis can reach a QE of 100%, in terms of electrons formed by incident photons. However, photosynthetic organisms have evolved with energy consuming self-repair mechanisms to deal with photodamage after prolonged or high intensity light exposure. This lowers the saturated photosynthetic efficiency to about 20% of total solar intensity and to a solar to biomass conversation efficiency of 1-2% for photosynthetic microorganism. [55]

3.6.5. Artificial photosynthesis – photocatalytic water splitting

Direct unassisted, bias-free, photocatalytic water splitting has been regarded as the holy grail in green H_2 production, as photocatalytic single bed particle suspension water splitting has the potential to become one of the most cost-effective methods to produce solar H_2. However, it still requires technical progress. [31]

Today, there is a wide range of artificial, suspended photocatalysts capable of overall water splitting. Typical photosensitizers are semiconductors such as $SrTiO_3$[56], [57] $BiVO_4$[56], C_3N_4[58], [59], $Y_2Ti_2O_5S_2$[60] reaching QE up to 96%[61] used. In combination with co-catalysts Ru/Cr_2O_4[62], Pt [58], cobalt compounds such as $Co(OH)_3$[58] and carbon dots STH efficiencies of up to 2% have been achieved [63]. A g-C_3N_4/carbon dot suspended catalyst was tested for 4800 h with a 98% retention of its initial H_2 evolution rate [63]. A single component CoO-nanoparticle catalyst achieved 5% STH but suffered a quick deactivation within one hour. Deactivated particles started to aggregate. Preliminary study of the particle surface suggests corrosion or oxidation [64].

Most of these catalysts are in their proof of concept – Technology Readiness Level (TRL) 3 – phase. However, Goto et al. constructed in 2018 a 1 m^2 panel with an Al-doped $SrTiO_3$/ $RhCrO_x$ catalyst and reports a runtime of 1000 h with an 64% initial H_2 evolution rate. As challenges in the development of particulate photocatalytic systems Goto et al. listed several points [65]. To ensure effective light harvesting, the particles should not be localized to one area and therefore, a level or perfectly stirred system is necessary, a sturdy construction to carry the load of even a thin layer of water – in case of 1cm thick layer of water, this already amounts to 10 kg per m^2 and the separation and capture of the suspended powder. They achieved a STH of 0.4% [65]. In 2020 a Japanese team constructed a 100m^2 pilot scale (TRL 5) with an immobilized SrTiO3:Al| Rh/Cr_2O_3- CoOOH catalyst. The system operated at ambient pressures and temperatures up to 34 °C. The produced pure oxyH_2 gas was separated by a hollow fiber membrane under vacuum suction, producing 94 vol% H_2. To ensure safe operation all system components were subjected to a detonation test to avoid damages in case of sudden ignition of the oxyH_2 gas. The system ran for 1600 h with 80% retention of initial photocatalytic capability. Peak STH of 0.51% was reached on a warm sunny day in September at noon. **A net-energy gain was not achieved![62]** A newer concept also incorporates H_2 with water sanitation utilizing a TiO_2–CuO catalyst with glycerol as a sacrificial agent with *E.coli* as a microbiological contaminant achieving a max. STH of 0.9% in a pilot scale experiment. The anoxic conditions in tandem with solar irradiation showed significant (>5 log) reduction in *E.coli* concentration in less than 10 minutes of treatment[66].

Artificial photosynthetic systems for water splitting								
Photo-catalyst	***co-catalyst***	***Educt/ Product***	***Absorp-tion edge***	***Output / Performance***	***Durability [h] (retention %)***	***SYSTEM***	***YEAR***	***REF.***
C_3N_4	carbon dots	Water / H_2, **overall water splitting**	*450*	fresh water *AQE (420nm) = 16%*, STH = **2.0%** sea water, (4. ×10−3 $g_{CDots}/g_{catalyst}$) *AQE (420 nm) = 3.86%* ,**STH =0.45%**	4800 (~98)	*TRL 3,* suspended particles	*2015*	[63]
g-C_3N_4	Pt, PtOx, and CoOx	Water / H_2, **overall water splitting**	*~430*	*AQY (405nm) = 0.3%*	510	*TRL 3,* suspended nanosheet particles	*2015*	[59]
SrTiO3:La, Rh;	$BiVO_4$:Mo	Water / H_2, **overall water splitting**	-	*AQY (419nm) = 33%),* **STH=1.1%**	10	*TRL 3,* photocatalytic sheet	*2016*	[57]
$SrTiO_3$:La, Rh/C/$BiVO_4$:Mo	Ru/Cr_2O_4	Water / H_2, **overall water splitting**	*520*	*AQE (419nm) = 26%,* **STH=1%**	17	*TRL 3,* photocatalytic sheet	*2017*	[56]
aza - CMP / C_2N	Pt, $Co(OH)_2$	Water / H_2, **overall water splitting**	*610*	*AQE (600nm) = 4,3%,* **STH =0.23%**	32 (~88)	*TRL 3,* photocatalytic sheet	*2017*	[67]
Al-doped SrTiO3 (SrTiO3:Al)	RhCrOx	Water / H_2, **overall water splitting**	*365*	*AQY= 56%±3% (365nm),* **STH=0.4%**	1000 (~64)	*TRL 4,* immobilized powder	*2018*	[65]
$Y_2Ti_2O_5S_2$	Ru/Cr_2O_4, IrO_2	Water / H_2, **overall water splitting**	*650*	*AQE = 0.05% at 600nm,* **STH = 0.007%**	20 (~81)	*TRL 3,* photocatalytic sheet	*2019*	[60]
Al - doped $SrTiO_3$ ($SrTiO_3$:Al)	Rh/Cr_2O_3 CoOOH (photode-position)	Water /H_2, **overall water splitting**	*390*	*AQE = 96% at 350-360nm*, **STH=0.65%**	12,5 (94)	*TRL 3,* nanoparticles	*2020*	[61]
LaOCl/PCN	Pt and CoO_X	Water / H_2, **overall water splitting**	*430*	-	25 (100)	*below TRL 3* not clear	*2020*	[68]
B-doped, N-deficient C_3N_4	Pt, $Co(OH)_3$	Water / H_2, **overall water splitting**	*500*	*AQE (420nm) = 11.76%,* **STH = 1.16%**	24 (~90)	*TRL 3,* 2D - nanosheets	*2021*	[58]
Al - doped $SrTiO_3$ ($SrTiO_3$:Al)	Rh/Cr_2O_3 CoOOH (impreg-nation)	Water / H_2, **overall water splitting**	*390*	**STH=0.51%**	1600 (~80)	*TRL 5,* photocatalytic sheet	*2021*	[62]
$PtO_x/Nd_2Ta_2O_5N_2$	PtO_x/WO_3	Water / H_2, **overall water splitting**	*620*	*AQY (420nm) = 0.47%* **STH=0.4%**	-	*TRL 3,* suspended particles	2022	[69]
CoO nanoparti cle	none	Water / H_2, **overall water splitting**	-	**STH = 5%**	0.5 deactivation with 1h	*TRL 3 suspended particle*	2015	[64]

Tab. 6 Artificial photosynthetic systems for water splitting

3.6.6. Photoelectrochemical H_2 production PEC

A photoelectrochemical PEC cell consists of semiconductors acting as photo electrode separated by a proton exchange membrane in a cell filled with an aqueous electrolyte. N- type semiconductors, providing surplus electrons act as photo anodes and p-type semiconductors, providing excess electron holes as photo cathodes. In general, there are 3 groups of PEC cell designs, single photoelectrode, photoanode and -cathode and PV supported PEC devices. The cell voltage of both half-cells can be added to provide sufficient potential for the water splitting reaction. Application of 2 different photoelectrodes with different band gaps allows for a broader capture of the light spectrum. Separated by a proton exchange membrane (H_2 and O_2 are produced in separated compartments no further purification steps are needed. Theoretical STH efficiencies of 29.7% could be reached [70]. However unbiased dual photoanode/photocathode systems only achieve STH <1 % and PV integrated systems achieved up to 19.3% STH [71]. PEC Systems are still in the pilot stage of development, reaching STH of 1.7% [72]. Challenges remain the development of cost efficient semiconductor materials with low bandgap potential and stability needed for water splitting. An in depth review and comparison of PEC systems was written by Ahmed et al. [73].

3.7. Semi - artificial photosynthesis

Semi–artificial photosynthesis is a hybrid biological–material approach for solar to chemical energy conversion. This not only covers artificial water splitting, but also CO_2, N_2 reduction and further reactions. Semi-artificial photosynthetic systems (SAPSs) are an attempt to combine the strength of artificial and natural photosynthetic components with biobased, biomimetic or synthetic catalysts to optimize light capture, reduce substrate activation barriers, improve catalytic activity and efficiency, increase the diversity of products and lifetime/stability of the components. Biological components offer advantages with high QE, low overpotential and high product selectivity, while synthetic components tend to be more stable and have a wider range of light absorption. This leads to a wide range of possible combinations of light capture systems, the photosensitizers, like organic light-active molecules, semiconductors, and catalytic systems such as enzymes, semiconductors, and cells to drive a solar to chemical energy conversion using basic building blocks such as CO_2, H_2O and N_2, to produce not only H_2 but also carbon and N_2-based H_2 carriers like formate, ammonia and methanol [55], [74].

All SAPSs consist of 3 basic components.:

a. ***A Photosensitizer*** – for energy capture
b. ***Biotic – abiotic Interface*** – for electron transfer
c. ***Catalytic center - for energy conversion***

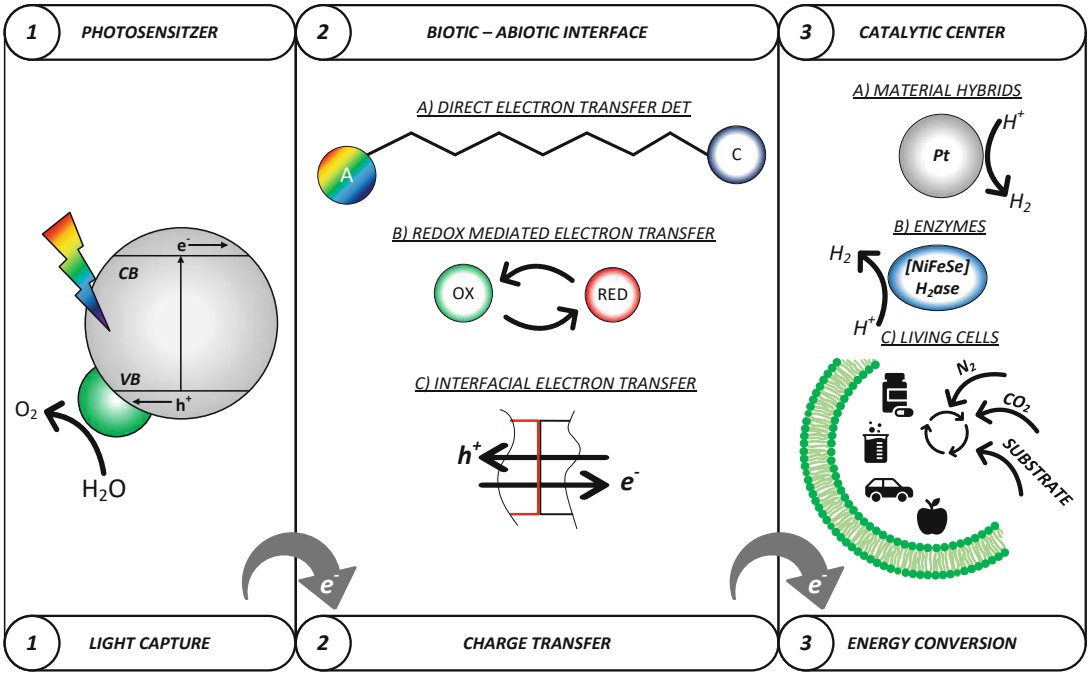

Fig. 9 Basic components of SAPSs

The task of the photosensitizer in SAPSs is the light capture and production of electrons or redox carriers with a sufficient electrochemical potential to drive the reaction at the catalytic center. The requirements are similar to those of artificial photosynthesis. A small bandgap allows excitation by low wavelengths or low energy of the impacting light and a sufficiently high valance band maxima that are higher than the oxidation potential of the half-reaction as well as a conduction band minimum lower than the reduction potential of the other half-reaction. To prevent the recombination of the generated electron-hole pair, the photoactive center should provide a long-activated state and be connected with a sufficiently fast charge carrier for quick electron transmission.

3.7.1. Photosensitizers:

Photosensitizers such as bio photosensitizers, organic dyes and semiconductors have been used. Bio photosensitizers are biological complexes allowing photosynthesis in nature such as PS1, PS2, thylakoid membranes[75], [76] and bacteriorhodopsin (bR) [77]. Organic dyes produce, compared to semiconductors, charge carriers with a different mechanism. They don't rely on the typical bandgap mechanism of semiconductors but use electron–donor/acceptor pairs that shuttle to electrons through a metal - to – ligand (Ru-polypyridyl (ppy) complexes) or a π – conjugated C=C backbone (porphyrin) by photoexcitation. There are synthetic dyes such as Ru-ppy complexes or DPP[78] and xanthenes like Eosin Y and natural dyes like porphyrins and flavins. Semiconductors are synthetic materials capable of producing photoelectrons after photoexcitation. Typical examples in SAPSs for H_2 production are carbon nanodots, CdS, CdTe, In_2S_3, TiO_2 and g-C_3N_4.

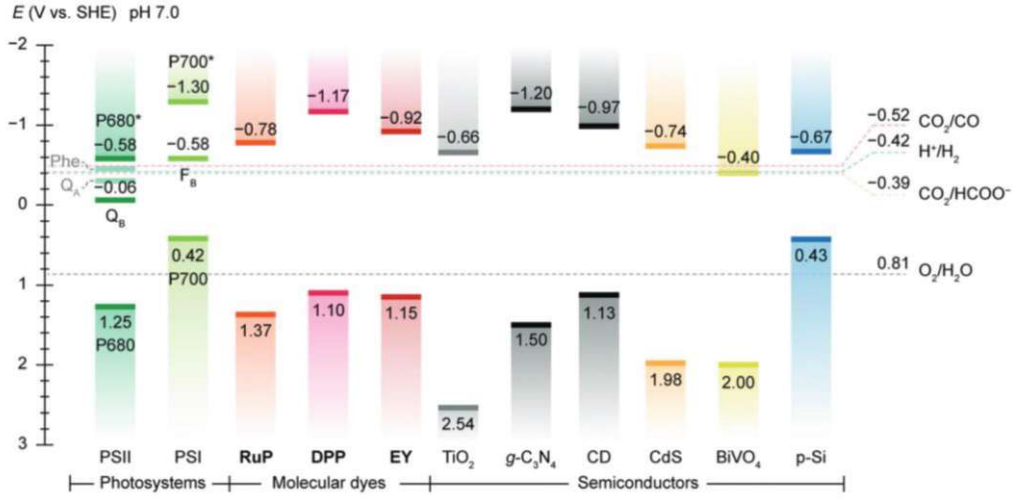

Fig. 10 Energy band edges of light absorbers used in semi-artificial photosynthesis. Reproduced from Semi-biological approaches to solar-to-chemical conversion X. Fang, S. Kalathil and E. Reisner, Chem. Soc. Rev., 2020, 49, 4926 DOI: 10.1039/C9CS00496C with permission from the Royal Society of Chemistry under CC-BY 3.0 .Source:[74, p. 4]

3.7.2. The Catalytic Centers

The catalytic centers allow a first classification of SAPSs into cell-free and cell-based SAPSs. Cell-free SAPSs either use naturally occurring enzymes, enzyme hybrids, which are modified enzymes to increase stability or overcome limitations, material hybrids and biomimetic complex hybrids. Cell bases systems use whole living cells as catalytic centers taking advantage of the internal metabolic pathways and enzyme networks to produce more complex products. The cells are either powered by a suspended photocatalyst/dye or are directly coated by a photocatalyst. The catalytic center for SAPSs should be highly efficient, stable under the reaction environment, simple to isolate, highly selective and work with basic educts like H_2O, CO_2 and N_2. The choice of the catalytic center allows for select/desired products. Enzymes are highly efficient catalysts with low activation potential. Enzymes used for SAPSs are H_2ase (H_2ase) for water splitting, carbon monoxide deH_2ase (CODH), formate deH_2ase (FDH), N_2ase (N_2ase) for N_2 reduction, flavoenzyme fumarate reductase (FccA) for the reduction of C=C bonds. Photochemical C-C bond formation can be realized with a CdS-2-oxoglutarate: ferredoxin oxidoreductase (OGOR) system. [55], [74]

SAPS							
System	***cell free SAPSs***					***Cell based SAPSs***	
PHOTO - SENSITZIER	*Bio - photo-sensitizer*	*Dye*	*Semi-conductors*	*Photo-sensitizers*	*Biophoto-sensitizers*	*Photo-electrodes*	*Nanoparticles*
	+	+	+	+	+	+	+
CATALYTIC CENTER	*material hybrids*	*enzymes*	*enzymes*	*biomimetic complex*	*enzymes*	*living cells*	*living cells*
PRODUCTS	$H^+ \rightarrow H_2$ ATP synthesis Fatty acids → hydrocarbons	$H^+ \rightarrow H_2$ $CO_2 \rightarrow$formate	$H^+ \rightarrow H_2$ $CO_2 \rightarrow CO$ $CO_2 \rightarrow$formate $N_2 \rightarrow NH_3$	$H^+ \rightarrow H_2$ $CO_2 \rightarrow CO$ $CO_2 \rightarrow$formate $CO_2 \rightarrow$methanol	$H^+ \rightarrow H_2$	$H^+ \rightarrow H_2$ $CO_2 \rightarrow$isoproanol $CO_2 \rightarrow$methane $CO_2 \rightarrow$acetate $CO_2 \rightarrow$butanol, hexanol $CO_2 \rightarrow$PHB, carotenoids Glucose→shikimic acid Fumarate → succinate $N_2 \rightarrow NH_3$	

Fig. 11 Classification of SAPSs Sources:[55], [74]

Photoelectrical cells (PECs) separating the anode and cathode reactions [33] and suspended particle reactors, similar to PC -systems [77] are the 2 two architectures of cell-free SAPSs.

3.7.3. The Biotic A-Biotic Interface

The biotic–abiotic interface covers 2 topics. First, the connection between the photosensitizer and/or catalytic center with the charge transfer system, for example, efficiently connecting an enzyme to an electrode and secondly, the charge transfer mechanism between the photosensitizer and catalytic center.

There are 3 different charge transfer mechanisms, *direct electron transfer (DET)* by a covalent chemical bond such as a molecular wire[79], *redox-mediated systems* using methyl viologen[80], ferrocyanide-ferricyanide redox couple [81], redox polymers[82], reduced graphene oxide[83]and *interfacial electron transport* such as Förster resonance energy transfer[84].

Efficiently connecting the photosynthetic molecules or enzymes to the charge transfer system is crucial for the performance of the SAPS. For the construction of **SAPSs with a PEC-protein film architecture**, the immobilization of the photosynthetic proteins or catalytic enzymes with correct orientation on electrodes was a key challenge. For the example of PS2 immobilization, there have been three generations of electrodes described. First-generation electrodes were constructed of either self-assembling monolayer or redox polymer matrices. The first electrodes were Au – electrodes covered in monolayers with His-tagged PS2 [85]–[87]. Since intra-protein electron transfer depends on the correct orientation of the protein directly [74] Os-containing poly(vinyl)imidazole-based methyl viologen [88] redox polymer matrices were developed that act as electron acceptors and immobilization matrices. They are capable of shuttling electrons from a reactive site within an immobilized redox protein towards an electrode surface regardless of the orientation of the protein [89].

Second-generation electrodes – mesoporous film electrodes - are made of metal oxides such as visible light transparent, indium tin oxide (ITO). The surface of mesoporous - ITO can be modified to covalently bind PS2 in the correct orientation at high surface loadings of up to 19 pmol PS2 cm^{-2} [90], [91]. The third generation of electrodes - increased the surface by creating a 3D scaffold. These inverse opal (IO) electrodes have meso- and microporosity and are made of semiconducting hydrophilic nanoparticles (TIO_2 or ITO) capable of adsorbing proteins. This allows for higher PS2 / protein loadings, improved mass transport and light transmission.

For **photocatalytic (PC) suspended SAPSs** particles, the following designs have been described. Colloidal suspended semiconductor particles with attached enzymes and possible additional photosensitizers such as TiO_2 nanoparticles with a RuP photosensitizer and attached [NiFeSe]-H_2ase[92], [93], or CdTe nanoparticles with [FeFe]-H_2ase. Or suspended liposomes or vesicles fused with a material hybrid as catalytic center such as *Halobacterium salinarum* purple membrane-derived vesicles (PMVs) containing bR, fused with palladium-deposited porous hollow TiO_2 nanoparticles (Pd-HTNPs) for CO_2-reduction [77]. Also dissolved photosynthetic dyes, with an soluble redox mediator and suspended particular H_2 evolution catalyst are possible [78].

For **cell-bases SAPSs,** a classification into photoelectrode cell hybrids, where a photoelectrode for light harvest is coupled with a cell as a catalytic center and light capturing nanoparticle-cell hybrids. Both approaches are further separated in to “integrated” SAPSs, the cells are in direct contact with the photosensitizer or separated in “suspended” SAPSs connecting the photosensitizer via redox mediator with the cells.

The following overview will focus primarily on H_2-producing SAPSs. A detailed in depth-look into non-H_2 experiments can be found in the Reviews *“Panoramic insights into semi-artificial photosynthesis: origin, development , and future perspective”* of Kenmeng Xiao et al.[55] and *“Semi-biological approaches to solar to chemical conversion”* by Xin Fang et al.[74]. The performance of SAPSs roughly

categorized into SAPS capable of unassisted overall water splitting (OWS), without applied bias and sacrificial electron donors and assisted water splitting (AWS).

3.7.4. Bio photosensitizer – Material hybrid SAPSs

PS1 is a powerful bio photosensitizer thanks to its high QY of close to 1. It provides sufficient driving force to reduce protons to H_2 in neutral conditions with an electrochemical potential of -580 mV (vs NHE) at terminal electron accept Fb (a [4Fe-4S] cluster) and its long-lived (about 60ms) charge-separated state [76].

First SAPSs designs consisted of a suspended plastocyanin crosslinked PS1 – dithiol molecular wire - Pt-nanoparticle bioconjugate. This system achieved in Na-ascorbate assisted water splitting (AWS) a rate of 312 µmol H_2 mg Chl^{-1} h^{-1}. This study showed that different PS1 sources have varying chlorophyll to P700 ratios leading to higher optical cross-sections and to higher rates of H_2 production, provided no limitations by other rate-limiting steps at non saturating light intensities. By chemical crosslinking the plastocyanin to PS1, the diffusional rate limitation could be eliminated by avoiding diffusion-based electron transport, increasing H_2 production by a factor of 2. As for ionic dependence of light-induced H_2 evolution, they report relative independence on NaCl and $MgCl_2$ – concentration. However, at higher $MgCl_2$, the bioconjugate flocculated. The bioconjugates generated H_2 with higher rates at lower pH value. As for the effect of the molecular wire length and bond on H_2 production the fastest rate was found using the aromatic wire 1,4 benzene dithiol. The rate dropped when a second aromatic ring was added. This bioconjugate with aliphatic molecular wires showed a lower rate than a conjugated bond of similar length. The H_2 production decreased with the length of aliphatic dithiols. However, short molecular wires may not allow for efficient covalent linkage between PS I and the Pt nanoparticle and decrease the effectiveness of preventing denaturation of the proteins on the metal surface. Full light saturation hasn't been reached [30].

A simpler design of a PS1 - Pt SAPS design - PS1 trimers *from Thermosynechococcus elongatus* platinized themselves by photoexcitation in a photobioreactor in a MES buffered - $Na_2[PtCl]_6$ salt solution. The H_2 production rate increased as the platinization process proceeded. Assisted H_2 production was also achieved with the reisolated platinized PS1. The influence of temperature, light intensity, platinum salt concentration and temperature, as well as the light color during the platinization on the H_2 were investigated. Using response surface methodology, the max H_2 yield was calculated at 8.02 µmol H_2 mg Chl^{-1} h^{-1} [94].

A similar set-up was used when a PS1-Pt nanoparticle complex was immobilized with a poly(vinyl)imidazole $Os(bispyridine)_2Cl$ redox polymer embedded in a hydrogel to create a bio photocathode. A photocurrent of 4.8 ± 0.4 µAcm^{-2} with an applied bias of 150 mV H_2 production was witnessed. The properties of the redox hydrogel depend strongly on the presence of the Pt-nanoparticles [82].

PS1/Pt system was also used in combination with Lumogen Red, an artificial light-harvesting dye. Lumogen Red acts as an additional light harvester and transfers the energy to PS1 by Förster resonance energy transfer (FRET), Pt nanoparticles act as H_2 evolution catalysts. Lumogen Red and PS1 have complementary, but still slightly overlapping, light absorption spectra increasing light harvesting yet allowing for FRET increasing H_2 production rates. The system used an ascorbic acid as SED and DCIP as electron mediator, realizing a H_2 evolution rate of 26.3 mol H_2 (mol PSI)$^{-1}$ h^{-1}. The system ran for 12 hours [84].

Even though water oxidation is regarded as one of the bottlenecks in water splitting because it involves multiple bond rearrangements between molecules that have to be synchronized with the removal of electrons and protons to avoid the formation of rate-retarding, high-energy intermediates [95]. Hereby, at ambient conditions, PS2, as nature's water oxidation enzyme sets a benchmark. Its QE close to 1 and its low overpotential makes PS2 an interesting photosensitizer for SAPSs [96]. An

additional advantage especially in a Z-scheme system is provided by PS2, as it absorbs at longer wavelengths than most other oxygen evolution catalysts [97].

PS2 has been immobilized on a mesoporous indium-tin oxide (mesoITO) electrode to increase protein coverage 26-fold compared to an ideal monolayer allowing for DET from PS2 to mesoITO. A mechanistic study showed that interfacial electron transfer also occurs from the quinone Q_A through an unnatural electron transfer pathway to the electrode surface and not only from the terminal quinone Q_B [91].

The first attempt on a solar overall water splitting with PS2 was made with a hybrid system of plant PS2 and Ru/$SrTiO_3$:Rh connected by an inorganic electron shuttle [$Fe(CN)^{3-}_6$ /$Fe(CN)^{4-}_6$] dispersed in an aqueous solution. PS2 hereby self-assembles onto the surface of the photocatalyst. Water splitting was achieved under visible light irradiation reaching rates of 2.489 mol H_2 (mol PS2)$^{-1}$ h^{-1} showing that hybrid systems reach higher efficiencies compared to PS2 systems. The isolated PS2 membranes were damaged when illuminated for a few hours by the effects of photo-oxidative stress on the protein structure [81].
In order to spatially separate H_2 and O_2 evolution – a PEC cell with a photoactive platinum-decorated silicon cathode and an anode compartment with solubilized PS2 with an $[Fe(CN)_6]^{3-}$/$[Fe(CN)_6]^{4-}$ redox mediator to connect to the anode was designed. The system is limited by the performance of the Si cathode. The 2 compartments are separated by a NAFION proton exchange membrane. As Si absorbs light at shorter wavelengths compared to PS2 the 2 photosensitizers should complement each other for better utilization of incident light. This artificial Z- scheme setup achieved unassisted overall water splitting at STH of 0.29% [81].

As the purification of PS1 and PS2 is a complex, expensive process, systems based on thylakoid membranes have been developed.

Self-assembly of PT nanoparticles with spinach thylakoid membranes was studied. By applying a sacrificial electron donor and by blocking electron transfer from PS2 with 1mM DCMU, rates of 4 µmol H_2 (mg Chl)$^{-1}$ h^{-1} were achieved. In full Z-scheme operation without SED and DCMU, the rates dropped to 0.1 µmol H_2 (mg Chl)$^{-1}$ h^{-1} and 2 µmol O_2 (mg Chl)$^{-1}$ h^{-1}. One would expect a 2:1 ratio of H_2 and O_2 for full water splitting, yet a 1:20 ratio was observed. This could be the result of the low efficiency of electron flow from PS2 to PS1 because of the complex electron transfer chain in the thylakoids. By adding an excess of the mediator protein cyt c_6, a shuttle protein that donates an electron to $P700^+$, the H_2 production increased threefold. A similar system was created with cyanobacterial thylakoids – as the cyanobacterial membrane preparations in this experiment do not contain plastocyanin, cyt c_6 was added to help mediate the reduction of $P700^+$. For *S. leopoliensis* 14 µmol H_2 (mg Chl)$^{-1}$ h^{-1} for 4 h with SED and 0.4 µmol H_2 (mg Chl)$^{-1}$ h^{-1} for the first 2h without SED have been with a H_2:O_2 ratio close to 1:1 have been observed. EPR spectroscopy was used to explore light-induced electron transfer reactions showing that Pt nanoparticles mimic acceptor protein binding to PS1. To prove efficient and scalable photosynthetic H_2 production, further experiments with metal molecular catalysts – cobaloxime ($Co(dmgH)_2pyCl$) and nickel diphosphine [Ni ($P_2^{Ph}N_2^{Ph}$)$_2$](BF_4)$_2$ have been successfully linked to a S. leopoliensis thylakoid membrane. For the cabaloxime membranes H_2 production rates of 1 µmol H_2 (mg Chl)$^{-1}$ h^{-1} for 1 h and the nickel diphosphine system 3 µmol H_2 (mg Chl)$^{-1}$ h^{-1} for 6 h inhibited by DCMU and assisted by SED. The nickel diphosphine system achieved unassisted full Z-scheme rates of 0.03 H_2 (mg Chl)$^{-1}$ h^{-1} and 0.5 µmol O_2 (mg Chl)$^{-1}$ h^{-1}. The H_2 production rate suggests, that some of the synthetic catalysts binds near the protein surface on the acceptor end of PS1. [76]

A unique setup for a bio-photo-electro chemical cell based on thylakoids lets suspended thylakoids settle as a slurry on a flat transparent FTO anode together with a redox mediator (Fe(III)/Fe(II)CN) to mediate the photocurrent between the thylakoids, the FTO anode and Pt cathode for H_2 production.

This setup allows for easy replacement of photodamaged thylakoids. The replacement was tested in 10 minutes intervals showing only a drop in photocurrent of ~20% between the intervals. H_2 production was possible with an applied BIAS above 0.8 V. In a setup with DCMU inhibiting electron transfer via the redox mediator (Fe(III)/Fe(II)CN) forcing direct electron transfer between the thylakoids and the FTO anode and a solar cell providing the required BIAS potential, mimicking the natural Z-scheme, STH of 0.3% without SED was achieved. The max. photocurrent and power output of the cell was obtained at 80 $mWcm^{-2}$ of illumination, which is lower than 1 sun conditions (100 $mWcm^{-2}$). This decrease is most likely due to photo saturation of the thylakoid membranes. [98]

Besides the classical PS2-PS1 photosensitizer, the proton pump bacteriorhodopsin, a membrane protein can be found in the cell membrane of the extremophile organism like *Halobacteria salinarium*, also known as purple membrane protein. Contrary to the electron pumping system found in chlorophyll, its primary function is the development of a proton gradient between the cytoplasm and surrounding environment to drive ATP synthase. It absorbs light at lower wavelengths, at around 570 nm. A photocycle in bR takes about ~15 ms limiting its photosynthetic performance. This can be reduced by taking advantage of the plasmonic field effect of nanoparticles to modify the photocycle of bR [99]. Since bR is expressed by an extremophile host organism it is stable in a wide pH range, high temperatures and in conditions under high ionic strength without loss of photochemical activity [100].

One of the first experiments to apply bR for photochemical H_2 production used a PEC setup with a bR/TiO_2 nanotube hybrid photoanode. Anchoring bR molecules onto a TiO_2 surface effectively expands the absorption region of TiO_2 from UV to visible light. The hybrid photo anode system was either assembled by physisorption, leading to the random assembly of the 2 components where the binding force between bR molecules and TiO_2 surface is the weakest and a broad undefined absorption spectrum, or by a linker, 3-mercaptopropionic acid, leading to a well-established bR absorption peak, improved absorption intensities and a more stable hybrid cell system. Compared to a pure TiO_2 photoanode, the photocurrent onset is decreased from -0.49 V to -0.56 V and the max. photocurrent density increased by 50%. However, no exact data for H_2 production is presented with this system. [99]

This system has been used to construct a bR|TiO_2||Pt particulate nanocatalyst for H_2 production with methanol as SED in neutral conditions in white light. Under green light, H_2 generation with a turnover rate of 207 µmol of H_2 (µmol protein)$^{-1}$ h^{-1}. A nearly constant rate has been observed under illumination for at least 2.5h. Under white light, the increased by 25 times to 5275 µmol of H_2 (µmol protein)$^{-1}$ h^{-1}. [100]

A very similar nanoparticle system was developed by Wang et al. mimicking nature's bilipid layers environment to express membrane proteins by artificial lipoprotein nanodiscs. Here bR- nanodiscs, TiO_2- and Pt nanoparticles are assembled in a noncovalent way. An in-vitro cell-free expressed synthetic purple membrane (PMsyn) using a nanodisc artificial lipoprotein membrane template and a vector containing a synthetic DNA construct encoding bR hereby expressing in bRsyn monolayers on the nano disc. In the presence of methanol as SED, this system increased the H_2 production rate at 120 mW/cm^2 more than threefold to 17.7 mmol H_2 (µmol protein)$^{-1}$ h^{-1} compared to the work of Balasubramanian et al. under white light. This is 74 times higher than under green light. [101]

A hybrid material liposome-based system was constructed by Chen et al.. By enveloping Pd – deposited hollow porous TiO_2 nanoparticles with purple membrane–derived vesicles from *Halobacterium,* a bR-TiO_2 dual photosensitizer Pd cocatalyst system was constructed for CO_2 reduction. Their results support that incorporation of bR in a closed cytomimetic compartment, bR indeed maintained its native bioactivity. Over time the product selectivity shifted from CO to CH_4 up to 95.2% after 8 h. Ascorbate was used as an electron donor. [77]

SAPS: Bio-photosensitizer + material hybrids 1/2								
Photosensitizer	***Biotic Abiotic Interface***	***Catalytic Center***	***Educt/ Product***	***Performance***	***Lifetime***	***SYSTEM***	***YEAR***	***REF***
plastocyanin crosslinked PS1 (spinach/*Synechococcus*))	Ps1|dithiol molecular wire|Pt-nanoparticle	Pt nano-particles	aqueous buffer Solution (Na - ascorbate) /H_2	**AWS,** 312 µmol H_2 mg Chl^{-1} $h^{-1.}$	No Information	***TRL 3*** suspension	*2009*	[30]
bacteriorhodopsin (bR) *Halobacteria salinarium* / TiO2 nanotube	self-assembly - hybrid electrode system 3-Mercaptopropionic acid as linker molecule and physisorption	Pt Foil	methanol (sacrificial agent) / H_2	**AWS** 0.87 mA/cm^2	No Information	***TRL 3*** PEC	*2011*	[99]
PS1 - *T. elonngatus BP-1*	platinized PS1	Pt	10 mM NaAsc /H_2	**AWS** 8.02 µmol H_2 h^{-1} mg chl^{-1}	24 h of platinization, 12h pure H_2 evolution	***TRL 3*** PEC	*2011*	[94]
PS2	PS2|mesoITO half cell	none - half cell	Water /O_2	**AWS** QY: 0.04 – 0.3% 0.18 ± 0.04 mol O_2 (mol PS_2)$^{-1}$ s^{-1}	half-life time of 4 to 5 min under continuous red-light illumination	***TRL 3*** PEC - half cell	*2012*	[91]
bacteriorhodopsin (bR) *Halobacteria salinarium*	molecular complex	Pt/TiO_2	MeOH (sacrificial agent) / H_2	**AWS** in white light at pH 7 : 5275 µmol H_2 (µmol protein)$^{-1}$ $h^{-1.}$ in green light: 207 µmol H_2 (µmol protein)$^{-1}$ h^{-1}	irradiation time: 90min	***TRL 3***, suspension	*2013*	[100]
PS2	inorganic electron shuttle [$Fe(CN)^{3-}_6$ /$Fe(CN)^{4-}_6$]	Ru/$SrTiO_3$:Rh	Water /H_2	**AWS** 2489 mol H_2 *(mol PS2)$^{-1}$ h^{-1}	120min runtime - Illumination of PS2 at >600nm than >420nm has a positive effect on stability	***TRL 3,*** suspension	*2014*	[81]
PS1	immobilization on Os-complexed-redox hydrogel	Pt	Buffer Solution/ H_2	**AWS**	no information	***TRL 3,*** PEC	*2015*	[82]
PS2 /Si	PS2|redox mediator|Electrode||Si|Pt	PS2 / Pt	Water /H_2	**OWS** 0.29% STH (@ AM 1.5G 100 mW/cm^2)	no information	***TRL 3***, PEC	*2016*	[97]
Spinach Thylakoids (Slurry)	Thylakoid (Slurry)|(redox mediator (Fe(III)/Fe(II)CN)))|FTO||SOLAR CELL/potentiostat||Pt	Pt	Water/H_2	**AWS** STH=0.3% Faradaic efficiency 69±3% EQE=17±4% @ 650-660nm 3.4 - 3.5 µmol H_2 *(mg Chl)$^{-1}$ h^{-1}	Thylakoids were replaced by fresh ones every 10 minutes irradiation for H_2 production for 1200s	***TRL 3*** bio photo electro chemical cell (BPEC)	*2016*	[98]

SAPS: Bio-photosensitizer + material hybrids 2/2								
Photosensitizer	**Biotic Abiotic Interface**	**Catalytic Center**	**Educt/ Product**	**Performance**	**Lifetime**	**SYSTEM**	**YEAR**	**REF**
Synthetic purple membranes PM_{syn} - bacteriorhodopsin (bR_{syn}) *Halobacteria salinarium / TiO_2*	molecular complex	Pt	MeOH (sacrificial agent) / H_2	**AWS** in white light @ ambient conditions, neutral pH: 17.74 mmol H_2 (µmol protein)$^{-1}$ h^{-1} in green light: 240 µmol H_2 (µmol protein)$^{-1}$ h^{-1}	constant H_2 evolution for: 2–3 h	***TRL 3*** suspension	2017	[101]
PS1 - Thylakoids (*S.leopoliensis*)	self-assembly	Pt nano-particles - mercapto stabilized	(Na-ascorbate) buffer solution /H_2	**OWS** **AWS** Full Membrane Z-scheme: With SED: 14 µmol H_2 *(mol PSI)$^{-1}$ h^{-1} Without SED: 0.4 µmol H_2 *(mol PSI)$^{-1}$ h^{-1}	up to 8 hours of runtime	***TRL 3*** suspension	2018	[76]
PS1 - (*T. vulcanus*) + LR (Lumogen Red)	PSI/Pt nanoparticle	Pt nano-particles (PtNp)	ascorbic acid and DCIP / H_2	**AWS** PS1/PtNP + LR: 26.3 mol H_2 (mol PSI)$^{-1}$ h^{-1}	irradiation time: 12 h	***TRL 3*** suspension	2019	[84]

Tab. 7 Bio - photosensitizer + material hybrids

3.7.5. Dye - enzyme hybrid SAPSs

Besides organic photosensitizers of the likes PS1/2 and bR there are also organic dyes capable of light absorption based on a different mechanism [55]. For H_2 production, they are coupled with H_2ase.

In 2009 Reisner et al. constructed a particulate photocatalyst with Rup dye - sensitized TiO_2 - *Desulfomicrobium baculatum* (*Db*)[NiFeSe] – H_2ase nanoparticles. With triethanolamine as a sacrificial electron donor, 50 (mol H_2)s^{-1} (mol total H_2ase)$^{-1}$ at pH 7 and 25 °C, even under the typical solar irradiation of a northern European sky, was achieved. Because of the wide bandgap of TiO_2 (3eV), allowing H_2 production only under ultraviolet light, an additional photosensitizer is necessary for visible light water splitting. A comparison of 5 Pt or Ru dyes, RuP emerged as a suitable photosensitizer because of absorption in the visible spectrum, long-term stability under irradiation, efficient charge separation and excellent absorption on TiO_2. A series of O_2 – tolerant and sensitive H_2ase has been tested with Db [NiFeSe] - H_2ase providing the best performance thanks to its good H_2 production activity, rapid reactivation at low potential after O_2 inactivation and tolerance up to 1% O_2. The system deactivates within hours under irradiation after exposure to air but shows long term stability without irradiation under anaerobic conditions. The assembly of H_2ase to the TiO_2 – nanoparticle is likely controlled by localized polar interactions between sidechain carboxylates and a number of Ti-O(H) sites close to the distal iron sulfur clusters rather than by overall electrostatic interactions improving direct electron transfer. Direct electron transfer rate via TiO_2 is 6 times higher than the one obtained by bi-molecular diffusion controlled when replacing TiO_2 by MV^{2+}. [93]

Another approach constructed a SAPS with dissolved organic Eosin Y dye with dissolved O_2 tolerant [NiFeSe]-H_2ase in a pH–neutral aqueous solution with triethanolamine as SED. Electron are directly transmitted without the need of an electron mediator. The Eosin Y – H_2ase system deactivated within 3 hours of irradiation under a 21% O_2 atmosphere but stayed fully photoactive in anaerobic

conditions. The higher stability of a dye -TiO_2 – H_2ase can be explained by the proximity of the H_2ase to the O_2 evolution site. The system achieved a TOF_{H2ase}=(13.9±0.7) (mol H_2)(mol H_2ase)$^{-1}$ s^{-1}. [102]

Warnan et al. immobilized 5 different modified diketopyrrolopyrrole (DDP)dyes and Ru-tris(bipyridine) (RuP) on either molecular Co and Ni catalyst–TiO_2 hybrids or H_2ase -or Pt-TiO_2 hybrids. The semiconductor nanoparticle acts as a scaffold for the co-immobilization of dye and catalysts and enables efficient charge separation and accumulation of multiple long-lived low- potential electrons for catalytic fuel generation. A RuP|TiO_2|H_2ase hybrid performed at TOF_{RuP} = 25.0 ± 2.5 h^{-1} and DPP_2|TiO_2|H_2ase hybrid performed at $TOF_{DPP\ 2}$= 25.0 ± 2.5 h^{-1} ascorbic acid assisted water splitting. It is outperformed by all DPP2 or RuP|TiO_2|Pt/Ni/Co hybrids, with DPP_2|TiO_2|Pt offering the best performance at 337 ± 33.7 h^{-1} offering the best performance. [78]

Dye + enzyme hybrids								
Photosensitizer	***Biotic Abiotic Interface***	***Catalytic Center***	***Educt/ Product***	***Performance***	***Lifetime***	***TRL / SYSTEM***	***YEAR***	***REF.***
RuP dye sensitized TiO_2	Adsorption of Photosensitizers and H_2ases to TiO_2 direct electron transfer via TiO_2- control experiment with soluble redox mediator MV^{2+}	[NiFeSe]-H_2ase *Desulfomicro-bium baculatum*	aqueous TEOA (electron donor) buffer (4 mL, pH 7, 25 mM) / H_2	**AWS** initial TOF = 50 (mol H_2)s^{-1} (mol total H2ase)$^{-1}$ at pH 7 and 25 °C visible light - enzyme nanoparticle system : 2070 µmol H_2 h^{-1} (mg enzyme)$^{-1}$; 712 µmol H_2 h^{-1} (g TiO2)$^{-1}$ visible light irradiated RuP-sensitized TiO_2 particles loaded with Pt (3% by mass) in a pH 3.0 EDTA buffered solution: up to 10 600 µmol H_2 h^{-1} (g TiO_2)$^{-1}$.	total irradiation time: 4h	***TRL 3***, suspen-sion	2009	[93]
Eosin Y / RuP	Soluble EY and soluble H2ase without redox mediator Eosin EY: direct electron transfer RuP: MV as redox mediator	*Desulfomicro-bium baculatum* (Db) [NiFeSe] H_2ase	TEOA (triethanolamine) or Ascorbic Acid in pH-neutral aqueous solution (Sacrificial agent) |H_2	**AWS** Eosin Y TOF_{H2ase} = (13.9±0.7) (mol H_2)(mol H_2ase)$^{-1}$ s^{-1} RuP TOF_{H2ase} = (27±2) (mol H_2)(mol H_2ase)$^{-1}$ s^{-1}	No photoactivity after 24h linear H_2 evolution rates over 15 hours inactivity in 21%O_2 after 3h	***TRL 3***, Dye and H_2ase in solution without redox media-tor	2013	[103]
DPP 2 / RuP	TiO_2 nanoparticles	Co/Ni-TiO_2 and PT-TiO_2, [NiFeSe]-H_2ase	Ascorbic Acid (pH 4,5) aqueous solution /H_2	**AWS** TON_{DPP}=205 Co/Ni TON_{DPP}=2665 for H_2ase/Pt	runtime 24h	***TRL 3***, suspen-sion	2018	[78]

Tab. 8 Dye + Enzyme hybrids SAPSs

3.7.6. Semiconductor – enzyme SAPSs

Artificial photosensitizers, such as semiconductors, have been combined with H_2ase to create photocatalytic systems that aren't limited by the stability issues of biological photosensitizers. The first attempts were based on Cd–based photosensitizers.

In 2010 Brown et al. constructed a colloidal nanocrystal CdTe – [FeFe] – H_2ase system via self-assembly mediated by electrostatic interactions. This hybrid achieved, with ascorbic acid as electron donor, a STH of 1.8% in white light and STH of 9% in monochromatic light. The system was irradiated up to 50 min. High intramolecular electron transfer efficiency is achieved by the correct orientation of the H_2ase and H_2ase monolayers. The highest TONs were achieved for complexes that formed under lower H_2ase ratios, hereby the orientation within the complex the capping ligand 3-mercaptopropionic acid (MPA) on the nc-CdTe. This leads to a compatible surface charge with H_2ase and allows docking close to the surface localized distal [4Fe-4S] H_2ase cluster. [32]

To improve upon this experiment, Brown et al. constructed a molecular complex with MPA capped CdS – nanorods and *Clostridium acetobutylicum* [FeFe] – H_2ase. This allows for greater photostability, larger absorption cross-section and surface area. The MPA-capping ligand enabled controlled self-assembly and site-specific binding to a positively charged patch on H_2ase surface, promoting effective electron transfer via iron sulfur cluster. The highest TOF was achieved with a 1:1 CdS:H_2ase molar ratio. Long-term stability was affected by the photodegradation of MPA-CdS, due to oxidative loss of MPA from the CdS surface and photodegradation of the light-capturing components. [102]

Wilker et al. studied with a similar MPA capped CdS – nanorods – H_2ase, the electron transfer kinetics involved H2 production with ascorbic acid as electron donor. They found that the electron transfer constant from CdS to the H_2ase are comparable to the electron relaxation rate in the CdS - nanorods at 10^{-7} s^{-1}. This results in a QE of 42% for CdS NR:H_2ase mole ratio of 1:1. They suggested higher QE for ET, could be reached by improving the structure of the complex. For instance, by shortening the length of surface capping ligands, improving the nanorods for longer excited state lifetimes and using the molar ratio of H_2ase to CdS. [104]

In an effort to develop a system that doesn't rely on expensive (Ru-dyes), toxic (Cd-based quantum dot), and/or fragile (organic dyes) light absorbers, Caputo et al. developed a suspended amorphous polymeric carbon nitride (also often referred to as melon or g-C_3N_4) CN_x-[NiFeSe] H_2ase, redox mediator free system, with EDTA as electron donor capable of assisted water splitting. The assembly of the photosynthetic complex occurs via adsorption and leads to direct electron transfer (DET). However, the addition of MV^{2+} as redox mediator increases H_2 generation significantly, suggesting not yet fully optimized DET. A centrifugation test with the goal of gaining insight into the strength of interaction between CN_x and H_2ase showed only 12% remaining activity, indicating that the relatively weak interaction between CN_x and H_2ase, still allows for electron transfer to occur from CN_x to the H_2ase. This setup kept a reasonable amount of activity after 50h. In addition, a similar synthetic system with CN_x-NiP (Ni-based, water-soluble H_2ase mimic) has been tested. At the same concentrations, H_2ase system greatly outperforms the NiP – cocatalyst system. The H_2ase – CN_x was photoactive for 48h and operated 69h with as CN_x – MV - H_2ase system and is therefore limited by the electron transfer. In contrary to the NiP system where H_2 generation is dependent on the NiP concentration. [80]

Caputo optimized this system in a follow-up experiment with a CN_x – TiO_2 – [NiFeSe]-H_2ase photocatalyst. This photocatalyst improved solar light harvesting performance because TiO_2 utilizes the UV spectrum and the CN_x-TiO_2 allows for 3 different electron transfer pathways at 390 nm, 428 nm and 540nm utilizing a broad range of the visible light spectrum. Also, the titaniaphilicity of [NiFeSe]-H_2ase leads to a more stable binding and improved electron flow to the active site of the

H_2ase. A 1:10 enzyme particle ratio allows the H_2ase to function at the maximum rate because this directs the maximum electron flux of conduction band electrons. Adding an MV^{2+} redox mediator improved the H_2 production rate significantly, indicating that the system is limited by charge transfer. By comparing the ratio of H_2 produced with and without MV^{2+}, indicating the relative efficiency of charge transfer from the CN_x-H_2ase and CN_x-TiO_2-H_2ase, strong improvements in the charge transfer to the H_2ase could be shown. However, this shows that the interfacial electron transfer from CNx-TiO_2 to H_2ase is not fully optimized and indicates that the orientation of the bound H_2ase is not fully directed. The CN_x-TiO_2-H_2ase assembly achieved a TON of >5.8*10^5 after 72 h and a TOF of 8 s^{-1} without an external soluble redox mediator, assisted by EDTA. [105]

Hutton et al. developed a carbon dots (CD) – [NiFeSe]-H_2ase photocatalytic system for EDTA-assisted H_2 production. Carbon dots are attractive nanosized photosensitizers as they are low-cost, water-soluble, photostable, nontoxic, have easily modifiable surface chemistry and are highly stable. Positively charged ammonium-terminated CDs (Cd-$NHMe_2^+$) and negatively charged carboxylate terminated CDs (CD-CO_2^-) have been investigated. Due to favorable interfacial interactions, cationic CDs are capable of efficient transfer of photoelectrodes to negatively charged proteins. Cutting the light intensity, showed a linear decrease in TOF, indicating a limitation by light intensity. Investigation of the CD-H_2ase interface showed the efficiency of the DET. In the presence of the redox mediator MV^{2+} a 6-fold increase in H_2 production has been shown. This indicates a not yet fully optimized CD-H_2ase interaction but an improvement to the experiments of Caputo et al.. [105] The redox-mediated CD-$NHMe^{2+}$ - MV^{2+} - [NiFeSe] system reached a TOF_{H2ase} = 24 ± 7 * 10^3 mol H_2 (mol H_2ase)$^{-1}$ h^{-1} sustaining enzyme driven catalysis for up to 3 days. The loss of photocatalytic activity is rather due to degradation of H_2ase than of the CD. [106]

Some metal sulfides offer a band gap in the range of visible light and their conduction band energy level is above that required for water splitting. An alternative to CdS is In_2S_3, it has a similar band gap energy of 2-2.3 eV, CB potential of -0.8V vs RHE (reversible H_2 electrode) and lower toxicity. Compared to TiO_2, capable of only utilizing UV light, the main advantage is the absorption of visible light. The most critical step for photocatalytic H_2 production is the electron transfer between the conduction band of the semiconductor and the co-catalysts to reduce charge recombination in the semiconductor. This becomes especially apparent with H_2ase when the interfacial electron transfer at the semiconductor's surface is the rate-limiting step. Hutton et al. constructed a semi-biological hybrid photocatalyst constructed of porous In_2S_3 particles and adsorbed [NiFeSe] – H_2ase. Fast interfacial electron exchange between the semiconductor and H_2ase is usually achieved by oriented immobilization of the enzyme modulated by electrostatic interactions between charged groups and the photosensitizers surface and the net dipolar moment of the enzyme, guaranteeing that the distal 4Fe4S cluster is facing the photosensitizer surface. However, this is not the case in this system. The negative charge of In_2S_3 surface should not allow for proper orientation of immobilized H_2ase since the 4Fe4S cluster is surrounded by negative charges at neutral pH. Here the enzyme is immobilized within the porous structure. With a pore size slightly larger than the H_2ase, the chance of having the distal 4Fe4S cluster in sufficient distance to the photosensitizer wall for fast direct electron transfer preventing recombination of the electron-hole pair increases. The In_2S_3/H_2ase electron transfer was the rate-limiting step. The system achieved with sodium sulfite as electron donor, steady state rates of 292 µmol of H_2 (mg of H_2ase)$^{-1}$ min^{-1} and TOF_{H2ase} 986 s^{-1} during a maximum irradiation time of 9 min. [107]

Nam et al. achieved bias-free water splitting in photo electrochemical cell with a Si photocathode with [NiFeSe]- H_2ase wired to an inverse opal TiO_2 interlayer in connection with either an $BiVO_4$ or an PS2 photoanode. The system operated for 5 hours. [108]

The first CDs-[FeFe] (CrHydA1) H_2ase system capable of H_2 evolution with a redox mediator was developed in 2020. Negatively charged aspartic acid – AspCDs – Carbon dots self-assembled with a positive charged patch near the active site of the CrHydA1 H_2ase. CDs are smaller than H_2ase. Therefore several CD might attach to a single H_2ase molecule, however the CDs closest to the active site of the H_2ase will dominate the electron transfer to the enzyme. Differently charged electron donors, TEOA / MV^{2+} and EDTA influence the performance and the stability of the photosynthetic biohybrid complex. For instance, the positively charged TEOA leads to better photocatalytic performance and a better charge transfer rate because it allows the biohybrid complex to retain the interaction between the negatively charged AspCDs and the positive charged binding site on the H_2ase. The rate-limiting step is still the electron transfer. Even though the biohybrid assembly was capable of H_2 production without redox mediator, the presence of MV^{2+} improved stability and extended the operating lifetime to one week. The system reached an EQE of 1.7%. [109]

H_2ase 1 (Hyd-1) from *E.coli* is not capable of H^+ reduction at neutral pH but has excellent H_2 – oxidizing activities, is O_2 tolerant and even functions in air. Zhang et al. site selectively attached silver nanocluster (AgNC) onto the Hyd-1 H_2ase, providing an additional redox site capturing externally supplied electrons with sufficiently high energy to drive H_2 production. Excited by visible light, the AgNC acts in its photoexcited state as a powerful reductant. Implemented into a colloidal system with a graphitic carbon nitride g-C_3N_4 a TiO_2 together with the AgNC-Hyd-1 enzyme hybrid achieved TOF_{H2ase} of 40 H_2 s^{-1} with TEOA as electron donor while sustaining 20% activity in air. [110]

semiconductor + enzyme hybrids 1/3								
Photo sensitizer	***Biotic Abiotic Interface***	***Catalytic Center***	***Educt/ Product***	***Performance***	***Lifetime***	***SYSTEM***	***YEAR***	***REF.***
nc-CdTe (nano-crystal)	molecular complexes	*Clostridium acetobutylicum* [FeFe]-H_2ase	Ascorbic acid|H_2	**AWS** white light: **STH 1.8%** monochromatic light: **STH 9%** TON: 25 mol H_2 mol^{-1} H_2ase s^{-1}	irradiation up to 50 min	***TRL 3*** suspension	2010	[32]
CdS nanorod-MPA capped	CdS Nanorod MPA capped – [FeFe] H_2ase Complexes	*Clostridium acetobutylicum* [FeFe] H_2ase (=CaI)	aqueous ascorbic acid solution|H_2	**AWS** Quantum Yield for H_2 at 405nm: 20.4 ± 1.9%, TOF at 405nm: 380 mol H_2 (mol H_2ase)$^{-1}$ s^{-1}, TOF at high intensity light (30 000 µEm^{-2} s^{-1}) 983 mol H_2 (mol H_2ase)$^{-1}$ s^{-1}	operational for 4 h	***TRL 3*** suspension	2012	[102]
CdS nanorod	CdS Nanorod MPA capped – [FeFe] H_2ase Complexes	*Clostridium acetobutylicum* [FeFe] H_2ase (=CaI) expressed by *E.Coli*	aqueous ascorbic acid solution|H_2	**AWS** Electron Transfer Yield of 42% - purely kinetic Investigation of previous system of Wilker et. Al..	irradiation time 10min	***TRL 3*** suspension	2014	[104]
CNx	physical adsorption (DET), control experiment with CNx|(MV)|H_2ase,	*Desulfomicrobium baculatum* [NiFeSe]-H_2ase and NiP - H_2ase mimic	aqueous sacrificial electron donor solution (EDTA)|H_2	**AWS** $TON_{CnxH2ase}$: 50000 mol H_2 (mol H_2ase)$^{-1}$ TON_{CNxNiP} : 155 mol H_2 (mol NiP)$^{-1}$ TOF_{H2ase} : (5532 ± 553) mol H_2 (mol H_2ase)$^{-1}$ h^{-1} TOF_{CNx}:(55.3 ± 5.5)µmol H2 (g CNx)$^{-1}$ h^{-1}	photoactive up to 48h up to 69h with redox mediator, CN_x-NiP photoactive for 3h	***TRL 3*** suspension	2014	[80]

CNx/TiO_2	(CNx and/or TiO_2)-[NiFeSe]-H_2ase physical adsorption (DET) (optimized system with MV redox mediator	*Desulfomicrobium baculatum* [NiFeSe]-H_2ase	aqueous sacrificial electron donor solution (EDTA)|H_2	**AWS** TON: 5.8* 10^5 mol H_2 (mol H_2ase)$^{-1}$ after 72h at λ > 420 nm initial TOF_{H2ase}: 6353 ± 635 h^{-1} $TOF_{CNx\text{-}TiO2\text{-}H2ase}$=8$s^{-1}$ EQE (external quantum efficiency): 4.8% UV irradiation 0.51% visible light	runtime 72h	***TRL 3*** suspension	2015	[105]
Carbon Dots (CDs) CD-$NHMe_2^+$ and CD-CO_2^-	CD-$NHMe_2^+$/CD-CO_2^-|(MV)|[NiFeSe]H_2ase/FccA	*Desulfomicrobium baculatum* [NiFeSe]-H_2ase further experiments for reduction of fumarate to succinate with: *shewanella oneidensis* MR-1FccA (Fumarate reductase)	aqueous solution with EDTA |H_2	**AWS** TON_{H2ase} 43.000 mol H_2 (mol H_2ase)$^{-1}$ after 24h $TOF_{H2ase[CD\text{-}NHMe2+]}$=3.9±0.9 * 10^3 mol H_2 (mol H_2ase)$^{-1}$ h^{-1} with MV^{2+} redox mediator $TOF_{H2ase[CD\text{-}NHMe2+]}$ =24 ± 7 * 10^3 mol H_2 (mol H_2ase)$^{-1}$ h^{-1} TOF_{FccA}: 6.0 ± 0.6 × 10^3 mol succinate (mol FccA)$^{-1}$ after 24h EQE of 0.36 ± 0.02% @ 365nm	Runtime 48h stable CD-H_2ase reaction up to 72h	***TRL 3*** suspension	2016	[106]
In_2S_3	interfacial electron transfer	*[NiFeSe] H_2ase - Desulfovibrio vulgaris Hildenborough*	aqueous sodium sulfite solution (10 mL of 50 mM Tris-HCl pH 7.0)/ H_2	**AWS** TOF_{H2ase}=986s^{-1} initial rates: With sulfite: 1140 ± 45 µmol of H_2 (mg of H_2ase^{-1} min^{-1}. without sulfite 3763 ± 221 µmol of H_2 (mg of H_2ase^{-1} min^{-1}) steady state rates: 292 µmol of H_2 (mg of H_2ase)$^{-1}$ min^{-1}	irradiation time: up to 9 minutes	***TRL 3*** *suspension*	2016	[107]
$BiVO_4$	$BiVO_4$|FTO||p-Si|IO-TiO_2	*Si|IO-TiO_2|[NiFeSe]H_2ase*	Water/H2	**OWS** Faradaic efficiency of (98 ± 14)%	Irradiation time: 5 h	***TRL 3*** *PEC*	2018	[108]

aspartic acid-based carbon dots (AspCDs)	molecular complexes, self-assembly, w/o MV^{2+} redox mediator	*[FeFe] H_2ase (CrHydA1) Chlamydomonas reinhardtii*	aqueous sacrificial donor solution [(0.5 mg mL^{-1} AspCDs, 0.1 M EDTA pH 7 or 10% TEOA pH 7)] + (0.1 mmol of methyl viologen (5 mM solution) / H_2	**AWS** EQE: 1.7% @ 420nm initial activity: 1.73 µmol(H_2) mg^{-1} (H_2ase) min^{-1}	stability of biohybrid assembly in presence of redox mediator beyond 1 week continuous H_2 production: - 8h without MV^{2+} - up to 48h in TEOA with MV^{2+}	***TRL 3*** *suspension*	2020	[109]
g-C_3N_4 /TiO_2	covalently attached close to existing distal and medial FeS clusters colloidal system implement-ed into hetero-structure with TiO_2 and graphic carbon nitride (g-C_3N_4) AgNC - connected by soft polymeric material PMAA (poly-methyl acrylate)	AgNC Ag-Nanocluster - [NiFe]-H_2ase - (Hyd -1) *E.coli Biohybrids*	Aqueous buffer solution (TEOA) / H_2	**AWS** 40 molecules H_2 s^{-1} per active site EQY @ 500nm: 2.3%	Irradiation time: 4h	***TRL 3*** *suspension*	2020	[110]

Tab. 9 Semiconductor + Enzyme hybrids SAPSs

3.7.7. Bio photosensitizers – Enzymes SAPS

With the aim of combining the advantages of natural photosensitizers, such as high quantum yield and H_2ases with their high turnover rates, selectivity and low overpotential in an artificially constructed system, made of readily available materials and with low environmental impact, bio photosensitizers – enzyme SAPSs have been developed. At first, researchers focused on connecting PS1 to H_2ase. Direct coupling of PS1 and H_2ase requires O_2-tolerant H_2ase. This complex consisting of photosystem I and H_2ase was connected on a solid gold surface to construct a cathodic photochemical half-cell.

Krassen et al. developed a monolayer PS1 – membrane bound [NiFe]-H_2ase (MBH) complex attached to a gold electrode via a histidine/Ni-NTA interaction. This allowed for site-specific oriented attachment. Even though, a physical connection between the complex and the Au – electrode was established, electrons provided by the gold electrode were transferred to PS1 via a soluble electron carrier N-methylphenazonium methyl sulfate (PMS). The complex reached H_2 production rates of up to 4500 ± 1125 mol H_2 min^{-1} mol^{-1} hybrid complex at 20°C, pH 7.5 and -90mV of bias. In order to improve the performance, they suggest an H_2ase – PS1 synthesized *in vivo*, to produce a system that produces H_2 directly from water and sunlight.[111]

Lubner et al. developed a technology to connect PS1 via a molecular wire to catalytic centers such as Pt, [FeFe]- and [NiFe] – H_2ase. The molecular wire can covalently connect the F_B iron-sulfur cluster of PS1 to either a Pt nanoparticle or the distal iron – sulfur cluster of H_2ase via surface-located cysteine residues that act as ligands to Fe-S clusters. Through site-specific mutagenesis they are changed into glycine residues. The molecular wire forms a direct chemical bond to the iron – sulfur clusters by sulfhydryl groups at the end of the wire. This allows electrons to tunnel quantum mechanically between the two modules without rate and yield restrictions of diffusion-limited processes. With electrons supplied by a sacrificial donor, this photochemical cathode is capable of H_2 production. An investigation into the influence of the molecular wire, by comparison of different dithiol linkers, showed that very short wires resulted in low rates of light-induced H_2 generation because of either because of inefficient coupling or the inability to shield the protein from denaturation by the metal surface of the Pt -nanoparticle. An aliphatic dithiol wire with more than 6 carbon atoms resulted in lower rates. The best rates were achieved by aromatic dithiol molecular wires. The PS1 - molecular wire – Pt nanoparticle construct outperformed the PS1- molecular wire – H_2ase with 312 µmol of H_2 (mg of Chl)$^{-1}$ h^{-1} to 3.9 µmol of H_2 (mg of Chl)$^{-1}$ h^{-1}. The system is limited by the charge transfer.[79]

Lubner et al. improved on this setup in a follow-up experiment trying to attain electron throughput by oxygenic photosynthesis. By constructing a cross-linked Cyt c_6–PS1–[FeFe] H_2ase nano construct using a 1,8-octanedithiol molecular wire in a medium of Na-phosphate buffer and Na- ascorbate as electron donor, at pH 6.5 they achieved a light induced H_2 of 2200 ± 460 µmol mg Chl^{-1} h^{-1} continuously over 4h. The initial H_2 evolution rate was resumed after the addition of fresh ascorbate. Full recovery of H_2 evolving ability after 100 days of storage under anoxic conditions at room temperature was observed. The electron transfer throughput of the nano construct surpassed that of oxygenic photosynthesis. [112]

Since earlier PS1-molecular wire – H_2ase systems did not incorporate a spectroscopic reporter that can show the electron transfer between the two systems. The next iteration of Lubners concept was PS1 – molecular wire – organic cofactor (1-(3-thiopropyl)-10(methyl)-4,40-bipyridinium chloride). Under illumination, the reduction of the organic cofactor is comparable to the rate of H_2 evolution of a PS1 – molecular wire – H_2ase system. [113]

A different approach to tether a PS 1 to H_2ase with the help of 2 different redox polymers was developed by Tapia et al.. The PS1 was wired to an Os-PVI loaded polyvinyl imidazole redox polymer,

with positive potential, while the H_2ase was wired to baltocene-functionalized branched polyethyleneimine (Cc-BPE) with negative potential to protect the H_2ase from O_2 inactivation. At 400 mW cm^{-2} the photocurrent dropped within 10 minutes to 0 and at 40 mW cm^{-2} PS1 lost 50% of its activity within 10min. The system achieved a TOF = 3 s^{-1}. [88]

Mersch et al. developed a PS2 based PEC system by immobilizing PS2 on an IO-mesoITO anode and coupling it with an IO-mesoITO [NiFeSe]-H_2ase Photocathode. With an applied bias of 0.8 V a STH efficiency of 5.4±0.3%. [33]

Unassisted solar water splitting with H_2ase *in vitro* has been a long-standing goal. Nam et al. mimicked the natural Z-scheme in a PEC setup with a proton reducing Si|IO-TiO_2|[NiFeSe]-H_2ase photocathode and a PS2 photoanode. Producing 70 ± 0.13 µmol H_2 /cm^2 at a Faradaic efficiency of(91 ± 19)% with an applied bias of 0.4 V over 3 h. [108]

Sokol mimicked a bias-free water splitting system with PS2 on a dye sensitized photoanode wired to H_2ase. Therefore, a PS2|dpp - sensitized|IO-TiO_2 photoanode with an Os-complex redox polymer for effective electronic communication, avoiding possible limitations from inefficient interfacial electron transfer. As cathode, an IO-ITO|[NiFeSe]-H_2ase was used. As PS2 is a blue and red-light absorber, DPP – dye is a complementary absorber in the green spectrum. At overall water-splitting with 0V bias, the initial photocurrent decayed from 130 to 5 µA cm^{-2} after 1 h irradiation, leading to an average half-life time of 6.5 min, which is consistent with the stability of PS2 in vivo ($\tau_{1/2}$~20 min). With a bias of 0.3 V an STH 0.14 ± 0.02 % .[114] A similar setup with format deH_2ase was used for light-driven CO_2 fixation to formate [115].

Bio-photosensitizer + Enzymes								
Photosensitizer	***Biotic Abiotic Interface***	***Catalytic Center***	***Educt/Product***	***Performance***	***Lifetime***	***SYSTEM***	***YEAR***	***REF.***
PS1	immobilized on gold electrode, soluble electron carrier N-methylphenazonium methyl sulfate (PMS)	[NiFe]-H_2ase (MBH) from *Ralstonia eutropha H16*	Aqueous HEPES buffer | H_2	**AWS** 4500 ± 1125 mol H_2 min^{-1} mol^{-1} hybrid complex (at pH 7.5, 20 °C, at bias of 90 mV).	runtime of experiment: 30 min The photocurrent of the monolayer decreased by about 50% during 30 min of illumination	***TRL 3*** PEC- half cell	2009	[111]
PS1	on gold electrode, molecular wire connecting [4Fe-4S] cluster of PS1 with catalyst	Pt or [FeFe]- H_2ase	3 soluble electron donors: Cyt c6, ascorbate, DPIP |H_2	**AWS** H_2ase: 3.9 µmol H_2 $(mg\ Chl)^{-1}$ h^{-1} Pt: 312 µmol of H_2 $(mg\ of\ Chl)^{-1}$ h^{-1}	construct stable for 2 months at room temperature in anoxic conditions	***TRL 3*** PEC- half cell	2010	[113]
CytC6 crosslinked PS1	Octanedithiol molecular wire	[FeFe]-H_2ase	sodium phosphate buffer, sodium - ascorbate electron donor||PS crosslinked with molecular wire to H_2ase	**AWS** 2201 ± 460 µmol mg Chl^{-1} h^{-1}	irradiation 4h full recovery of H_2 evolution after 100d being stored at room temperature in anoxic conditions	***TRL 3*** suspension	2011	[112]

PS2	PS2|IO-mesoITO||IO-mesoITO|H_2ase	[NiFeSe]-H_2ase	Water/H_2	**AWS** **5.4±0.3 STH** I=0.25mW/cm^2 at U=0.28V	no information	***TRL 3*** PEC	2015	[33]
PS1	Os-PVI/PSI/Cc-BPEI or MV-LPEI /Hase	[NiFe]-H_2ase Desulfovibrio gigas	MV|H_2	**AWS** TOF = 3 s^{-1}	photo current fell within 10 minutes to 0, under 40mW/cm^{-2} irradiation PSI retained 50% of its activity after 10 min of continuous exposure	***TRL 3*** PEC	2017	[88]
PS2	PS2|IO-mesoITO|Si||IO-TiO2 |H_2ase PEC Setup	p-Si|[NiFeSe]-H_2ase	Water/H_2	**AWS** Faradaic efficiency of (91 ± 19) %	Irradiation 3 h	***TRL 3*** PEC	2018	[108]
PS2/dpp	FTO|POs-PS2|dye(dpp)|IO-TiO2||IO-ITO|H_2ase POs (redox polymer poly (1-vinylimidazole-co-allylamine)-Os(bipy)2Cl) FTO (fluorine tin oxide)	[NiFeSe]-H_2ase	Water|H_2	**OWS** STH 0.14±0.02% η_F=88±12%	irradiation of 1h - photocurrent decayed by 90% $\tau_{1/2}$ = 8min	***TRL 3*** PEC	2018	[114]

Tab. 10 Bio - Photosensitizer + Enzymes SAPSs

3.7.8. Photosensitizers – Biomimetic complexes

One could make the argument that photosensitizer - H_2ase mimics systems can also be classified as SAPS, as some mimics are based on heavily modified H_2ase. The development of H_2ase mimics is driven by the desire to copy the extremely high activity and selectivity while also improving the stability of H_2ase by mimicking the active site of H_2ase, not only structurally but also functionally. A MPA - CdTe (CdTe stabilized by 3-mercaptopropionic acid) – [FeFe] -H_2ase mimic system was developed achieving a TOF of 50 h^{-1} and staying active for 10 h with ascorbic acid as sacrificial agent showing a tenfold increase of lifetime compared to [FeFe] - H_2ase. The [FeFe]-H_2ase mimic was modified by incorporating a cyanide (CN) group to anchor three hydrophilic ether chains to the active site to increase the water solubility of the system. [116] Even better performance has been achieved with ZnS - ([(μ-SPh-$_4$-NH_2)$_2$$Fe_2$$(CO)_6$] with an initial TOF of 100 h^{-1} and stable activity for 38 h [117].

Photosensitizer + biomimetic complex								
Photosensitizer	***Biotic Abiotic Interface***	***Catalytic Center***	***Educt/Product***	***Performance***	***Lifetime***	***SYSTEM***	***YEAR***	***REF.***
MPA - CdTe (CdTe stabilized by 3-mercaptopropionic acid)	Ascorbic Acid (proton donor and sacrificial agent)	artificial water-soluble [FeFe]-H_2ase mimic	Water + ascorbic acid / H_2	**AWS** TON = 505 TOF = 50 h^{-1}	active up to 10 h	***TRL 3*** suspension	2011	[116]
ZnS - nanoparticles	physical adsorption of ZnS and Fe_2S_2	H_2ase mimic ([(m-SPh-4-NH_2)$_2$$Fe_2$$(CO)_6$]; referred to hereafter as [Fe_2S_2])	water + ascorbic acid / H_2	**AWS** TON = 2607 initial TOF = 100h^{-1} QE: 2.5% @325nm	stable activity during 38h of irradiation	***TRL 3*** suspension	2012	[117]

Tab. 11 Photosensitizer + biomimetic complex SAPSs

3.7.9. Cell based H_2- producing SAPSs

Compared to enzyme-based systems, cell-based SAPSs offer several advantages. Living Cells act as catalytic centers without any time-consuming and costly manipulations like enzyme purifications and could also employ intracellular repair mechanisms regarding photodamage improving the lifetime of the system. Furthermore, the self-replicating nature of biological organisms and the low cost of whole-cell catalysts are advantages. Via genetic engineering, cells are optimized to the individual use case by expressing the desired enzyme. Often semiconductors are employed as photosensitizers because of their broad absorption range.

The first system to employ a recombinant improved *E.coli* expressing [FeFe]-H_2ase and relevant maturase from *Clostridium acetobutylicum* as biocatalyst, because [FeFe]-H_2ase shows high turnover rates. Suspended TiO_2 particles acted as photosensitizers and MV^{2+} as redox mediator, ascorbic acid as sacrificial agent. The system was irradiated for 15h and continuously produced H_2, significantly longer than the control experiment with purified HydA-H_2ase that became inactive within 4h showing the improved stability of the cell-based system. The AQY of 0.31% is lower than the control experiment with purified HydA – H_2ase. The electron transfer step from the reduced MV extracellularly added to intracellular HydA might be the rate limiting step. [118]

The photosensitizer can also be directly attached to the cell. Bo Wang et al. precipitated CdS – nanoparticles on the surface of *E.coli*. Anaerobically induced, endogenous [NiFe] – H_2ase generated H_2 with an AQE of 9.59% @ 620nm. [119]

E.coli can also be sensitized by $AgInS_2/In_2S_3$. The $AgInS_2/In_2S_3$.- endogenous [NiFe] – H_2ase achieved H_2 production with 3.3% QE at 720nm. $AgInS_2/In_2S_3$ is an excellent light absorber and offers faster electrical conduction than In_2S_3. At first In_2S_3 crystals were grown on the cell surface then the $AgInS_2$ then anchored on the surface of In_2S_3. [120]

Organic electron mediators also have been used with cell-based SAPS. Reduced graphene oxide (RGO) with integrated Cu_2O and *shewanella oneidensis MR-1* has been constructed improving catalytic H_2 production 11-38-fold compared to other charge transfer systems. With ascorbic acid as sacrificial agent the system was irradiated and active for 4h. [83]

Organic dyes also have been used for the sensitization of cell-based SAPS. Whole cells of *Rhodopseudomonas* were added to a slurry of Rhodamine B - dye sensitized TiO_2 and MV^{2+} mediated systems to produce H_2. [121]

Cell Based SAPSs - H_2 Production								
Organic Dye - cells SAPSs								
Photosensitizer	Biotic Abiotic Interface	Catalytic Center	Educt/Product	Performance	Lifetime	SYSTEM	YEAR	REF.
RhB (Rhodamine B) - TiO_2	Tris-HCl-MV^{2+}	*R.capsulata*	H+/H_2	QY=12%	runtime 1h	***TRL 3*** suspension	1999	[121]
Semiconductor - cells SAPS								
Photosensitizer	Biotic Abiotic Interface	Catalytic Center	Educt/Product	Performance	Lifetime	SYSTEM	YEAR	REF.
TiO_2 - suspended nanoparticles	MV^{2+}	*E.coli* - recombinant expressing thegenes encoding the [FeFe]-H2ase and relevant maturases from *Clostridium acetobutylicum*	Ascorbic acid / H_2	**AWS** TiO_2/MV^{2+}/E.coli for 5 h: 117 µmol(H_2) for 5h - for the Enzyme based system: $TON_{TiO2/MV2+/HydA}$: 222 000 mol H_2 / mol HydA $QY_{TiO2/MV2+/HydA}$ @ 300nm : 1,57% $TON_{TiO2/HydA}$: 231 000 mol H_2 / mol HydA	5h irradiation time up to 15h examination period	***TRL 3*** suspension	2016	[118]
CdS - nanoparticle	without mediator photosensitizer directly precipitated on cell	*E.coli* endogenous bacterial [NiFe]-H2ase	MOPS or Wastewater (Glucose) / H_2	**AWS** QE: 7.98% at 470nm 9.59% at 620nm	over 3 h exhibited a decreasing trend with increasing light intensity when the light intensity was higher than 2000 W m^{-2}	***TRL 3*** suspension	2017	[119]
$AgInS_2/In_2S_3$ - Heterojunction	without mediator - direct electron transfer between photosensitizer and cell	*E.coli* endogenous bacterial [NiFe]-H2ase	Glucose + Water / H_2	**AWS** QE: 3.3% at 720 nm	runtime up to 3h	***TRL3*** suspension, Nanoparticles on surface of E.coli,	2018	[120]
Cu_2O	reduced graphene oxide (RGO)	*Shewanella oneidensis* MR-1	Ascorbic Acid + Water / H_2	no information	runtime up to 4h	***TRL3*** suspension	2020	[83]

Tab. 12 Cell Based SAPSs

3.8. Conclusion literature study into SAPSs

Comparing the listed SAPSs has been a challenge. Not all studies provide the same performance parameters, only a few also provide STH efficiency. Input parameters such as spectrum, light intensity, environmental parameters can vary. Unassisted, bias-free pure water splitting at neutral conditions in visible light is not possible with most systems. None of the listed SAPSs has exceeded the TRL 3. The longest operating times have been achieved with semiconductor enzyme hybrids with up to 72 h [105], [106]. The highest visible light STH of 5.4% has been achieved by Mersch et al. with a PS2

based PEC system by immobilizing PS2 on a IO-mesoITO anode and coupling it with a IO-mesoITO [NiFeSe]-H_2ase photocathode with an applied bias of 0.8V [33]. Most systems are limited by electron transfer. Thylakoid-based systems face quick photodegradation. None of the papers mention any strategies for scale-up. Liposome-based SAPSs have been constructed [77]. This leaves room for improvement.

4. PhotoSomes – liposome based SAPSs

In 2021 Pannwitz et al. proposed to mimic nature and embed natural photocatalysts in artificial lipids [1] similar to the lipid layers of thylakoid membranes for photocatalytic green H_2 production. A biobased photocatalyst must be stable against conditions such as low pH, high temperatures and oxidation since these conditions arise during photocatalytic H_2 production however, currently available phospholipids, a key component of cell membranes, aren't [122]. To create a highly efficient bio-based H_2 production system, archaeal tetrahedral lipids (TEL) could be embedded with a photocatalysts, for instance thylakoid membrane fragments, to provide electrons, a charge carrier such as quinones and a H_2ase, an enzyme to catalyze water splitting to form a stable photoactive liposome, a so-called "PhotoSome", capable of photocatalytic water splitting. PhotoSomes would operate as suspended particulate catalysts in solar collectors, filled with an aqueous medium producing an oxyH_2 gas mixture. Because of the limited long-term stability of biobased photocatalyst, suspended particulate catalysts offer an advantage compared to catalysts immobilized on electrodes, as they can easily be replenished. To renew the catalysts, the system only needs to be flushed and new PhotoSomes injected. Regarding the handling of the catalyst, this is easier to accomplish and automate at a large scale compared to exchanging inactive photoelectrodes. In the production of the PhotoSomes, no rare earth - and only small quantities of transition metals mainly from biological sources are used, allowing for simple disposal of inactive PhotoSomes and low overall environmental impact.

4.1. The Photo- (Lipo)some - PhotoSome

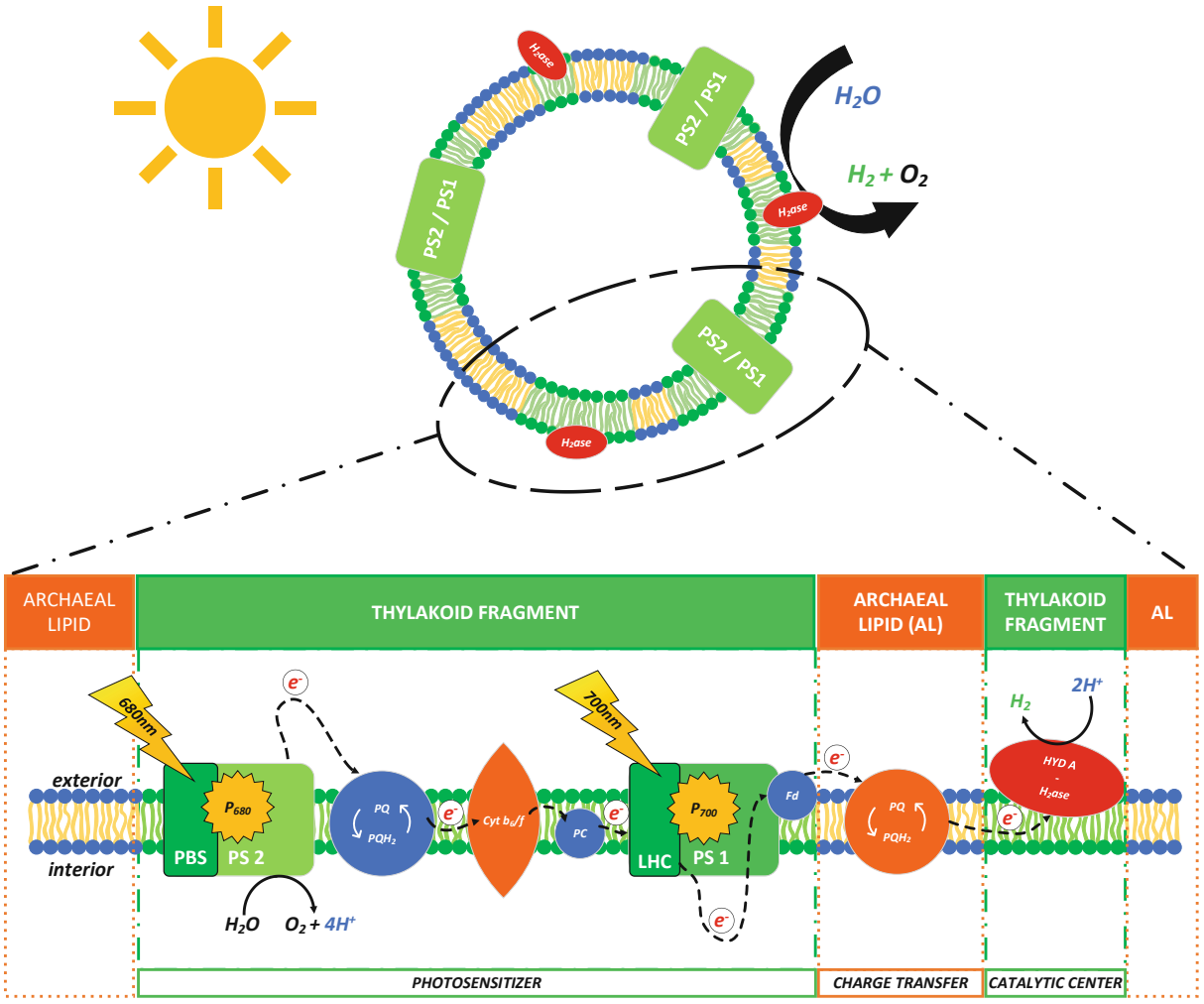

Fig. 12 Schematic view of PhotoSome with photocatalytic process

Liposomes are sphere-shaped vesicles with phospholipid bilayers that surrounding an inner aqueous compartment. They form by dispersing lipids in an aqueous media. Salts and other water-soluble compounds present during the formation of the liposomes are sealed into the aqueous compartment. Liposomes cannot trap hydrophobic compounds in the aqueous compartment but are able to integrate hydrophobic compounds, such as membrane proteins, into the bilipid layer. Liposomes are used as a tool in various scientific disciplines, including mathematics and theoretical physics, biophysics, chemistry, colloid science, biochemistry, and biology [123]. Using spherical membranes mimicking thylakoid membranes by forming photoactive liposomes offers opportunities to confine redox half-reactions, facilitate charge separation, and avoid cross-reactivity – the main challenges in photocatalytic systems [1]. Phospholipids, a key component of cell membranes, are molecules consisting of a hydrophilic head containing a phosphate group and two hydrophobic “tails”. Thanks to this amphiphilic characteristic, phospholipids can rearrange themselves in an aqueous solution either as a monolayer, a sphere-shaped micelle or bilipid liposomes. However, phospholipids have limited stability and should be kept for long-term stability at temperatures of 4-6°C and at pH 6.5 [122]. To overcome the limitations of the phospholipids, PhotoSomes are constructed with tetrahedral lipids (TELs) found in archaea native to extremely hostile environments such as volcanic ponds, from cultures such as *Sulfolobus* that developed to withstand these hostile conditions. For instance, the optimal condition for lipids of *Sulfolobus solfataricus* culture are 3-4.5 pH and 87 °C [124]. During the formulation of PhotoSomes, the randomly sized thylakoid fragments, some carrying

the photosynthetic complex consisting of PS2/PS1 and others carrying the H_2ase integrate themselves unoriented into the bilipid liposome to create PhotoSomes. Charge transfer between the fragments is ensured by a quinone pool native to the source organisms of the TEL and thylakoid membranes.

4.2. The Photosensitizers

To start a photocatalytic cycle, a photosensitizer (PS) is irradiated to form an electronically excited species PS*. This can act as a strong oxidant or reductant and either oxidize an electron donor or reduce an electron acceptor to form a reduced (PS^-) or oxidized (PS^+) species. These species then transfer their charge to a catalyst to drive a substrate oxidation or reduction. [1] The photosystem PS1 and PS2 are naturally occurring photosensitizers and are located on thylakoid membranes. The thylakoid membrane is a bilayer lipid membrane that separates the outside, the stroma, from the more acidic inner lumen side. It serves as an anchor point for the light-harvesting antennae, the two photoreaction centers photosystem 2 (PS 2) and photosystem 1(PS 1), cytochrome b_6/f and ATP-synthase. It serves as a channel for energy shuttled from the light-harvesting antenna photoreaction centers of PS2 and PS1. The Isolation of PS1 and PS2 from thylakoid membranes requires costly unit operations (UP) such as chromatography and gradient centrifugation and they are unstable in vitro [55], [125]. In contrast, the isolation of the thylakoid membrane with only stepwise sequential ultra-centrifugation thylakoid is quite simple. Thylakoid membranes were chosen as photosensitizers.

A significant advantage of a single photocatalytic system is a simple framework with the opportunity to avoid charge recombination and back reactions, the main challenge in photocatalytic artificial photosynthesis [1]. However, the separation of the oxidative from the reductive catalytic centers by compartmentalization of the different redox half-reactions with lumen and stroma is one of the critical features of thylakoid membranes minimizing charge recombination and chemical back reactions, which is detrimental for an efficient, sustained reaction [1]. By implementation of thylakoid fragments, this feature can be implemented with the added benefit of broader light absorption and higher redox potential of dual photosensitizer Z-scheme set-up. Photosynthetic organelles and thylakoid membranes possess many advantages over isolated reaction center complexes for electrochemical applications such as simpler immobilization procedures, multiple electron transfer routes and high protein stability [126]. Applying thylakoid membrane fragments as photosensitizers for biophotochemical electrodes has been done previously by Calkins et al. [126]. Adding randomly oriented, different-sized thylakoid membrane fragments into liposomes requires further consideration. First, the orientation of the fragment. The active site of the water oxidation complex with PS2 is naturally located on the inside, lumen, of the thylakoid membrane. Because of random orientation, this active site could be near a potential electron donor site of the charge transfer chain, increasing the recombination rate. Secondly mismatched ratio of PS2 to PS1. The natural Z-scheme suffers a bottleneck by different photosynthetic rates between PS1 and PS2 resulting in mismatched ratios of PS1- to PS2- rates. For instance, Synechococcus *sp. PCC 7002* grown to the end of the exponential phase, has a ratio of 1.8. On average, if N electrons are transferred through each PS2 per second, then each PS1 transfers N/1.8 electrons per second [112]. Randomly arranged thylakoid fragments could influence this ratio negatively. This is especially relevant for the determination of electron throughput by PS1 and PS2. Thirdly position of the fragments. As the catalytic center and photosensitizers move further apart, the charge transfer efficiency drops. Further the correct ratio of photosensitizer to H_2ase depending on the TOF of the components is crucial. While thylakoids of algae and plants are located in the chloroplast, as part of a complex membrane assembly with appressed grana stacks a more open stroma lamella, thylakoid membranes in cyanobacteria have no grana/stroma arrangement and are not confined into a subsection of the cell. Further differences are the light-harvesting antenna complexes, phycobilisomes by cyanobacteria and LHCs by plants and some minor peptide compositions [127]. There are further differences, begging the question of the

photocatalytic performance of different thylakoid membrane sources. Given the redox potential of PS1 and PS2 and unavoidable losses by artificial, imperfect electron transfer, only a system with additional photosensitizers or the entire photosynthetic complex on the thylakoid membrane provides sufficient potential for overall water splitting without SED at neutral conditions. The literature on the photocatalytic performance of thylakoid membranes is scarce. A review on thylakoid membrane–based photo bioelectrochemical systems has been written by Pankratov et al. [128] and there have been several papers on photobiological solar cell designs. The most feasible comparison is based on a per-protein photocurrent. Most papers only offer a photocurrent per cell size measurement. Spinach thylakoid membranes are studied the most, also offering the highest photocurrents. The thylakoid membranes for PhotoSomes are sourced from cyanobacteria (UTEX 2973 *Synechococcus elongatus*) grown on industrial waste stream substrates, capturing CO_2 during cultivation.

Performance of Thylakoid Membranes						
Organism	***Photocurrent***	***System***	***Input***	***Info***	***Year***	***Ref.***
Spinach thylakoids	80 nA per mg protein 430 nA per mg chlorophyll	thylakoid/catalase mixture on 1 cm^2 Toray® carbon paper electrodes	0.45 V vs. Ag|AgCl and illumination of 5200 lumen	Protein conc: 4,153mg/ml Chlorophyll conc. 0.839 mg/ml	2014	[129]
Beet greens	20 nA per mg protein 100 nA per mg chlorophyll	thylakoid/catalase mixture on 1 cm^2 Toray® carbon paper electrodes	0.45 V vs. Ag|AgCl l and illumination of 5200 lumen	Protein conc: 4.22mg/ml Chlorophyll conc. 0,997mg/ml	2014	[129]
Collard greens	9 nA per mg protein 30 nA per mg chlorophyll	thylakoid/catalase mixture on 1 cm^2 Toray® carbon paper electrodes	0.45 V vs. Ag|AgCl and illumination of 5200 lumen	Protein conc: 11.6 mg/ml Chlorophyll conc. 3.29 mg/ml	2014	[129]
Green chard	1.6 nA per mg protein 7 nA per mg chlorophyll	thylakoid/catalase mixture on 1 cm^2 Toray® carbon paper electrodes	0.45 V vs. Ag|AgCl and illumination of 5200 lumen	Protein conc: 10.2 mg/ml Chlorophyll conc. 2.37 mg/ml	2014	[129]
Kale	2.2 nA per mg protein 9 nA per mg chlorophyll	thylakoid/catalase mixture on 1 cm^2 Toray® carbon paper electrodes	0.45 V vs. Ag|AgCl and illumination of 5200 lumen	Protein conc: 9.09 mg/ml Chlorophyll conc. 0.839 mg/ml	2014	[129]
Arugula	1.6 nA per mg protein 11 nA per mg chlorophyll	thylakoid/catalase mixture on 1 cm^2 Toray® carbon paper electrodes	0.45 V vs. Ag|AgCl and illumination of 5200 lumen	Protein conc: 10.1 mg/ml Chlorophyll conc. 1.51 mg/ml	2014	[129]
Watercress	0.7 nA per mg protein 4 nA per mg chlorophyll	thylakoid/catalase mixture on 1 cm^2 Toray® carbon paper electrodes	0.45 V vs. Ag|AgCl and illumination of 5200 lumen	Protein conc: 10.9 mg/ml Chlorophyll conc. 1.81 mg/ml	2014	[129]
Spinach thylakoids (fresh/organic)	0.43 ± 0.02 µA/$cm^{2.}$	thylakoid/catalase mixture was physically adsorbed onto Toray® carbon paper electrode, dried and silica layer vapor deposed onto electrode	0.45 V vs. Ag/AgCl in 0.1 M pH 5.5 citrate buffer	bf_6 inhibited the photocurrent for PSI inhibited thylakoids is 11 ± 2% of intact thylakoids ATP Synthase inhibited - photocurrent decreases by 16% ATP Synthase uncoupled - photocurrent increase by 25%	2014	[130]
Spinach thylakoids (fresh/organic)	peak: 63µA/cm^2 steady: 38µA/cm^2	multiwalled carbon nanotubes using a molecular tethering [Au-MWNT-thylakoid]	25°C using 0.1 M tricine buffer of pH 7.8 as the electrolyte $[Fe(CN)_6]^{3-/4-}$ as a redox mediator	steady state photocurrent for up to one week	2013	[126]

Spinach thylakoids (fresh/organic)	100 µAcm^{-2}	multiwalled carbon nanotubes on porous electrode [Au-MWNT-thylakoid]	0.2 V vs. Ag|AgClsat and a light intensity of 1500 mmol m^{-2} s^{-1} mediator : 1,2-naphthoquinone	area densities Chl a in the thylakoid membrane and MWCNTs were 120 µµgcm^{-2}	2018	[131]
Spinacia oleracea	71 µAcm^{-2}	Quartz wafer	irradiation: 1000 W m^{-2} +0.22 V vs Ag|AgClsat mediators: monomeric ([Ru(NH3)6]3+) polymeric ([Os(2,2'-bipyridine)2-poly(N-vinylimidazole)10Cl]+/2+),	Chlorophyll content: 3.2 mg mL^{-1}	2018	[132]
Spinacia oleracea	5.24 ± 0.50 µAcm^{-2}	3D matrix of RGO with amidated surface for wiring thylakoids	mediator free system 6 V vs. standard H2 electrode (SHE), illumination intensity of 400 W m^{-2}	Unlike, what is observed with the thylakoids of Syn, electrons cannot be abstracted directly from plant PS2 and a mediator is required to obtain a photocurrent. Therefore, different strategies should be applied for using cyanobacterial or plant thylakoids for solar energy conversion.	2018	[133]
Synechocystis	14 µA/cm²	Graphite anode	unmediated external bias: 0.05V Ag/AgCl.		2015	[127]
Synechocystis K238 mutant	35 µA/cm²	graphite anode	unmediated external bias: 0.05V Ag/AgCl.		2015	[127]
Spinacia oleracea	62.5 µAcm^{-2}	wired to osmium redox polymers screen printed to carbon and gold electrodes or modified with either gold micro or nano particles.	illuminated with 400Wm^{-2}		2018	[134]

Tab. 13 Performance Thylakoid Membranes

4.3. The charge transfer

Quinones play a central role in photosynthesis. Plastoquinone PQ-9 is an electron carrier shuttling electrons from PS2 to bf6. The beauty of organic, redox-active quinones lies in low-cost, sustainable charge carriers with high redox reactivity and excellent electrochemical reversibility. Molecular structure engineering can easily modify their electrochemical properties [135]. Quinones are present in nearly all living organisms. PQ connects photosynthesis with metabolism and plays a role in photoprotection, helps to manage oxidative stress, and affects the mechanical properties of lipid membranes, changing permeability and increasing stability [136]. Grumbach studied the distribution of chlorophylls, carotenoids and quinones in radish and spinach cotyledon/chloroplasts and thylakoids [137]. The concentration of quinones in plants changes with exposure to light [136]. The Chl (a + b) to PQ ratio of plant chloroplasts is in the same range of cyanobacteria, despite the big differences between the light-harvesting complexes [138]. The exact electron transfer pathway, especially with redox-mediated systems like PhotoSomes is challenging to determine at this point. Calkins et al. described 4 different electron pathways with their immobilized thylakoids, redox-mediated, membranes [126] since electrons can be extracted at several points along the linear electron transport chain via three electron mediators including the two quinone acceptors, Q_A and Q_B, toward the cyt b_6/f complex and onwards to PS1. Compared to aqueous redox-mediated systems – the withing the by lipid layer compartmentalized redox system should have superior charge transfer performance as all the components are close to one another. To keep the construction process of the PhotoSomes simple and cost-effective and to avoid additional downstream process steps, charge transfer will be accomplished in the bilipid membrane by endogenous quinones already present in the cyanobacterial thylakoid fragments and the archaeal lipids.

4.4. Catalytic center

H_2ases are large metalloenzymes featuring an active metal complex within the protein structure. To allow for a catalytic reaction, H_2ase is equipped with gas/water channels and pathways for proton, electron, water, and gas transport from and to the active site. Most H_2ases are bidirectional catalysts, acting both as H_2-producing and H_2-uptake enzymes and are capable of catalyzing the para – to ortho dihydrogen conversion. Compared to other H_2 evolution catalysts, they are nontoxic, don't rely on noble metals and show small overpotential [105]. H_2ase are classified by the structure of their active centers into [Fe]- or [Hmd]-, [FeFe]-, [NiFe]- H_2ase or by redox partners like b- or c-type cytochrome or NAD(P)+. H_2ase is further classified by location within the cell into membrane-bound (MBH), soluble (SH) or regulatory H_2ase (RH). Regulatory H_2ase, senses the presence of H_2 and shows only low TOF_{H2}. Catalytic activities of [NiFe]-H_2ases are usually low compared to [FeFe]-H_2ases [130].

The [FeFe]- H_2ase tends to be more active in the production of molecular H_2 and the [NiFe] – H_2ase in the oxidation of H_2. Electron transfer to the catalytic/active bimetal center is accomplished by a series of 3 iron-sulfur clusters, the proximal, medial, and distal cluster. As the distal Fe-S cluster is located on the outside of the H_2ase, it is essential for efficient DET connections to a photosensitizer. Since water splitting also produces O_2, H_2ase must be stable under oxidation while still exhibiting sufficient TOF or activity. Protein film electrochemistry, with H_2ase immobilized as monolayers on an electrode is mainly used to study the performance H_2ase for direct measurement of the catalytic activity, i.e., the turnover frequency TOF as a function of the electrode potential. H_2ase is compared to other standard inorganic molecular catalysts with a typical size of ~5nm quite large. [139]

[Fe] -/ [Hmd] H_2ase is found in methanogenic archaea and an iron-sulfur-cluster-free H_2ase. Only in the presence of a second substrate, it is capable to activate H_2. [Fe]-H_2ase is light-sensitive and thus not useful for solar H_2 production. [139]

[FeFe]-H_2ase is found in certain green algae, anaerobic eukaryotes, fungi, ciliates trichomonads and anerobic prokaryotes like *Clostriadia*. Most researched and applied for SAPSs are *Clostridia* and *Desulfovibrio* species [FeFe]-H_2ase. [FeFe]-H_2ase shows the highest catalytic efficiency with H_2 turnover frequency of up to 10000 s^{-1} but is sensitive to O_2 [55]. There has been estimations, based on perfect conditions with optimal electron transport on bare gold electrode of TOFs up to ~21 000 s^{-1} with an overpotential of 150 mV SHE. [102, p. 1] [FeFe] – H_2ase is sensitive to CO, CO_2 and O_2. O_2 is damaging the [4Fe-4S] cluster of the H-cluster rather than the di-iron center [139]. H_2 production of [FeFe]-H_2ase can also be inhibited by H_2 but the inhibition constant is larger compared to [NiFe]-H_2ase. This might be caused because of H_2 crowding in the gas channels [139].

[NiFe] – H_2ase shows lower TOF_{H2} compared to [FeFe]-H_2ase. As mentioned above, in the presence of H_2 [NiFe] – H_2ase faces strong product inhibition. [NIFe] – H_2ase is also sensitive to CO, CO_2 and O_2. The O_2 tolerance of O_2 – tolerant [NiFe] H_2ase might be the due to the existence of a modified proximal [4Fe-3S] cluster. O_2 tolerant [NiFe] – H_2ase is found in *E.coli. E.coli* has two membrane-bound H_2ases, only Hyd1 being oxygen tolerant. Most H_2ases suffer from O_2 inactivation, only O_2 - tolerant [NiFe] H_2ase is able to sustain H_2 oxidation in the presence of O_2. [139]

[NiFeSe]-H_2ase is a subclass of [NiFe]-H_2ases with a selenocysteine residue coordinated to Ni at the active site. [NiFeSe]-H_2ase is one of the preferred H_2ase for solar H_2 production, because of its excellent H_2 evolution rate, low product inhibition as well as tolerance toward O_2, allowing for the accumulation of oxyH_2.[80] The medial iron-sulfur cluster in all [NiFeSe]-H_2ases is comprised of a [4Fe-4S] rather than a [3Fe-4S] unit. *Desulfomicrobium baculatum (Dmb*) [NiFeSe]–H_2ase is most commonly applied for SAPS, not only due to its high H_2 evolution activity, lack of H_2 inhibition and O_2-tolerance but also for its titaniaphilicity.[105] Sakai et al. showed a drop of TOF_{H2ase} with *Dmb* [NiFeSe] from 13.9s^{-1} at 0% O_2 to 11.9s^{-1} at 5% O_2 down to 1,5s^{-1} at 21% O_2. [103]

Performance H2ases				
Type	***Organism***	***TON (s^{-1})***	***Electron source***	***References***
[NiFe]	*Desulfovibrio gigas*	3	MV	[88]
[NiFe]	*Ralstonia eutropha*	75	MV and dithionite	[111]
[NiFe]	*E.coli Y'227C-Hyd-1*	initial: 40 steady state: 7	TEOA	[110]
[FeFe]	*Clostridium pasteurianum*	1700	Dithionite	[140]
[FeFe]	*Clostridium actobutylicum*	250	MV	[118]
[FeFe]	*Clostridium acetobutylicum*	25	ascorbic acid	[32]
[FeFe]	*Clostridium acetobutylicum*	380 /980 (low/ high light intensity)	ascorbic acid	[102]
[NiFeSe]	*Desulfomicrobium baculatum*	27	methyl viologen (MV)	[103]
[NiFeSe]	*Desulfomicrobium baculatum*	50	TEOA	[93]
[NiFeSe]	*Desulfomicrobium baculatum*	14	TEOA	[103]
[NiFeSe]	*Desulfovibrio vulgaris Hildenborough*	986	methyl viologen (MV)	[107]

H_2ase - mimics				
[Fe_2S_2])	H_2ase mimic ([(m-SPh-$_4$-NH_2)$_2$$Fe_2(CO)_6$]	100 h^{-1}	ascorbic acid	[117]
[FeFe]-mod	*modified artificial [FeFe]-H_2ase mimic*	50 h^{-1}	ascorbic acid	[116]

Tab. 14 Performance of H2ases

An in-depth review of O_2 sensitivity and H_2 production activity of H_2ases has been written by Lu et al. [140]. They listed several different H_2ase half-lifes, ranging from 720 to 3 minutes at oxygen partial pressures below 0.1 atm. In a comparison of oxygen tolerance of several H_2ase, tests never exceeded durations of 24 h for [NiFe]-H_2ase and 1h for [FeFe]-H_2ase. Possible options for engineering an O_2 resistant H_2ase are molecular mechanisms based on blocking O_2 diffusion to the active site by mutated residues along the gas diffusion tunnels within the enzyme by replacing the residues with larger hydrophobic amino acids or by external blockages to the protein body. Internal - chemical strategies try to convert O_2 into harmless products, for instance ROS into H_2O, by replacing amino acids near the active site with Cys. External techniques like immobilization of H_2ase in an O_2- reducing redox polymer also succeeded. [140]

For simple, cost-effective production of PhotoSomes, the endogenous membrane bound H_2ase from the cyanobacterial thylakoid membrane fragments (UTEX 2973 *Synechococcus elongates)* will be incorporated into the liposome.

4.5. Stability and performance of PhotoSomes

The stability and performance of PhotoSomes are critical parameters for the system's scale-up and economic feasibility. As the TELs are stable at low pH, oxidation, and high temperatures, they face structural challenges. Photoactive liposomes might become unstable during photocatalysis or in the dark because of coalescence into large assemblies by aggregation, membrane rupture due to photochemical oxidation of its lipid components or to the formation of holes. This could be mitigated either by strengthening of the bilipid through additives, as cholesterol, electrostatic repulsion by doping the liposomes to create a charged membrane or adding steric hindrance by introducing polyethylene glycol-containing lipids in the lipid mixture forming the membrane. Osmotic pressure created by the concentration of membrane impermeable solutes, especially of the inner compartment of the liposome, might influence the water flow through the bilipid membrane leading to hypertonic conditions resulting in shrinking or swelling, in extreme cases bursting of the liposome. [1] The archaeal TELs are stable in ambient conditions for two years.

The literature about the stability of thylakoid membranes in *vitro* and *vivo* is scarce and ranges in experiments in bio photoelectric cells from up to one week [126] to minutes in more hostile conditions in a PEC SAPS setup [127]. In a study on the thermal stability of pea thylakoid membranes adapted to low light conditions, the thylakoid membranes showed a lower thermal stability compared to moderate light conditions. The first heat induced denaturation of the protein complexes of thylakoid membranes occurred at 57 °C. Denaturation of LHC2 occurs at 73 °C. The low-light thylakoids reached these limits 1-2 °C earlier [141].

However, there is more information about the stability of the individual PS1 and PS2 complexes.

Despite PS2 setting a benchmark in terms of O_2 evolution rate under ambient conditions for the development of synthetic catalysts [90], PS2s half-life is very low. In *vivo* only about 20 min and *in vitro* immobilized in a redox polymer up to 55 min [142]. In nature, PS2 is stabilized by a continuous repair mechanism. PS2 inactivation from high-intensity light is not a mechanism of increased

photodamage to PS2, but much more suppression of the repair mechanism through inhibition of protein synthesis by the generation of ROS, H_2O_2, $^1O_2$ by excess light energy [81], [143]. The photodamage becomes apparent as soon as the rate of photodamage surpasses the repair rate. The repair mechanism is based on the removal of degraded D1 protein in PS2. The rate of photodamage is proportional to the intensity of incident light. Under moderate light intensity, photoinhibition is not apparent. However, other abiotic stress factors, as low temperature (repair inhibitor), salt stress (repair inhibitor) have also been known to negatively affect PS2 lifetimes [143].

PS1-based photoelectrodes have been tested up to 30 days [144] and face stability issues such as ROS damage [145]. PS1 photoinhibition is caused by O_2^- and O_2 produced in the thylakoid membranes by highly reduced electron carriers in PS1, causing damage to the P700 site. Higher plants have superoxide dismutase and ascorbate peroxidase in their chloroplasts to detoxify ROS [146]. Without these protective enzymes isolated PS1 faces photoinhibition. Protecting PS1 from O_2 is crucial for long term-stability. Furthermore, chilling induced photoinhibition at 4 °C has been described [113].

Hu et al. found in their study of effects of heat treatment on protein structure and pigment microstructures in PS complex no significant change in the protein structure below 50 °C, first conformational changes at 60 °C. Also, the oxygen uptake rate decreased by 90.81 % at 70 °C and was completely lost at 80 °C. [147] The recovery of photo inhibited PS1 is slow compared to PS2 [146].

As these repair mechanisms are part of the overall cell metabolism, they are missing in purified photosystems and might not be existent or active in thylakoid fragments at all. For protection from photodamage, PhotoSomes will rely solely on the compartmentalization or encapsulation provided by the TEL liposome. To minimize photodamage, photosensitizers should be protected from exposure to strong light, in particular, light in the UV and blue light spectra [143].

Because of the numerous factors influencing STH of PhotoSomes, without lab experiments, only a rough estimation of STH of PhotoSomes is possible based on the efficiency estimation of photosynthesis of Hall and Rao [148].

Based on the full solar spectrum, 53 % of light is within the 400-700 nm active range. Only about 70 % of these in–active-range photon hitting the photoactive components and are fully absorbed resulting in 37 % of absorbed energy. Then 24 % of absorbed photon energy are lost because of wavelength mismatch degradation to 700 nm, resulting in 28 % of initial energy input. At this point, an estimated 25 % conversion efficiency within the quinone charge-transfer and the H_2 reduction at the H_2ase because of imperfect orientation and location of the thylakoid membrane fragment seems reasonable, leading to a 7% STH for the final, fully optimized, PhotoSome system.

Given the superior stability of archaeal tetrahedral lipids, stabilizing and incapsulating the photosensitizers and H_2ase and improvements in PhotoSomes during development, a 7% STH and a stability of 6 months seem reasonable for further considerations for scale-up of the fully optimized PhotoSomes system. The operating temperature should be between -4 to +55 °C.

5. The PhotoSome Process

After diving into the mechanics, limitations and inner workings of the single suspended photocatalysts "PhotoSomes", it is time to take a step back and take a bird's-eye view of the fully integrated PhotoSome process to get a deeper understanding of the bottlenecks and challenges in the scale-up of photocatalytic H_2 production via PhotoSome SAPSs. Therefore, the following process flow diagram of the complete PhotoSome System was designed, providing a schematic overview of the required unit operations for the H_2 production by semi-synthetic photosynthesis.

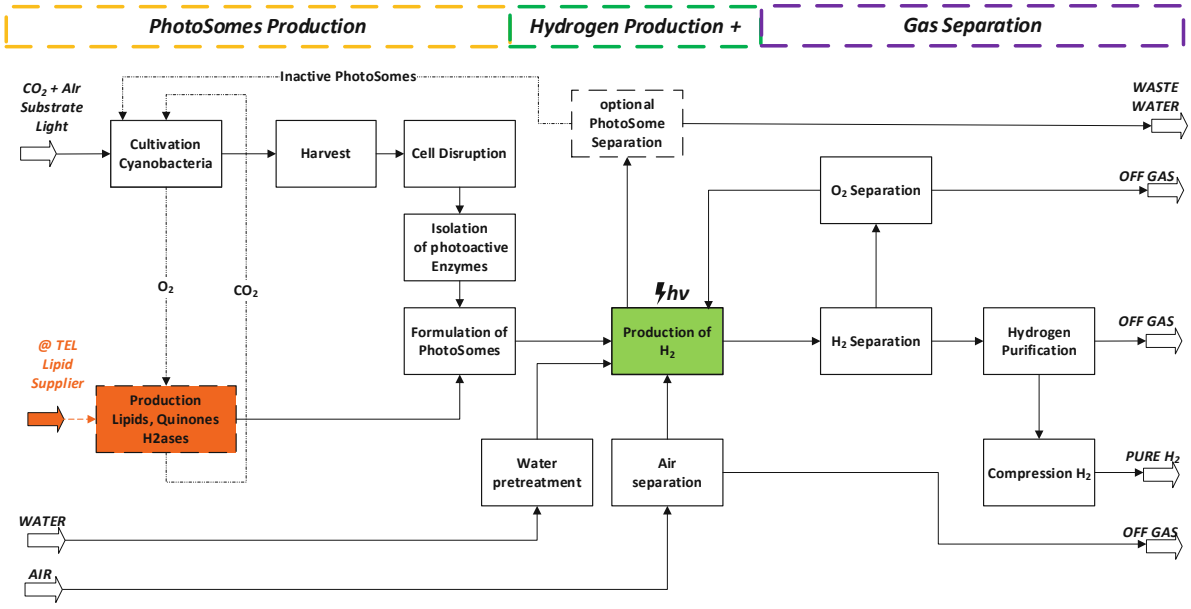

Fig. 13 Process flow diagram of the PhotoSome Process

The PhotoSome process can be split into 3 sections:

1	2	3
PhotoSomes PRODUCTION	H_2 PRODUCTION	GASSEPARATION
• cultivation of cyanobacteria • cell harvest • cell disruption • isolation of the (photoactive) enzymes, (thylakoids) • formulation of the PhotoSomes	• Production of H_2 – water splitting • water pretreatment (.. support process)	• H_2 separation and purification • O_2 separation • Compression H_2 • Air separation (.. support process)

The PhotoSome - process starts with the cultivation of cyanobacteria as the source organism of the photoactive thylakoid membranes. Extracting these membranes consists of a harvesting step to separate the cyanobacteria cells from the cultivation media for the cell disruption, followed by a cell disruption to lyse the cells and dispense the thylakoid membrane fragments. The thylakoid membrane fragments are then incorporated – formulated - in stable TEL lipids with quinones and H_2ases into the so called PhotoSomes liposomes. This process section is called PhotoSomes PRODUCTION.

The next section – H_2 PRODUCTION consists of the photocatalytic water splitting process and the support process of water pretreatment. In water suspended PhotoSomes split water by impacting

sunlight into H_2 and O_2. To prevent this gas mixture from exploding spontaneously, an inert gas, in the final concept N_2, is used to dilute the O_2-H_2 mixture into a non-flammable H_2-O_2-N_2 gas mixture. To provide water for the H_2 production and prevent unwanted contamination of the system, as well as an accumulation of minerals in the photo reactor (PR), a water pretreatment is necessary. A decontamination or cleaning concept should be considered to keep unwanted contamination from spreading.

This is followed by the process section of GASSEPARATION. By separating the H_2 from this gas mixture, the H_2 can safely be compressed and stored. To recover the N_2 for the explosion suppression, O_2 is separated in the following step, the N_2 is kept within the production loop. Inevitable N_2 losses during gas separation are compensated by air separation. To meet high H_2 purity standards, further purification will be required.

5.1. Operating Conditions

The PhotoSome process will operate close to ambient temperature and pressure conditions to lower the structural requirements on the photo reactor panels. For further considerations, a 40°C gas temperature in the photo reactor and pressures below $1.1 \cdot 10^5$ Pa are assumed.

5.1.1. Solar Energy Input.

The system is heavily influenced by the solar energy input and daily as well as yearly solar cycle. To simplify the first estimations, an average daily irradiation per square meter based on the yearly solar radiation and 12 hours of daily operation with constant H_2 production rates is assumed. The inherent daily and seasonal intermittence nature of solar radiation is for this first study not further considered. In Austria the global yearly ranges according to the World Bank's solar resource map between 913 and 1314 kWh/m^2. A medium value of 1250 kWh/m^2 will be applied for further considerations [149].

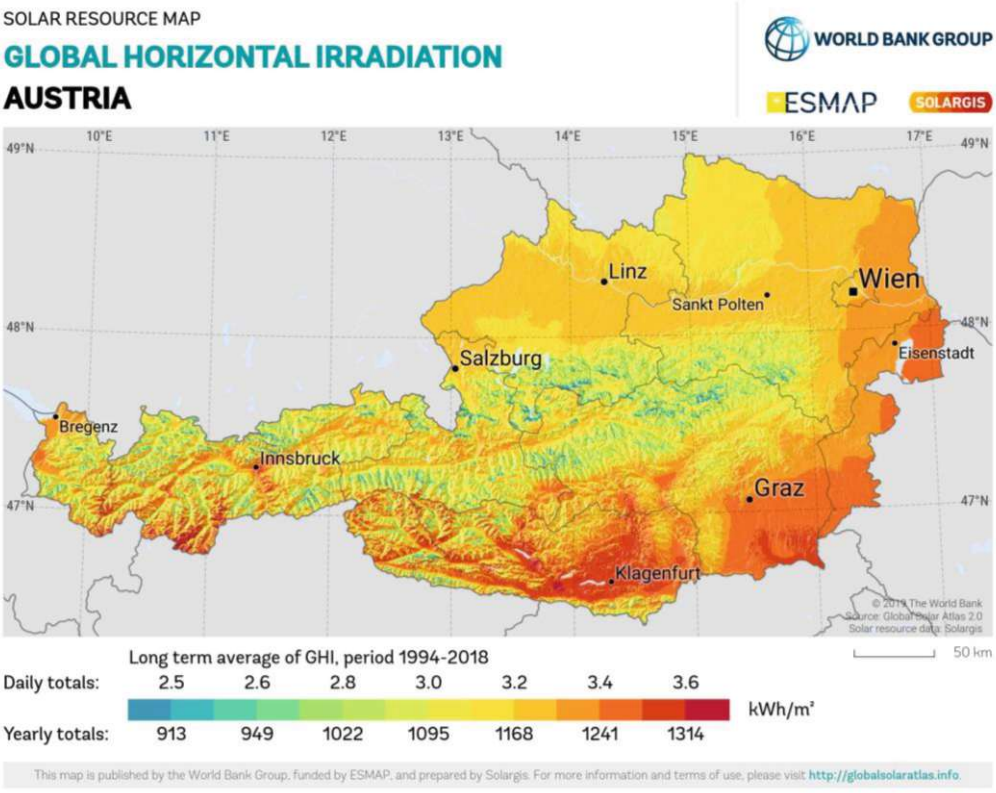

Fig. 14 Solar Resource Map of Austria. Source: https://solargis.com/maps-and-gis-data/download/austria Reproduced with permission from SolarGis and World Bank under CC-BY 4.0 .[149]

5.2. The Safety Issue:

Single-bed photocatalytic systems produce O_2-H_2 gas mixtures, creating an explosion hazard. The flammability of H_2 in a pure oxygen atmosphere ranges from 4% to 95%. Compared to traditional fuels, H_2 has a larger flammability zone, a lower ignition energy and a higher deflagration index, thus a higher probability of explosion or fire.

Literature describes 3 techniques to deal with this issue.

a. ***Dilution*** of the oxyH_2 gas with an inert gas to create a non-flammable gas mixture until the separation of H_2 [150], [151].
b. ***Explosion proofing*** the system + minimizing volume of combustible gas + quick gas processing + separation under vacuum [62].
c. ***Safety by Prevention*** – synthesizing a H_2 - based high value product, for instance, formate, methanol etc. avoiding the formation of an explosive atmosphere in the first place [55].

An example for ***b. explosion proofing***, is Nishiyama's et al. photocatalytic pilot plant. They explosion-proofed their pilot scale photocatalytic H_2 production plant by intentionally igniting the system's gas and optimizing the individual parts to withstand an explosion [62]. Together with minimizing the gas volume in the system, a reduction of fuel by keeping the free head volume of the flat plate collectors as small as possible, combined with quick gas processing, allows to minimize the impact of a spontaneous ignition of the system. The hydrogen separation was achieved by a membrane system with a vacuum pump to avoid compression of the explosive gas mixture [62].

Dilution of with an inert gas is the most feasible option moving forward as option b, explosion proofing with a large volume of oxyH_2 is too dangerous for large-scale scale-up and c, is not an option as this thesis focuses on H_2 production.

5.2.1. Dilution by an inert gas

The dilution of an $H_2 – O_2$ or H_2 - Air gas mixture has been topic in several papers. N_2, CO_2, He, and Ar are the most common inert gases to suppress explosions. As helium and argon are too expensive, only CO_2 and N_2 are considered as an option. The inert gas should also be readily available in close proximity to the PhotoSome plant as there are unavoidable losses in gas separation that need to be continuously replaced.

5.2.2. The flammability limits of H_2-O_2-CO_2 and H_2-O_2-N_2 gas mixtures.

The critical factors in comparing gas mixtures are the upper (UFL), lower flammability limit (LFL) and the limiting oxygen concentration (LOC). LFL and UFL describe the limiting fuel concentrations that can support flame propagation and lead to an explosion. Fuel mixtures outside of those limits are non-flammable. Flammability limits are determined by the gas mixture's composition and influenced by pressure, temperature, and humidity. The LOC is defined as the limiting concentration of O_2 below which, independent of fuel concentration, combustion is not possible. For a $H_2 – O_2 – N_2$, measured the LOC at 4.6-5 mol% O_2 [152]. A gas mixture will only be flammable if the O_2 concentration exceeds the LOC and the fuel concentration is between the LFL and UFL. These limits are listed in safety databanks such as CHEMSAFE® by Dechema for common gas mixtures or determined by elaborate experimental studies or calculated by kinetic models. There have been some studies into H_2 – air – CO_2 gas mixtures but only a few into H_2-O_2-CO_2 mixtures. The flammable range of H_2 gas in oxygen is 4-95% in a pure oxygen atmosphere [153]. However, some sources used a slightly different flammable range of H_2 in binary O_2 mixture, at normal operating conditions of 4 – 94% [150]. Extinction effects of CO_2 in oxyH_2 fuel occur when the CO_2 mole fraction is above 73% [154].

Hu. et al. measured in their experimental study of the LFL of $H_2/O_2/CO_2$ and $H_2/O_2/N_2$ an increase of the LFL of $H_2/O_2/CO_2$ from 4.25 vol% H_2 to 6.5 vol% H_2 and an increase of the LFL of $H_2/O_2/N_2$ from 4.25 vol% H_2 to 6.5% over an increase of dilution gas (CO_2, N_2) [153]. Furthermore, they determined that the specific heat capacity of the mixture mainly determines the LFL. Even though CO_2 directly participates in chemical and heat radiation, the chemical effect of CO_2 on the LFL of H_2 is small. The radiative effect on the lower LFL was improved by CO_2. Based on this data, the following flammability diagrams were constructed, with the LFL, UFL and extinction effect concentration.

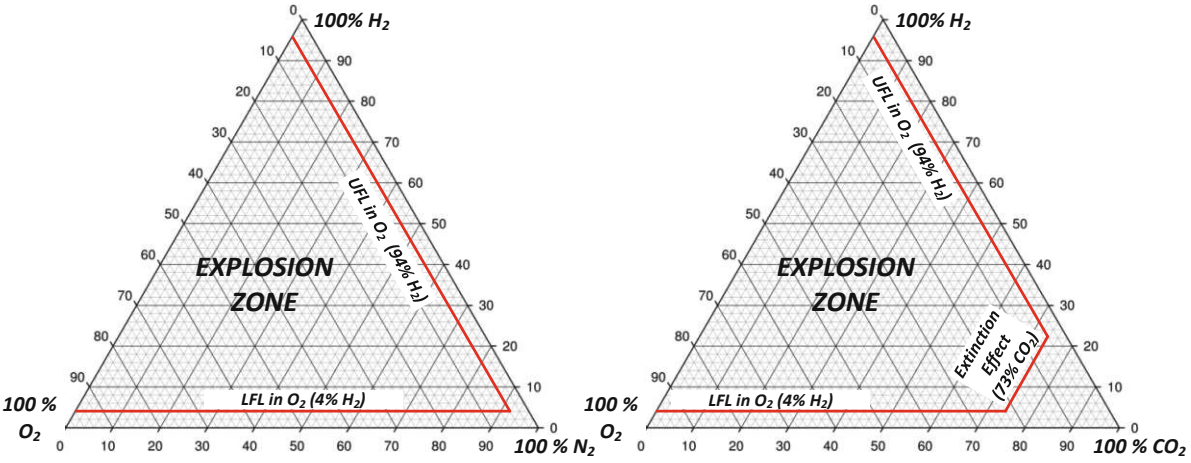

Fig. 15 Flammability Limits of trinary oxyH_2 gas mixture, left with N_2, on the right with CO_2

5.2.3. Pressure, temperature dependence and effect of water vapor on flammability limits.

Schroeder et al. showed in their study about explosion characteristics of H_2-air and H_2–O_2 mixtures at elevated pressures, an increase of LFL and first a decrease of the UFL until 20 bars followed by an increase with rising pressures. The LFL was lower and the UFL higher at 80°C compared to 20°C [155]. Medvedev et al. studied the flammability limits of H_2, air and water vapor mixtures, including after the formation of water microdroplets due to over-saturation of the gas mixture and showed that water vapor restricts the combustible range of H_2 [156]. Holborn et al. modelled the effect of water fog on the UFL of H_2-O_2-N_2 mixtures and observed a reduction of the UFL. In theory, their model would allow a prediction of the LFL of the H_2-O_2-N_2 mixtures. However, for lean H_2 mixtures, the formation of cellular flames and other instabilities make the prediction more complex. In addition, they found that the LFL was increased by the rising initial pressure and decreased by the elevated temperature [157]. When choosing a safe gas mixture for processing, one should bear in mind that flammability limits and LOCs, when determined have no built-in safety factor. In practice, such additional factors have to be implemented [152]. All gas separations are prone to losses and will need constant replenishment of inert gas. A local source, such as air, for the inert gas is a necessity. Direct air-capture of CO_2 is less mature and more expensive. Therefore, the N_2 was chosen as inert gas despite its larger explosive range.

Advantages - Disadvantages of dilution gases	
CO_2	***N_2***
Larger non-flammable area – higher initial H_2 concentrations possible. More unit operations possible for separations	Available in surrounding air at 78 vol% No negative effects to Lower NAFION permeability compared to CO_2 → relevant for EHC separation.
More complicated air extraction If not air recovered CO_2 → Problematic CO_2 emissions	Unproblematic emissions

Tab. 15 Advantages - disadvantages of dilution gases

Dilution of the process gas offers 2 additional benefits. First, because of the lower H_2 concentration, a higher H_2 production rate can be expected by avoiding product inhibition.

Secondly, it allows compression of the process gas. Compression of pure oxyH_2 is challenging from a safety perspective. The final safety concept for the PhotoSome process combines concepts b and c. Dilution by an inert gas with quick processing of gas and a reduction of gas volume in the system.

5.3. UNIT OPERATIONS

5.3.1. Cultivation of Cyanobacteria

Synecoccus Elongatus UTEX 2973, a unicellular cyanobacterium, chosen for its rapid photoautotrophic growth, cultivated in a photobioreactor (PBR) in waste stream substrates, for instance, potato cutting water under CO_2 uptake, will be the source for the thylakoid membranes. The most critical factors influencing biomass growth in a photobioreactor are light and mass transfer of gases. Conventional PBRs designs are flat plate, tubular, column, baggies and stirred tank with internal illumination. As cyanobacteria assimilate the CO_2 during growth, CO_2 fixation is an added benefit of PhotoSome production. Even though stirred tank PBRs offer the highest degree of control over the cultivation process, tubular PBR are preferred as they are the most widely used reactor type [158].

The ideal growth conditions for the rapid growth of *Synechococcus* UTEX 2973 are 38 – 41°C, 3% CO_2 and 500 µmol photos $m^{-2} \cdot s^{-1}$ using BG11 media, showing doubling times of 1.9 hours [159]. No additional nutrients, such as vitamins, are required to grow this cyanobacteria strain. Besides BG11, cheaper growth media, such as wastewater streams, are an option for cost optimization. As the only carbon source in autotrophic cultivation is air or CO_2, the supply must be maintained, and generated O_2 must be stripped out. To grow economically efficient phototrophic cultures, they must be light-limited, not by CO_2 transport and availability. R. Hasan achieved in a study of UTEX 2973 biomass yields of $0.65 g_{DW}/_L$ over 14 days in a 50:50 sturgeon and swine wastewater mixture [160, p. 83] less than in their control experiment in BG11 of $0.85 g_{DW}/_L$ over 14 days [160, p. 83]. Yu et la. reports biomass accumulation of 0.13 ± 0.01 mg/ml at the beginning of the experiments to 0.87 ± 0.03 mg/ml after 16 hours, outperforming several other cyanobacteria [159].

5.3.2. Harvest

The harvest unit operation separates the cyanobacteria from the culture media for further processing. The harvest of microalgae is one of the primary unit operations in microalgae processing, accounting for about 20-30% of processing cost. Common methods for algae harvesting include filtration, flocculation, flotation, and centrifugation.

Filtration is a process applying a semipermeable membrane, separating based on size exclusion. It can harvest highly concentrated cells from the medium and is able to handle delicate species that might be damage due to shearing. However, membranes can foul or clog up and require frequent

replacement, increasing processing costs. Flocculation is a process by which single free-floating cells aggregate together into larger particles with the help of flocculating agents such as iron and aluminum salt and can remove up to 95% of microalgae biomass. These flocculating agents present challenges because of their high toxicity and the subsequential additional process steps. Bio flocculants are cheaper and eco-friendly in comparison and capable of reaching 90% of cell recovery. Flotation is a process promoting the floating of cells on the culture media surface by utilizing small air bubbles. The advantages are high harvesting efficiency, high processing throughput, easy operating procedure and low cost. Centrifugation is a separation process based on each component's density and particle size via centrifugal force. Centrifugal systems include disc stack centrifuges, perforated basket centrifuges, imperforated basket centrifuges, hydro cyclones and decanters. This technique offers high cell harvesting efficiency and is a standard unit operation in downstream processing. Down sides are long processing times, high shear rates and high energy consumption [161].

As disc stack centrifuges are capable of large-scale continuous matter separation, offer high throughput and are common throughout the industry, they have been chosen for the harvesting unit operation.

5.3.3. Cell Disruption

The unit operation cell disruption will lyse the cyanobacteria and further fragment the thylakoid membranes into pieces for formulation into liposomes.

There are 5 fundamental methods for cell disruption, enzymatic, osmotic, thermal, chemical, and mechanical. Mechanical cell disruption techniques are ultra-sonic cell disruption, ball mill cell disruption, french press, and high-pressure homogenization. As high-pressure homogenization is a well-established, scalable, technique for cell disruption, it has been chosen. Based on inhouse experiments, the high-pressure homogenizations should be done in 3 executive rounds at 1200 bar. Depending on batch size, hydrodynamic cavitation could be an alternative. Waghmare et. la found in in their study of hydrodynamic cavitation for energy efficient and scalable microalgal cell disruption that compared to ultra sonication, it is significantly more energy efficient and a better scalable technology [162].

5.3.4. Isolation of the thylakoid membrane's fragments

The effort for isolation of the photosynthetic components increases with the purity. Separation of whole thylakoid membranes is relatively simple but further isolation of the individual components is more complex. As of now, it is not known whether whole thylakoid membranes can be used for the PhotoSome formulation, or the individual components are required. For now, the focus remains on membrane fragments.

For the isolation of the thylakoid membrane's fragments are 3 different unit operations possible, ultracentrifugation, precipitation, and gradient centrifugation.

Emek et. la described a 5-step process for the isolation by precipitation of whole plant thylakoids on a large scale:

1. Disruption of cells, followed by filtration to remove large cell debris and non-disrupted cells
2. Precipitation of thylakoids by adjusting the pH to the isoelectric point pH 4.7
3. Intermediate washing step with dilution of the precipitate in water
4. Second precipitation at pH 4.7
5. Freeze-thawing or freeze-drying step of the to concentrate the precipitate.

Dani and Sainis [163] investigated the isolation of the individual thylakoid components by ultracentrifugation at 3 rounds of 40 000, 90 000 and 120 000 g for 1 h. The pellet after each round

was collected and the supernatant was further subjected to centrifugation at higher speed. They reported that the sedimented fractions had all the components of the electron transport chain, phycobiliproteins, ATP synthase, ferredoxin–NADP reductase but no ferredoxin. Fraction from higher speeds higher enzymatic activities and higher rates of the whole electron transfer activity on a chlorophyll basis. The process followed these steps:

1. Washing cells with membrane isolation buffer (MIB) (10mM Tris-HCl pH 7.8, 10 mM $MgCl_2$; 50mM $NaHCO_3$; 1mM EDTA; 12 mM β-mercaptoethanol and 10% sucrose)
2. Storing the cell pellet in liquid N_2 at -70°C
3. Resuspension in MIB
4. Cell disruption by French press (100000 psi, single passage) or sonication for 30 min in pulse mode
5. Centrifugation of cell extract at 10000 rpm, 10 min to remove unbroken cells and large cell debris
6. Stepwise centrifugation of the supernatant at 40 000 g for resuspended in MIB, and the supernatant centrifuged at higher speeds.
7. Repeat of step 6 at 90 000 and 120 000 g.

At this moment, further experimental investigation is necessary for the most effective separation technique to be known. Precipitation is easy to scale up but requires further investigation, ultracentrifuges are limited by their volume, batch operations and long sedimentation times. Recently developed continuous flow ultracentrifuges, like the ThermoFischer® thermos scientific CC40 which offers process flows of up to 90 L/h, solve these limitations. However, these expensive systems are meant for large-scale operations and need to be fully utilized for cost-effective operations.

To simplify further consideration into the scale-up and as this unit operation still requires further investigation for the scale-up to a pilot scale system moving forward the isolation step consists of a preprocessing microfiltration to remove large cell debris and non-disrupted cells, followed by a conventional ultracentrifuge separation at 40 000 g for 15 minutes to evaluate a possible bottleneck with the isolation step. This will also help to show the limitations of ultracentrifuge unit operations.

5.3.5. Formulation of PhotoSomes

The formulation of the liposomes is based on self-assembly. For formulation, lipids are dissolved in an organic protic solvent and start the self-assembly process, arranging into bilipid layers when mixed with an aqueous phase. Most liposome formulation techniques consist of the following basic steps:

a. Creation of a lipid phase in an organic solvent
b. Hydration by an aqueous media to yield lipid dispersions.
c. Purification of liposomes
d. Analysis of the product.

There are several methods for liposome preparation. Standard methods include mechanical dispersion methods like Bingham or thin-film hydration method, sonication, french pressure cell, extrusion technique, micro emulsification and dried-reconstituted vesicles, solvent dispersion methods like ethanol – or ether injection and reverse phase evaporation and the detergent removal method. Novel methods include supercritical fluid technology with several different techniques, the heating method, freeze drying, double emulsion method and modified ethanol injection methods like micro hydrodynamic focusing, crossflow filtration, protoliposome technology, dual asymmetric centrifugation and membrane contactor technology[164], [165].
With feedback from the lipid's supplier, isopropanol injection - a crossflow solvent injection method,

was chosen as the preferred technology. The organic phase, which carries the dissolved lipids, is injected into a T-shape static mixer with the aqueous phase, carrying the thylakoid fragments. The rapid isopropanol dilution in the aqueous phase below a critical concentration leads to a self-assembly of the dissolved lipids in the aqueous phase. This leads to precipitation of the lipid molecules and aggregation. A crucial factor in the liposome formation is the ratio between organic to aqueous phase, in this case 1:2. Thanks to this high dilution, adverse effects due to any surfactants required to keep the thylakoid fragments dissolved in the aqueous phase should be mitigated.

This bulk technology is easy to scale up and frequently used. For instance, Polymun Scientific claims to be capable of producing 250 L of liposome preparation within 1.5h with one module. Several modules can run in parallel [166]. Also, no complex, expensive equipment is required. Further advantages are the use of non-harmful solvents, the formation of small unilamellar vesicles without sonication or extrusion unit operations and no oxidative alterations or degradation of lipids occur in this process [164]. The main drawbacks are, the heterogeneous population of liposomes, the removal of the organic solvent from the liposome dispersion and the risk of inactivation of biologically active macromolecules in the presence of isopropanol [167].

To reconcentrate the liposomes and to remove the organic solvent from the mixture, the formulation is directly coupled with an ultrafiltration crossflow membrane separation. The concentrated PhotoSome mixture is then ready for injection into the Photoreactor.

5.3.6. H_2 Production

The PhotoSomes will be injected into the water-filled photo reactor and start water splitting under impacting sunlight. Photo reactors are quite complex as they represent a 3-phase system with the particulate catalyst, the aqueous and gaseous phases. The first concern in designing the PR is the photosynthetic behavior of the PhotoSomes. Suppose it resembles the behavior of phototropic microorganisms. In that case, it will require a sufficient volume to account for the growing amount of biomass in the system and the increasing of volumetric photosynthetic surface, also increasing shading effects preventing photoinhibition. Alternatively, it could resemble artificial catalysts requiring a small water column to reduce the loss of light by absorption of the water column and other catalytic particles. Miyake et al. researched the light penetration in a bundle of several stacked flat plate photoreactors filled with a cell culture. They showed an almost complete drop of light intensity within 20 mm [168].

Further requirements are:

- Low head space to reduce the gas volume in the system.
- Uniform distribution of the photocatalyst in the aqueous media
- Complete coverage of the illuminated area by the photocatalyst for max. effective photon capture area.
- Mechanical requirements such as internal gas pressure, wind, and snow loads
- Stability against environmental hazards - e.g. hail proof.
- Cleanability – CIP stability or option of automatic cleaning by robots (dust/snow) or sonic clearing methods – even on the outside
- High light transmissibility and low light reflection of the glass.
- Temperature stability within set limits
- Simple, cheap construction and easy and quick assembly, mass-producible

Typical photoreactor designs for suspended catalysts are flat-plate, tubular, baggies or single bed and dual bed systems.

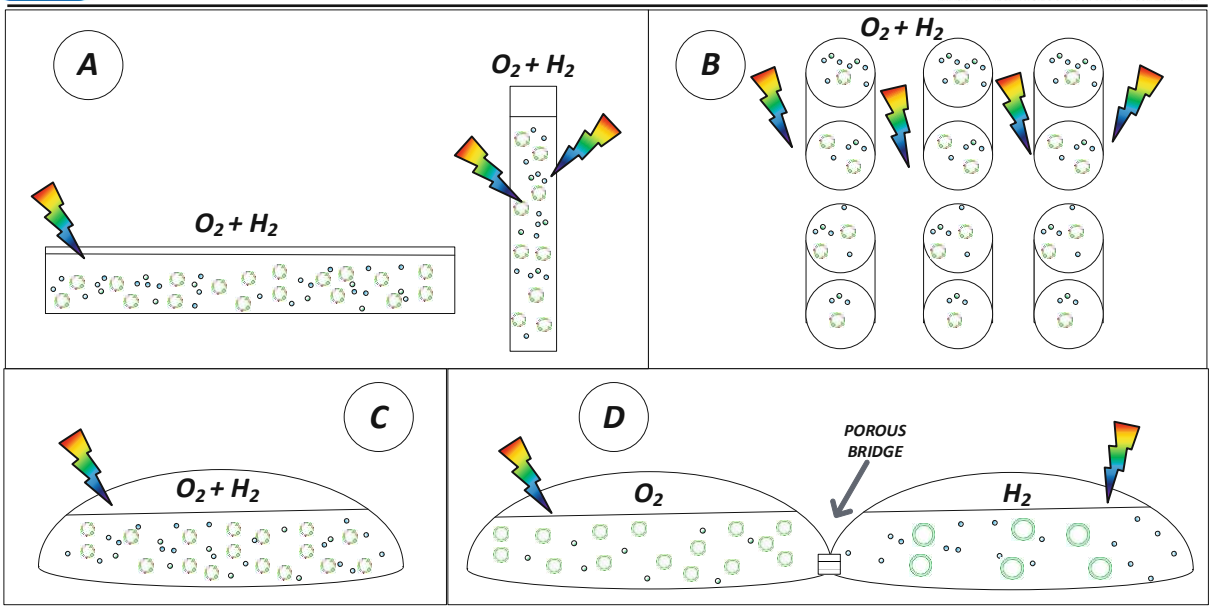

Fig. 16 Photoreactor Designs as cross-sections, A, flat plate; B, tubular; C, single bed; C dual bed

Flat plate systems are constructed of a metal bed or frame with either 1 or 2 glass panels. They can be mounted vertically, tilted or horizontally. Tubular systems comprise of a set of transparent tubes in either a vertical or horizontal position. Baggie or single bed systems have been used as bio photo reactor systems. Pinaud et al. proposed such a design for photoreactors for suspended photocatalyst [31]. They comprise of a long, flexible, transparent, tube-shaped plastic foil that sits on the ground and is filled with the aqueous medium and the photocatalyst. Dual bed systems connect two of these systems filled with 2 different photocatalysts with by a porous bridge, thereby spatially separating H_2 and O_2 evolution and avoiding separation in the first place. This system effectively halves the STH efficiency, since 2 separate reactions are necessary doubling the required reactor area in the process. Pinaud et al. describe the advantages and disadvantages of single and dual bed systems in detail [31].

Even though tubular systems are regarded superior in performance, baggie-based systems might be cheaper in construction than flat plate systems. Flat plate photo reactors have been chosen for further considerations, as it simplify estimation for the required amount of catalyst under the assumption of full coverage of the illuminated area by PhotoSomes in the reactor, simplifies the estimations of pressure loss in the gas loop and offer better cleanability. Also all previous pilot-scale photocatalytic systems used flat plate reactor designs [62], [65].

To prevent the issue of H_2 embrittlement and to account for the corrosive oxidative conditions in the photoreactor, stainless steel with at least 10% of Ni should be used in the construction.

Snow loads in Austria, are location and roof-shape specific, and can exceed 22 kN/m^2. As an example, the area-specific snow load for Wiener Neustadt is 1 kN. HORA, the Natural Hazard Overview and Risk Assessment Austria , offers an interactive map for snow loads based on the *ÖNORM B 1991 – 1-3:2022 05 15* [169].

5.3.7. Water pretreatment – The contamination issue

The large volumes of photo and photo bio reactors have repeatedly been challenged by contamination. Flushing and sterilizing such a system is costly and complex. Contrary to this, photocatalytic systems are investigated for water purification and removal of trace contaminants use cases. As previously mentioned TiO_2 – CuO photocatalysts catalysts created radicals that in tandem with solar irradiation, showed significant (>5 log) reduction in *E.coli* concentration in less than 10 minutes of treatment [66]. This gives reasonable evidence to assume of a high degree of self-

decontamination of the system. Still the PhotoSomes and non-active non-TEL liposomes / lipids that are injected into the reactor can act as a possible substrate. Therefore, and to avoid an accumulation of salts and minerals in the system, a commercial reverse osmose system will supply the water feed. The reverse osmose should be large enough to supply enough water for water splitting and fill the system in a reasonable amount of time. Since the inert gas supply will be accomplished via a gas permeation system, additional precautions to avoid contamination by the inert gas stream are not necessary.

5.3.8. H_2 separation

The goal of H_2 separation is the extraction of H_2 from the diluted gas mixture. The low H_2 concentration poses a significant challenge for standard gas separation technologies, as they are designed to remove impurities. Standard technologies are pressure swing adsorption based on adsorption, cryogenic distillation based on liquification or membrane technology. Even though cryogenic distillation and PSA are commercialized processes, pressure-driven membrane separation is considered a superior technology as they are regarded as less energy-intensive while still yielding high purity H_2.

Properties	***PSA***	***Membranes***	***Cryogenic***	***EHC***
Min feed purity [vol%]	>40	>25	15-80	< 5% possible
Product purity [vol%]	98 – 99.999	>98	95-99.8	up to 100%
H_2 recovery [%]	Up to 90	Up to 99	Up to 98	20% with one stage

Fig. 17 Performance of H_2 Separation Technologies, Source: EHC - own experiments,:[170]

The separation of oxyH_2 mixture has only been studied in a few publications. A few groups looked at liquid-supported membranes [171]. This immature technology still suffers from low lifetimes in the range of hours. Alsayegh et al. did economic studies on CO_2 and N_2-diluted oxyH_2 mixtures with polymeric membranes. They simulated and optimized an open 2-stage membrane separation process and achieved purities above 92.50% and recoveries >85% at costs of 6.15 to 8.2$\$_{2017}$/kg$H_2$ for the separation process without considering costs of feed gas neither the oxyH_2, nor the supply of inert gas. Their results are display in Tab. 16 Results of previous studies into oxyH2 .

MIX.	FEED	MEM.	PERMEANCE (GPU)			SELECTIVITY (Q_{H2}/Q_i)			RECOVERY	PURITY	COST $/kg$H_2$	Source:
H_2 O_2 N_2	6mol% H_2	UBE®	H_2 140	O_2 8.4	N_2 1.7	H_2 -	O_2 16.7	N_2 82.4	90%	95%	**6.15**	[150]
	4mol% H_2	UBE®	H_2 140	O_2 8.4	N_2 1.7	H_2 -	O_2 16.7	N_2 82.4	92%	92.50%	**8.2**	[150]
	ALTERNATIVE:	TIMP	H_2 3095.2	O_2 170.9	N_2 19.9	H_2 -	O_2 18.1	N_2 155.5				[150]
H_2 O_2 CO_2	76mol% CO_2, 16mol% H_2, 8mol% O_2	Proteus® H_2 – selective	H_2 300	O_2 6	CO_2 20	H_2 -	O_2 50	CO_2 15	85%	99%	**6.4**	[172]
H_2 O_2	50mol% H_2 / 50mol%O_2	Liquid PFTBA	H_2 3			H_2/O_2 140			N.A	N.A	N.A	[171]

Tab. 16 Results of previous studies into oxyH_2 mixtures.

Electrochemical H_2 separators / compressors (EHC) are a newly emerging technology. EHC selectively oxidizes H_2 electrochemically to positively charged H_2 ions. By applying of an electrical potential, the H_2 ions are transported through a semipermeable membrane, followed by a reduction on the permeate side to H_2. This allows for highly selective separation and isothermal compression of H_2 and is therefore often referred to as electrochemical H_2 compressors. This technology is capable of separating H_2 from low concentrations to pure H_2 in a single step. There hasn't been any research into the separation of diluted oxyH_2 mixtures with this technology. However, it seems quite promising for this separation requirement. The decision was made to investigate this possibility further by an experiment.

Moving forward 2 different gas separation concepts will be compared for the feasibility study. The **PSA - CONCEPT**: with a 2-stage H_2 membrane separation based on the work of. Alsayegh et al. paper "*Systematic optimization of H_2 recovery from water splitting process using membranes and N_2 diluent*" and **EHC - CONCEPT** based on a theoretical fully developed highly optimized EHC system.

5.3.9. O_2 separation

To avoid an accumulation of O_2 in the gas loop, an oxygen separation is necessary. Since the maximum O_2 in the gas loop is limited by LOC in the permeate and retentate stream of the H_2 separation a high degree of O_2 removal is required.

For the PSA-Concept, the oxygen concentration of the backflow into the gas loop limits the max. concentration of H_2 in the loop as an increase of O_2 partial pressure in the gas loop and consequentially in the feed stream to the H_2 separation would lead to an increase of O_2 in the permeate of the first H_2 membrane separation stage above the LOC and again the formation of an explosive gas mixture. Since the hydrogen concentration is directly coupled to the oxygen concentration by the stoichiometric balance of water splitting of 1:2 this lowers the max H_2 in the gas loop even below the LFL of H_2.

The challenges faced here are similar to the ones of the H_2 separation. PSA is not a viable option for O_2 separation given the low oxygen concentration and exacerbated by the fact that most adsorbents are N_2 selective and the few O_2-selective adsorbents, such as RHO zeolites, are still at the development stage or suffer from low selectivity.[173] Cryogenic separation is energy intensive. Thus, membrane separation is the preferred method.

An essential parameter for gas permeation is the kinetic diameter of the gas components. Smaller kinetic diameters lead to higher permeability and thus affects also the selectivity. Kinetic diameters for are 2.89 Å for H_2, 3.30 Å for CO_2, 3.46 Å for O_2 and 3.63 Å for N_2 [174]. This can be an issue with CO_2-O_2 separation as the kinetic diameter of CO_2 is quite unintuitively smaller than that of O_2 making

a selective separation of O_2 difficult. This an additional reason to choose N_2 as an inert gas for the gas loop.

As membranes generic PI hollow fiber membrane have been chosen with typical material specific performance parameters provided by a review of Himma et al., „Recent Progress and Challenges in Membrane-Based O_2/N_2 Separation“ [175].

For the PSA CONCEPT, in order to reduce the loss of N_2 in the 2nd stages of the H_2 gas separation and since the retentate stream of the second stage has a higher N_2 concentration than air, a second O_2 separation will be implemented into the PSA concept.

5.3.10. H_2 Purification

To meet the quality requirement set by H_2 fuel standards, a final H_2 purification is necessary. While the EHC – CONCEPT, thanks to the H_2 selective separation, does not need any further purification, PSA CONCEPT requires a two-step purification system. The first stage consists of a catalytic oxygen conversion to reduce the oxygen concentration by recombination into steam, followed by a PSA to remove the remaining N_2 from the gas mixture:

5.3.10.1. Catalytic Oxygen Conversion DE-OXO Cat

As oxygen would be adsorbed and enriched in the PSA adsorbents, again allowing for the formation of a flammable environment in certain operation cycles e.g., loss of pressure, a catalytic recombination of the remaining oxygen to water after the membrane separation is necessary. This will also allow the system to meet the high H_2 purity requirement set by ISO 14687. As the O_2 concentration in this stream is quite low already, subsequent H_2 losses by recombination are below 1%.

Catalytic H_2 – oxygen recombination at room temperature has been researched mainly in the nuclear industry for H_2 removal in O_2-rich environments to prevent the formation of explosive atmospheres. However, catalytic oxygen removal from H_2 to meet purity standards, not yet achieved by certain electrolyzer concepts, has renewed in this field of interest. Pt and Pd – based metal catalyst shows high H_2-O bonding reaction activities since both H_2 and O_2 have strong affinity to Pt and Pd. H_2 and O_2 molecules adsorb on the catalyst surface, dissociate, ionize and recombine to water in an autocatalyzed, exothermal reaction, even at room temperatures. The main bottlenecks of these catalysts are deactivation of the catalyst by the creation of a water film by the produced water molecules and creation of a hot spot of more than 700 °C on the surface of catalytic particles by this exothermal reaction and subsequent local ignition and explosion. Also, at temperatures below 300 °C, Pd is easily embrittled by H_2 and Pd-Pt catalysts are prone to irreversible sulfur poisoning and deactivation by deposition of carbonaceous materials [176].

Kim et la. showed a 100 % H_2 conversion of several Pt, Pd and Pt-Pd catalysts at 25 °C and 55 % relative humidity with H_2 concentration of 1.5 %. Lower H_2 concentrations showed lower conversion rates [177]. Most studies were conducted with dense or fluidized bed systems, however there has been a study on catalyst devices using cellular ceramics that showed better pneumatic performance and improved heat distribution [178]. Still, there remains a lack of studies around removal of trace oxygen e. g. low oxygen in high H_2 concentrations. As studies show improved performance at higher H_2 concentrations, moving forward a not yet available ceramic honeycomb DE-OXO-catalyst with a hypothetical 100% oxygen conversion rate will be implemented.

5.3.10.2. PSA H_2 Purification

The feed stream for the PSA purification already shows a high H_2 concentration and allows for economical purification at low losses. The system will be designed with 4 columns for continuous operation. Even though all oxygen should be removed by the DE – OXO stage, flammable carbon-

based adsorbents were dismissed in favor of a nonflammable Zeolites 5A. 5A shows superior performance and all necessary parameters for design were available by a study of the purification of waste H_2 to fuel cell grade [179].

5.3.11. Air separation of inter gas – CO_2 or N_2?

A steady supply of inert gas can only be ensured by a local source. As industrial sources are usually unavailable in proximity, air separation remains the most feasible source. Large-scale direct air capture technologies for CO_2 are under development in the effort to mitigate climate change. Costs are estimated to range between 335-125 $/$t_{CO2}$ [180], while on-site N_2 can drop down to around 33 $/$t_{N2}$ [181], giving N_2 a clear cost advantage. The challenges are again similar to the one mentioned in *5.3.9 Oxygen separation.* PSA systems can achieve purities of up to 99.999 % while membrane systems are usually limited to around 99%. Membrane systems offer advantages in both initial investment and cost of operation in smaller systems, while PSA are more cost-effective at large scale. A significant challenge for a basic engineering process design is the fact that commercial suppliers of high-performance N_2 air separation membranes such as Evionik with their SEPURAN® hollow fiber membranes, share their specifications and prices only with original equipment manufacturer. Thus, the same generic PI membrane from the oxygen separation was used for the cost analysis.

6. Experimental work

6.1. Gas separation by an electrochemical H_2 Compressor.

EHCs are a novel way to separate and compress H_2 gas from gas mixtures. Until now, no publications have been published on H_2 separation from H_2-O_2-CO_2 or H_2-O_2-N_2 mixtures via EHC. The prospect of highly selective hydrogen separation combined with the possibility of isothermal compression seemed promising and called for an experimental investigation. At the time of the experiments, CO_2 was thought to be the preferred inert gas, since it allowed for higher H_2 concentrations up to 18 vol% in the feed gas stream. The H_2 separation is more efficient from a concentrated gas stream. This raised the question of whether CO_2 reduction to CO would occur on the feed side and subsequentially deactivated to catalyst on the membrane. Due to technical issues and a limited time frame only H_2-N_2 and H_2-O_2-CO_2 mixtures were investigated. The goal of these experiments was a "*proof of concept*" of separating a trinary H_2-O_2-CO_2 gas mixtures and evaluating first performance parameters.

6.2. Determination of the flammability limits of a H_2, O_2, CO_2, gas mixture.

Preventing explosive gas mixture formation is the first step of the primary explosion protection. In order to design a safe and stable process for separating an oxy-H_2 gas, it is of the uzmost importance, especially for an electrochemical process, to prevent the gas mixture from igniting. This has already been discussed in *5.2 The safety issue* in detail.

Given that there are still open questions about the effects of humidity on the LFL on a H_2/O_2/CO_2 gas mixture and limitations of the mass flow controllers, in terms of already reaching the smallest possible H_2 – mass flow of the gas mixture system the following gas mixture was chosen for separation:

GAS	Mass flow [g/h]	Volume Fraction [vol%]
H_2	0.25	4.341
O_2	2	2.188
CO_2	117.5	93.47

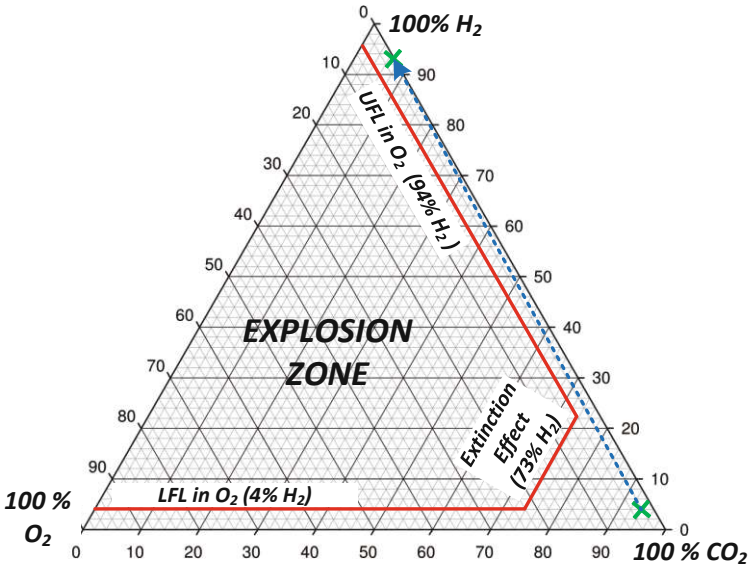

Fig. 18 H_2 separation by EHC

6.3. Experimental Setup:

The experiments were carried out on a prototype EHC at TU Wien built by Florian Fritsch for CH_4 – H_2 separation experiments. A detailed description of the EHC, the stack assembly and the experimental setup can be found in his master thesis, *"Design and testing of a membrane-based electrochemical H_2*

compressor"[182]. The experimental setup consists of a gas mixture table to provide the feed stream, the electrochemical H_2 compressor with the membrane stack, and an analytics bench to measure the volumetric flow or gas composition of either the retentate or permeate stream. A safety torch burns off the discarded gas stream. The gas mixture table is equipped with 4 BRONKHORST (Kamen, Germany) mass flow controllers (MFCs) to produce a defined gas mixture and feed gas flow. Gas bottles supply the gases. The MFCs are remote-controlled by a PC running a process control software.

The EHC is equipped with 2 power supplies, one for the support system and the other solely to power the membrane stack. A sufficient wetting of the proton exchange membrane is ensured by a humidifier filled with deionized water that's being bubbilized by the feed gas stream. The membrane stack is submersible by a crane in a thermostatic bath for temperature control. Further components are 2 Peltier coolers to dehumidify the permeate and retentate stream and several sensor and control systems. The membrane stack, described in Fig. 19, is the centerpiece of the system facilitating the separation step. The entire setup, including the membrane, was built and pre-used in experiments to separate H_2-CH_4 gas mixtures.

The following stack set up was used.

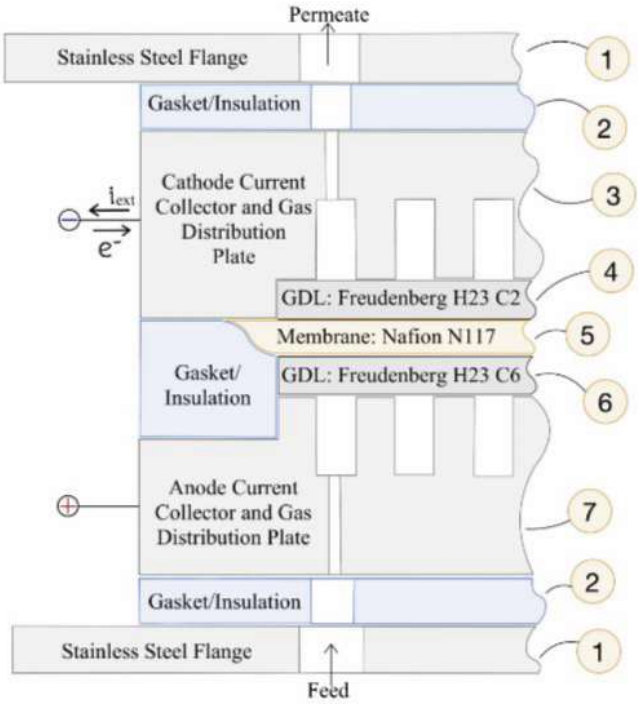

Fig. 19 Stack set-up EHC - Source: [182]

1. Stainless Steel Flange (V2A)
2. "Ice cube Sealing" made from a polyolefin elastomer for use with PEM fuel cells.
3. Cathode current collector plate made from aluminum (AlMg4,5Mn) with grooves for gas transport.
4. H23 C2 gas diffusion layer (GDL) for cathode side by Freudenberg – not treated with hydrophobic coating.
5. NAFION N117 CCM with a Pt loading of 0,3mg/cm2 on the anode and cathode side of the CCM. The Active Area is 70 by 70 mm.
6. H23 C6 GDL for the anode side made by Freudenberg - treated with a hydrophobic coating.
7. Anode current collector plate made from aluminum (AlMg4,5Mn)

Since there is only one gas analyzer, the composition of only one gas stream and the volumetric gas flow of the other stream or the volumetric gas flow of both streams can be determined simultaneously. In-line gas analysis was accomplished by a Sick GMS810 gas analyzer equipped with 4 separate channels, each exclusively measuring the CO_2, H_2, CH_4, CO content of the gas mixture. The volumetric flow rate of the permeate was measured using a "Definer 220 – L Rev C1" by Bios International Corp (NJ, USA).

6.4. Test Procedure

In preparation for the first test, the membrane stack was disassembled, the pre-used membrane inspected and for 24 hours, pre-wetted in deionized water. After reassembling of the membrane stack, the stack was reconnected to power cables, gas lines and sensor cables. The humidifier was filled with deionized water. The feed, retentate, and permeate side were subjected to a N_2 gas hold test to ensure a gas-tight system. After the safety torch was lit, all gas lines were flushed and filled with N_2, to ensure a non-flammable gas mixture within the system.

The initial gas mixture was set at 2.5 g/h H_2 and 75 g/h N_2 and was changed during the experiment to a 2.5 g/h H_2, 60 g/h CO_2 and 37.5 g/h N_2 until reaching a 2.5 g/h H_2, 120 g/h CO_2 mixture, then the H_2 mass flow was lowered to 0.25 g/h in preparation of the addition O_2. The goal was to keep a steady volumetric gas flow during changes in gas composition. After the reduction in H_2 mass flow, O_2 was slowly added to finally supply the system with a non-flammable gas flow of 0.25 g/h H_2, 2 g/h O_2 and 117.5 g/h CO_2.

The experiments were carried out at 3 V and 1 V, the feed gas humidity was kept above 70%. At the end of an experiment, all lines were again flushed with N_2 to ensure a safe atmosphere within the testbed. During the test 4th test run the experiment had to be paused for 70 minutes. The system was kept running with a pure CO_2 feed stream at a voltage of 3 V. After this break, no permeate stream could be established with a range of different H_2 – CO_2 and H_2 – N_2 gas mixtures. The membrane stack was disassembled for the 5th test run to install a new membrane. The disassembled collector and gas distribution plates showed heavy oxidation, especially on the feed or anode side. This oxidation layer was removed with sandpaper prior reassembly of the stack with a replaced membrane.

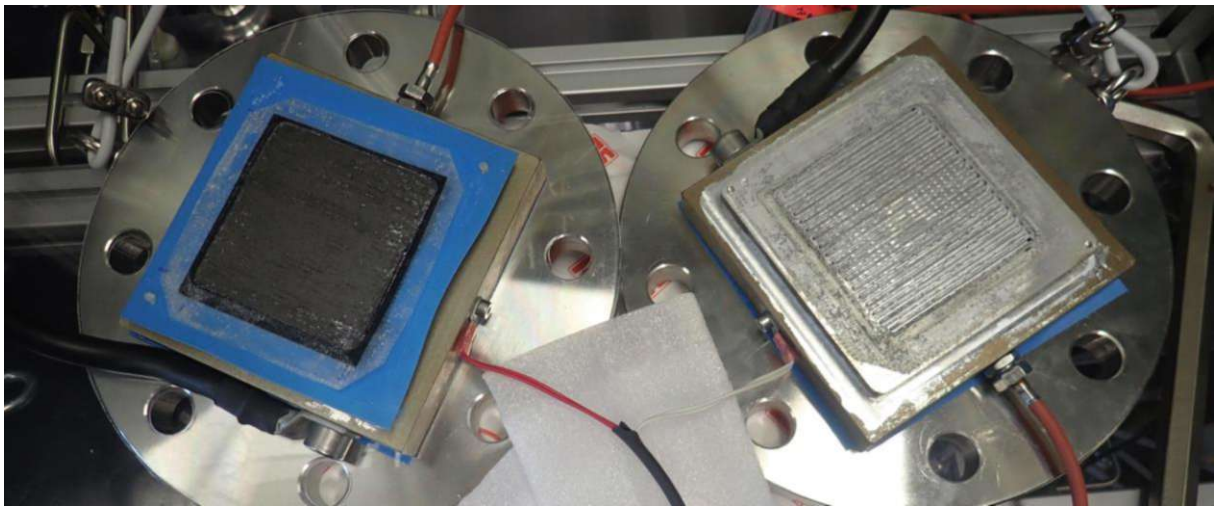

Fig. 20 left white oxidation on gas diffusion layer (black) and seal (blue); right: heavy oxidation on retentate current collector - gas distribution plate,

6.5. The CO_2 pressure hold test.

To study the effect of CO_2 diffusion to the permeate side, a pressure hold test was carried out. At first the entire system was flushed with pure CO_2 gas. Then the feed/retentate side was closed off and applied with CO_2 gas at 8.2 bar. On the permeate side, a 10 g/h sweep stream was applied and the change in CO_2 concentration measured.

6.6. Correction factors

Since a volumetric CO_2 gas concentration of 108% was measured during the experiment, it was necessary to apply a correction factor to the gas composition, calculated from measurements of the retentate gas stream.

The following 8 measuring points were chosen because they represent the most stable measurement at the end of each measurement series before changing to the following gas mixture. Here, the by the MFCs defined gas mixture of the feed stream was compared to the measured gas composition of the retentate stream and a correction factor for each measuring point was calculated by the following formulas.

$$calculated\ volumetric\ fraction\ of\ the\ Feed = \frac{\frac{mass\ fraction_i}{desity_i}}{\sum_{z=1}^{Z}\frac{mass\ fraction_z}{desity_z}}, (Eq\ 6.0)$$

$$Correction\ Factor = \frac{calculated\ volumetric\ fraction\ of\ the\ Feed}{measured\ volumetric\ fraction\ of\ the\ Retentate}, (Eq\ 6.1)$$

The measured H_2 concentration in the retentate stream is lower than the feed stream since the EHC separates a small fraction from the permeate. This difference is accepted but leads to a systemic error in the correction factor. However, this error is small because of relatively small permeate stream compared to the feed stream.

Gas	**Date**	*13. Sep*	*13. Sep*	*13. Sep*	*13. Sep*	*13. Sep*	*13. Sep*	*13. Sep*	*13. Sep*
[-]	**Time**	*13:45*	*14:36*	*16:12*	*17:47*	*18:03*	*18:32*	*18:44*	*19:06*
H2		1,09158345	1,06275247	1,03173263	0,5372841	0,82487148	1,808906556	1,80890656	0,895795907
CO2		0	0,84559186	0,843417194	0,89789643	0,87443491	0,849731219	0,84588628	0,872616825
N2		0	0	0	0	0	0	0	0
O2		0	0	0	0	0	0	0	0
					Discarded Values				

Gas	*Mean of all correction factors*	*standard deviation of all correction factors*	*mean + standard deviation*	*mean - standard deviation*	*Correction Factor new*
[-]					
H2	*1,13273*	*0,45304*	*1,58576*	*0,67969*	*0,98135*
CO2	*0,86137*	*0,02073*	*0,88210*	*0,84064*	*0,85528*
N2					
O2					

Fig. 21 Calculation of correction factor

Since the correction factors, especially of H_2, are distributed between 0.5373 and 1.81 the mean value and standard deviation were calculated and all factors outside of the standard deviation were discarded for the calculation of the correction factor.

6.7. Results

Since a volumetric CO_2 gas concentration of 108% was measured during the experiment, it was necessary to apply a correction factor to the gas composition, calculated from measurements of the defined feed gas mixture. The separation of a H_2 - N_2 gas mixture led to a higher permeate flow of 16 ml/min compared to 9 ml/min at the separation of a H_2/CO_2 mixture.

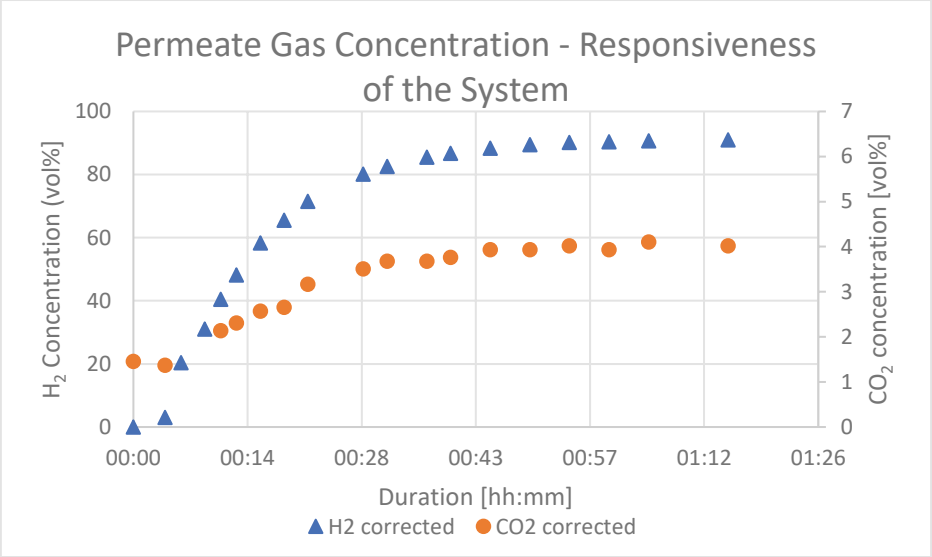

Fig. 22 Permeate gas concentration over time. Responsiveness of the measurement setup. Feed 0.25 g/h H_2, 2g/h O_2, 117.5 g/h CO_2

During the separation of a 0.25 g/h H_2, 2 g/h O_2, 117.5 g/h CO_2 gas mixture, a 91 vol% gas mixture was produced. This graph displays the responsiveness of the measurement setup. Because of the large dead volume and the small permeate stream, it took a long time until the gas concentration in the permeate stream stabilized.

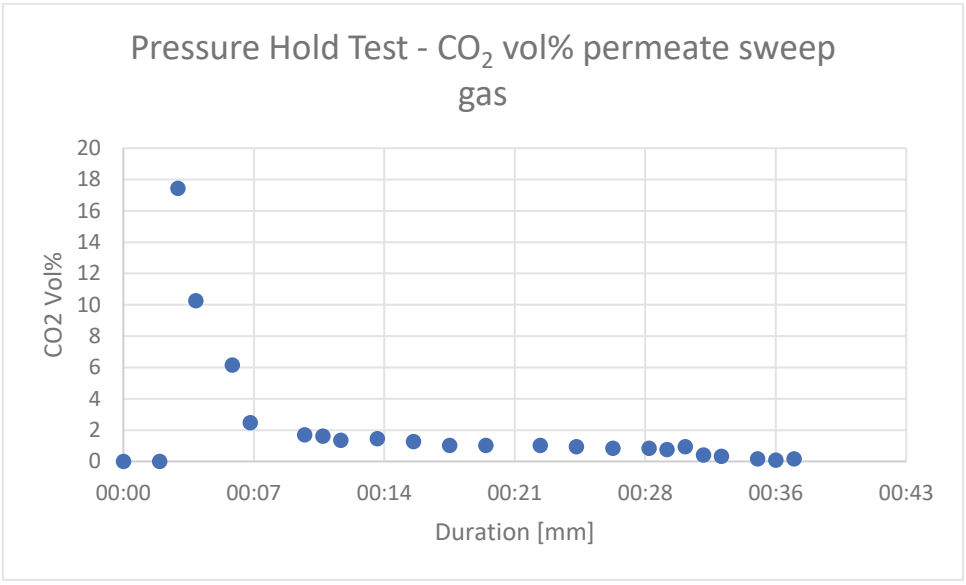

Fig. 23 Pressure hold test

The pressure hold test shows an initial spike to 18 vol% in CO_2 concentration on the permeate side slowly dropping down to 0.2 vol%.

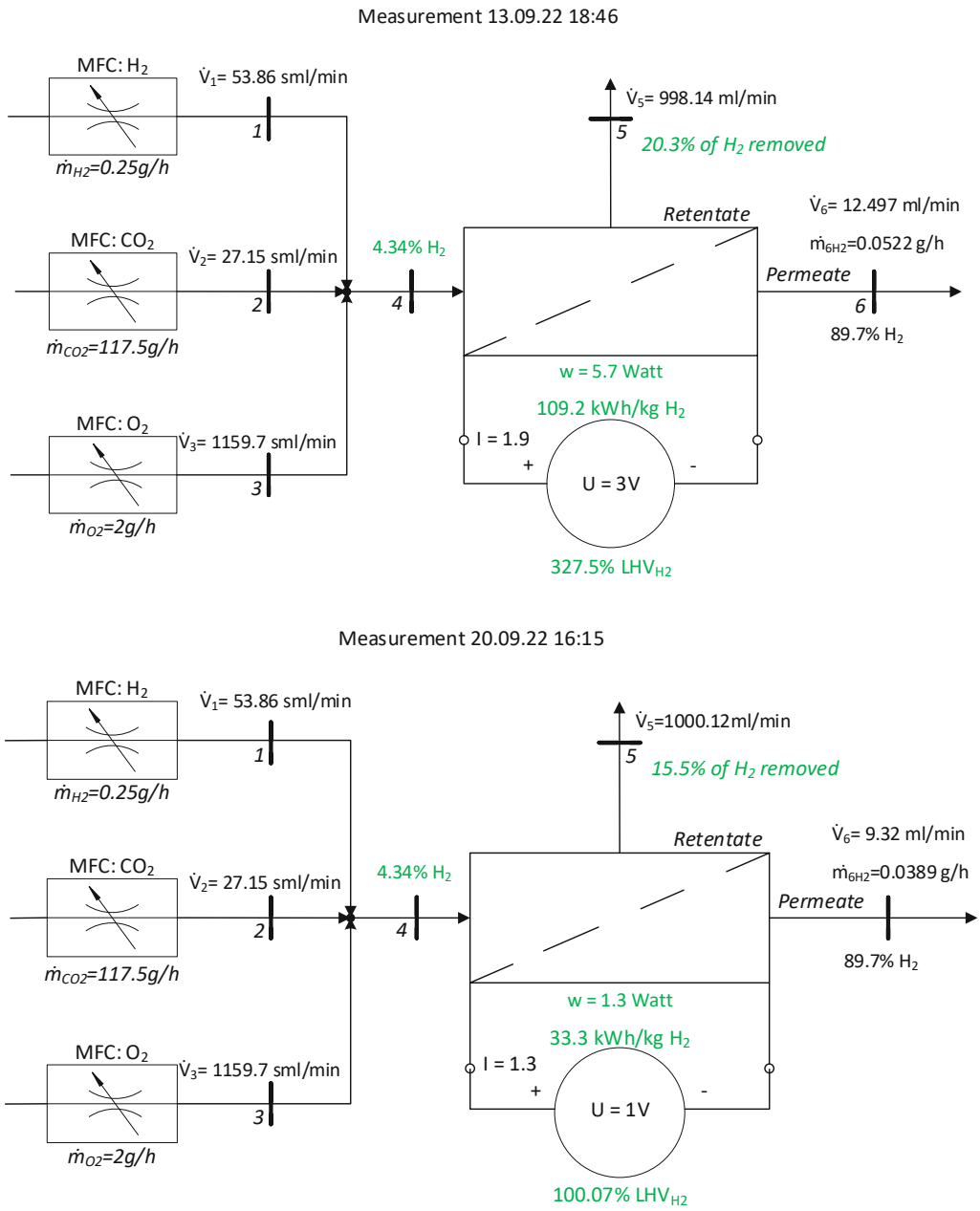

Fig. 24 Results of H_2-O_2-CO_2 separation by EHC

During a measurement at a voltage of 3 V and 5.7 W of power a separation 20.3 % H_2 from the feed was achieved at a power demand of 109.3 kWh/kg H_2, equivalent to 100.07% LHV_{H2} during the separation.

Measurement N2 only 20.09.22 14:16

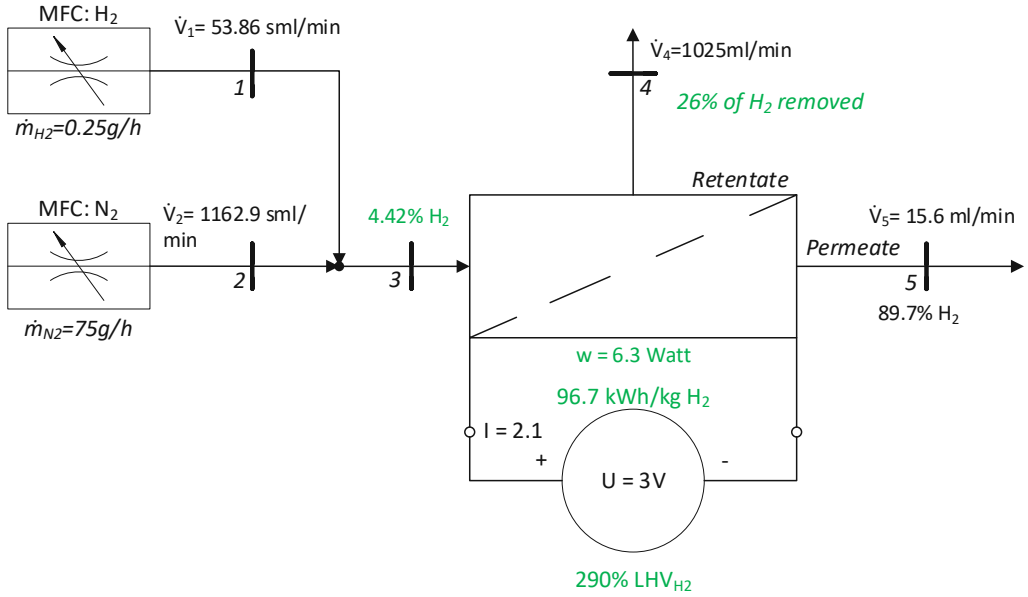

Fig. 25 Results of H_2-N_2 separation by EHC

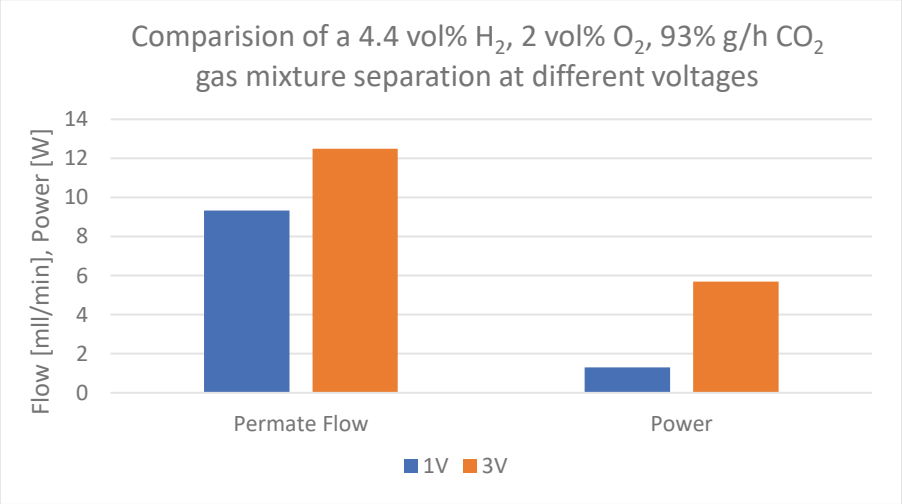

Fig. 26 Comparison of permeate flows at different potentials

The separation at 1 V has a significantly lower power requirement than at 3 V, especially compared to respective permeate flowrates.

6.8. Discussion

The experiments showed that H_2 separation of a trinary H_2-O_2-CO_2 gas mixture is possible.

Since a volumetric CO_2 gas concentration of 108% was measured during the experiment, it was necessary to apply a correction factor to the gas composition calculated from measurements of the feed gas. Oxidation and too high separation potential could be the reason for the high energy consumption. F. Fritsch used voltages of about 0.39 V compared to 1 V (see Tab. 17) and concluded that this still might have been too high. An explanation for the low H_2 purity on the permeate side could be the almost 10 times higher permeability of CO_2 compared to N_2 in NAFION.

In NAFION	Permeability [Barrer] at 1 atm and 35°C
CO_2	2.4
N_2	0.26

Fig. 27 permeabilities in NAFION, source: [183]

The initial spike in the pressure hold test might result from the valve opening in the measurement system, but the result is not conclusive. An improved lab setup with simultaneous analytics of permeate and retentate is necessary for further testing.

Gas mixture	*Voltage*	*Current*	*Power consumption*	*Separation efficiency*	*Ref.*
95 vol% CH_4, 5%H_2	0.393 V	1.79 A	11 kWh/kg	25.3 % H_2	[182]
93,5 vol% CO_2, 4.3 vol% O_2, 2.2 vol% CO_2	1 V	1.3 A	33 kWh/kg 100.07% LHV_{H2}	15.5 % H_2	

Tab. 17 comparison of results of EHC experiments

At first glance, a separation effort of 100.07% LHV_{H2} could indicate that no actual H_2 separation occurred during the separation but rather electrolysis of the humidity in the feed gas. However, with 1 V the potential is too low for water splitting, which requires 1.23 V at least. Therefore, the separated hydrogen should be from the feed gas stream.

7. Scale-up and cost analysis

7.1. The Comparison with 1 MW

The scaled up PhotoSome System should provide a comparable H_2 output to a 1 MW electrolyzer to allow for a tangible comparison. Based on an 80 % efficiency, this amounts to 483.36 kg of H_2 per 24h.

7.2. Method

Two models have been designed. One based on a gas separation based on gas permeation and PSA (PSA Concept) and one based on a hypothetical commercialized electrochemical separator (EHC Concept).

The PSA concept consists of a 2-stage H_2 gas permeation separation system. The EHC concept instead of a hypothetical fully developed EHC.

For both concepts PSA and EHC a model was designed in Microsoft® Excel. Each model consists of 4 linked excel files, one for unit operations concerning photo reactor, one for unit operations concerning the production of PhotoSomes and one for unit operation of the gas separation and one for the cost analysis. PHOTOSOME PRODUCTION, PHOTOREACTOR and GASSEPARATION include models and estimations for all unit operations. GASSEPARATION also includes an overview of gas flows, the gas separation UP, pumps, compressors and heat exchangers. PHOTOSOME _COST is a cost estimation based on the structured method for all UP: The sheets are interconnected to allow for iterative calculation of all unit operations to close the loops' mass balances and compensate gas losses of the gas separation process. The interaction of the excel sheets and excel files is shown in Fig. 30 PhotoSome Calculation Model

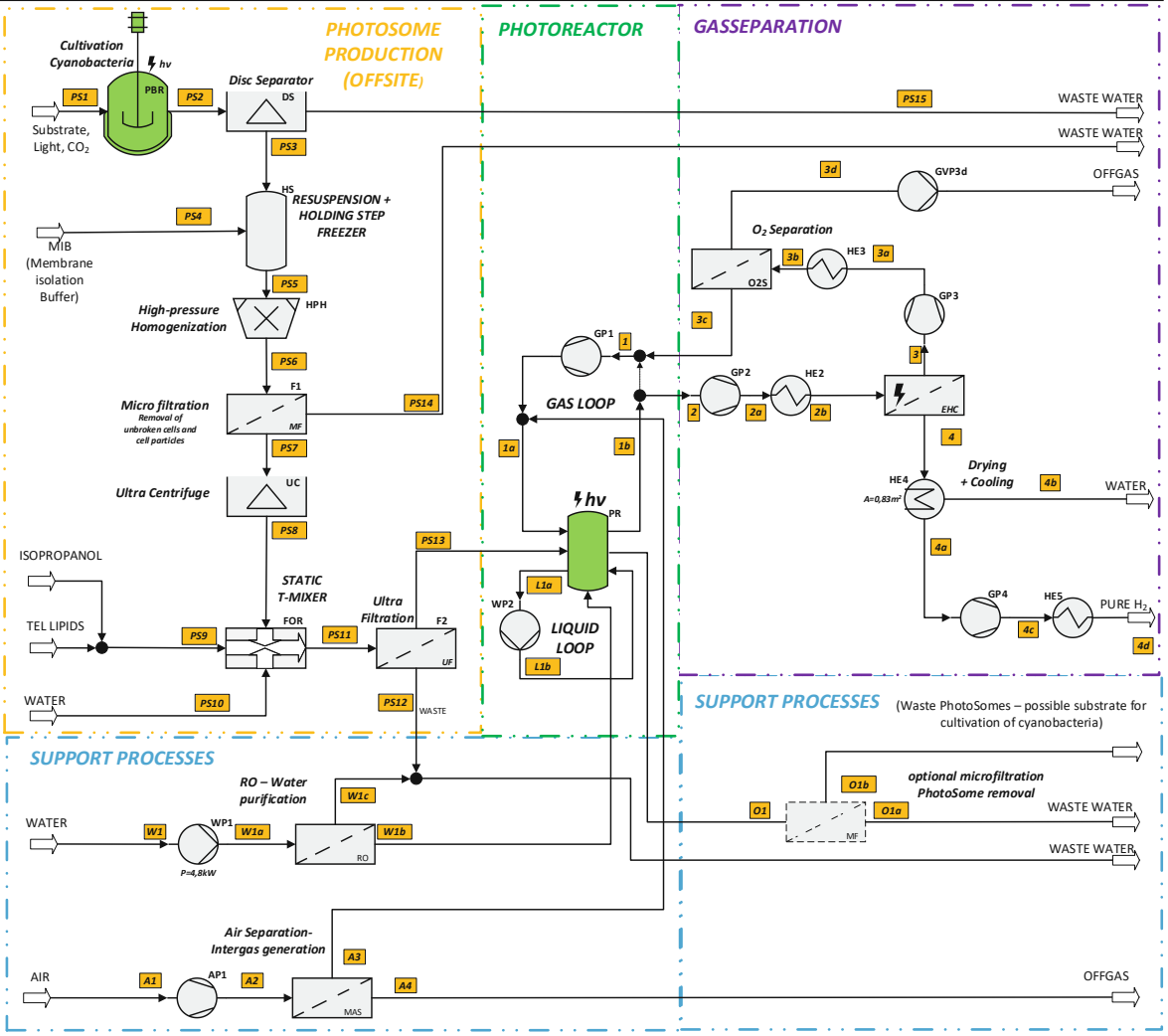

Fig. 28 EHC - FLOW CHART

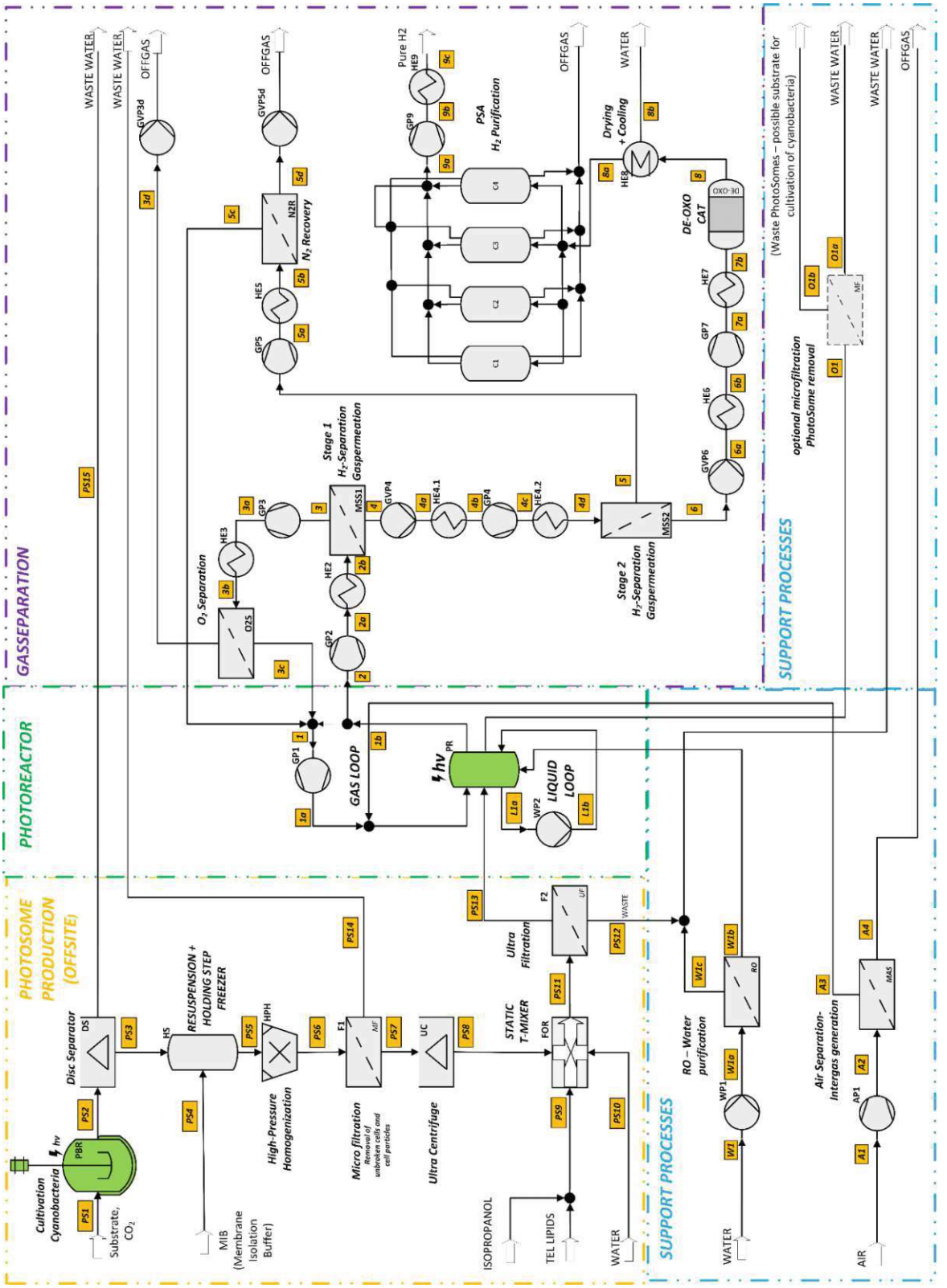

Fig. 29 PhotoSome PSA - FLOW CHART

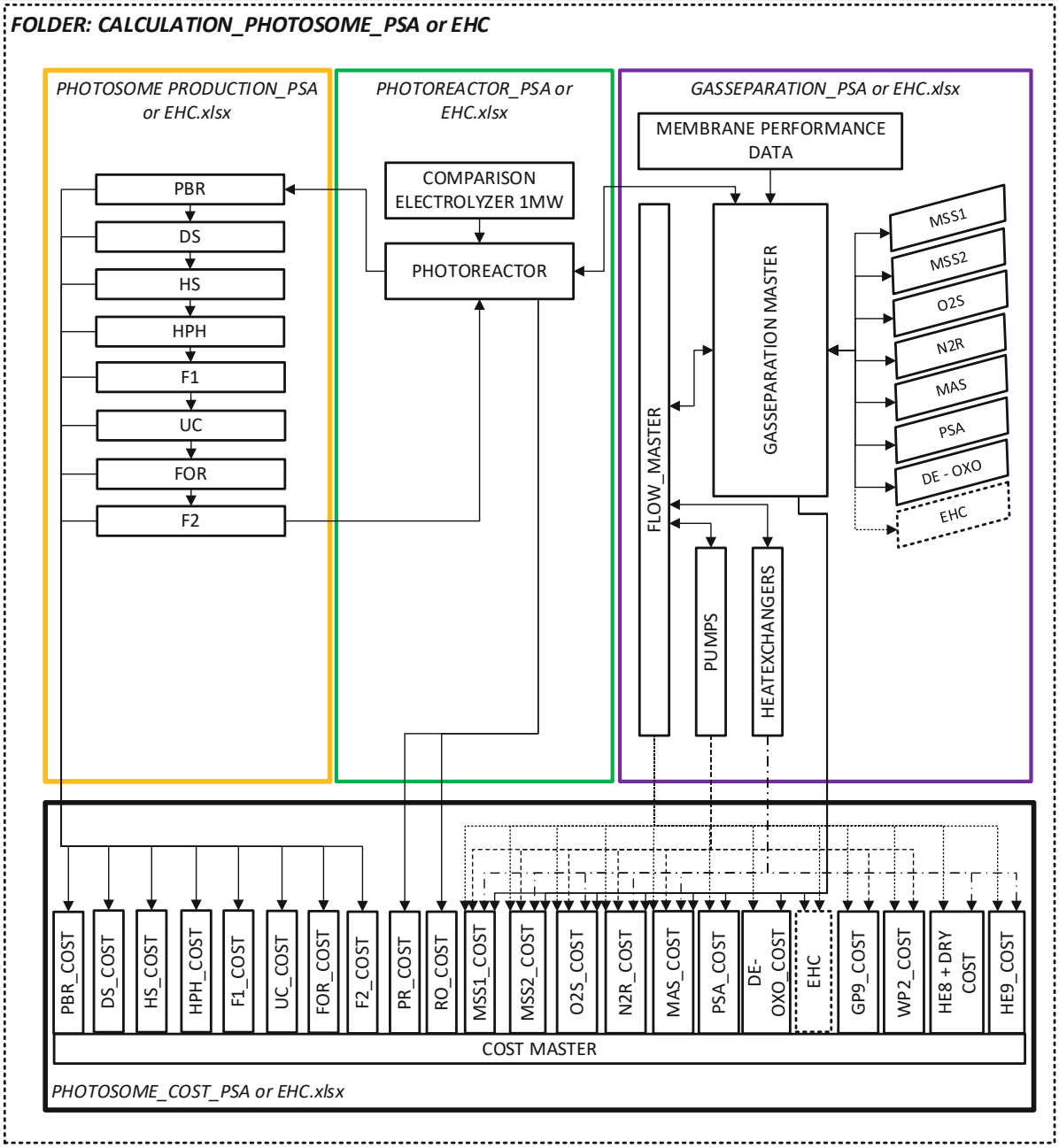

Fig. 30 PhotoSome Calculation Model – Information flow

7.3. The Cost analysis

The cost analysis was based on the structured method. Melin et al.[184, p. 494] provides the following template Tab. 19 for cost estimations for gas permeation from 2006-2023. The cost factors were adjusted to account for inflation by *Verbraucherpreisindex 2005* by Statistik Austria[185], as the more appropriate *Chemical Engineering Plant Cost Index (CEPCI)* was unavailable. For all other unit operations, the same cost template was used. If no cost functions were available in literature, components costs or the cost of materials were used for main component cost factors H_i. The support positions N1 -N12 for all other unit operations were based on their own assumptions and adjusted for each unit operation individually. The number of workers was adjusted to yearly working hours and to the perceived personnel intensity of each unit operation. All annual costs were added in the COST MASTER sheet and presented as cost/kgH_2. The cost factors f_1, f_2, f_3, q, z, KD are unchanged for all unit operations.

The following cost parameter applied to all cost calculation.

GENERAL COST PARAMETERS			
PARAMETER	VALUE	UNIT	INFO
Yearly operating hours:	4000	h	half day operation
Cost of electricity	0.18	€/kWh	Industrial power cost, Austria
Personnel cost	60240	€/yr	
Interest rate 7%	7	%	
Depreciation period 20a	20	yr	because of half day operation
Net dept service 9.44%	9.44	%	

Tab. 18 general cost parameters

The cost functions for gas permeation unit operation (MSS1, MSS2, O2S, N2R, MAS) are shown in Tab. 19. The cost for compressors/vacuum pumps and heat exchangers for each unit operation are already included. If a heat exchanger or pump is not connected to a gas permeation operation, the same functions were used for individual calculations of pumps, vacuum pumps, compressors and heat exchangers. All other cost considerations are described with the respective unit operation below.

COST GAS PERMEATION			
	CALCULATION ACCORDING TO:	Melin und Rautenbach, „Gaspermeation".P494	
	Increase Costbase 2006 to 2023:		1,506
MAIN PARAMETERS			
A_{MEM}		m^2	
V_{FEED}		m_N^3/h	
P_{COMP}		kW	
Membrane cost	55	€/m^2	
MAIN COMPONENTS			
ABR:		Generic Formular	
H1	Membrane modules	82,83	€/m2 Cost Base 2023
H2	Filter, Dryers, Heat exchangers	1,506*60*V_2^0,7433€ mit V_2 in m_N^3/h	Cost Base 2023
H3	Compressors and Pumps	1,506* 1130*$P_{KOMP}^{0,7312}$ € mit P_{KOMP} in KW	Cost Base 2023
SUPPORT POSITIONS			
ABR:		Factor %	% of
N1	Assembly	5	H2+H3
N2	Piping	12	H2+H3
N3	Assembly of piping	50	N2
N4	Isolation and paint	8	H2+H3
N5	Electrical support material	5	H2+H3
N6	Assembly electrical support material	55	N5
N7	Indication and Control I&C	18	H2+H3
N8	Support Material I&C	20	N7
N9	Assembly I& C	45	N7
N10	Building and Support Structures	10	H2+H3
N11	Additionall construction costs	8	H2+H3
N12	Planing and handling costs	10	D
D	Direct system costs	H1+H2*H3+ΣNi=1-11	
IK	Investment costs	D+N12	
	OPEX		
t_B	Yearly operating hours	4000h/a	Half DAY OP:
Z_M	Lifetime of modules	10a	
K_S	Cost of electrical power	0,18 €/kWh	:Price 2023
K_P	Personnel cost	60240€/a	
n_A	Number of workers	0,152	
	Cost factors		
f_1	Maintenance of system	3%	
f_2	Maintenance of building/structure	1%	
f_3	Insurance and administration	0,50%	
q	Interest rate	7%, q=1,07	
z	Depreciation period	20	
KD	Net debt service	9,44% , KD=q^z(q-1)/(q^z-1)	
	Annual costs		
B1	Modul replacement	10a	
B2	Electrical power	t_B*K_S*P_{COMP}*1,01	
B3	Personnel	nA*Kp	
	MAINTAINANCE		
B4	for SYSTEM	f1 of (D-N10)	
B5	for Building and Support Structures	f2 of (H1+H2+H3)	
B6	for Insurance and Administration	f3 of (H1+H2+H3)	
B7	Depreciation	KD of IK	
BK	Operating costs	ΣBi i=1-7	
OPEX	OPEX	ΣBi i=1-3	
CAPEX	CAPEX	ΣBi i=4-7	

Tab. 19 COST TEMPLATE for GASPERMEATION

7.4. Main constraints and simplifications

Besides the required output stream of 483.36 kg of H_2 per 24h over 365 days at PEM-fuel cell qualities of H_2 *ISO 14687* further constraints were given. The system was envisioned as a decentralized, local H_2 production system, possibly capable of feeding H_2 into the local natural gas grid.

To avoid all the complex engineering questions regarding the intermittence problem, inherent to all solar technologies, constant 12 hours of steady H_2 production over the whole year at an average yearly solar potential of 1250 kWh/(m^2 · yr.).

The PhotoSomes performance had to be specified without lab data to back up the performance. The stability was assumed to be 6 months and the efficiency 7% STH as described in *"4.5 Stability and performance of PhotoSomes".*

To estimate the formulation of PhotoSomes, the required biomass was estimated at 50% of the required mass of PhotoSomes lipids. No buffers or surfactants are considered in the estimation.

The gas separation is constrained by the flammability limits and limiting oxygen concentration. All gas streams were assumed to be dry except for stream 8 after the DE-OXO catalyst.

Further assumptions for each unit operation are explained on the following pages.

7.5. The Photo Reactor

7.5.1. Comparison of a PhotoReactor

The comparison is based on a 1 MW electrolyzer with 80% conversion efficiency with 24 h of operation. With an ΔH_{H2} = 286 kJ/mol from water, disregarding any system work to expand the formed gas. This amounts to 483.36 kg_{H2}/day.

$$m_{H2,ele} = \frac{P_{ele} * t_{ele} * \eta_{ele} * M_{H2} * 3600}{\Delta H_{H2}}, \qquad (Eq\ 7.0)$$

7.5.2. Photo reactor

The PhotoReactor is designed for PhotoSomes with an STH of 7% conversion efficiency and 6 months of activity (= effective lifetime), for 12 h of daily operation to account for the daily solar cycle and based on an average yearly solar irradiation of 1250 kWh/(m^2 * yr)

The required amount of PhotoSomes was calculated on the assumption that based on a hypothetical model of lipid layers the entire photo reactor surface should be covered by one PhotoSome. Based on 150 nm lipid diameter and a TEL lipid concentration of 5% - the rest are conventional lipids, a particle concentration of $2.4*10^{12}$ mL^{-1} and a lipid concentration of 2 g/L in the liposome mixture. This requires at least 20 layers of liposomes. The final photoreactor size and the required amount of liposomes is slightly different for both concepts as it compensates for H_2 losses of the gas separation. Also, the daily amount of water consumption is slightly different. The water consumption is solely based on water splitting, any water evaporation hasn't been taken into account.

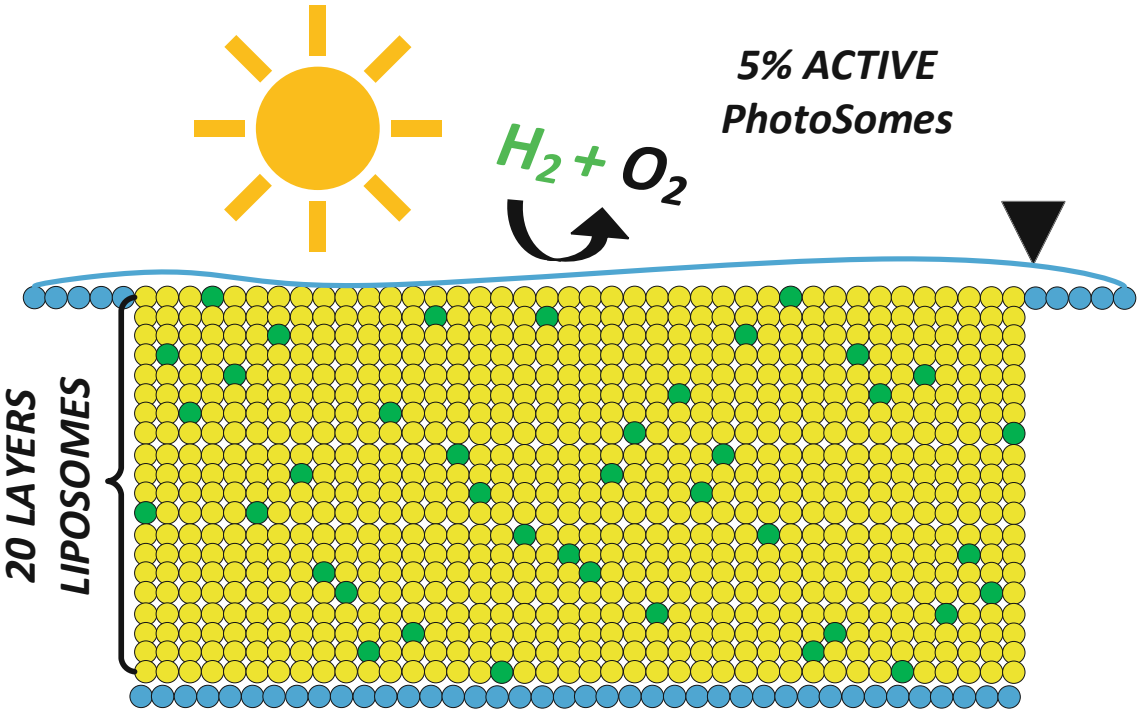

Fig. 31 Model for PhotoSomes distribution in photo reactor – green are photo active TEL PhotoSomes, yellow conventional phospholipids

PARAMETERS PR				
INPUT FACTOR	**VALUE**	**UNIT**	**Info**	**SOURCE**
t_{PR}	12	h	Hours of daily operation	Assumption
STH_{PS}	7%		Solar to H_2 efficiency PhotoSomes	Assumption
$P_{SOLAR,AUT,MEAN,YR}$		kWh/ (m^2 * yr)	Mean yearly solar potential for Austria	[149]
$t_{STB,PS}$	0.5	yr	Stability of PhotoSomes	Assumption
$-\Delta H_{H2O}$	286	kJ/mol	Energy consumption water splitting	NIST CHEMISTRY WEBBOOK
d_{PS}	150	nm	Diameter PhotoSome	SUPPLYER
$c_{n,LS}$	2.4E+12	mL^{-1}	Particle concentration of liposome mixture	SUPPLYER
f_{TEL}	5%		share of tetrahedral lipids	SUPPLYER
c_{LS}	20	g/L	Lipid concentration in c liposome sample	SUPPLYER

Tab. 20 Parameters PR

7.5.3. The design of the photo reactor panels and cost

The photoreactor is designed as a flat–plate reactor with panels of 2x1 m in size. The panel is slightly tilted at 3° to allow the gas to collect on top and be expelled into the gas collection tube and to prevent the accumulation of any particles in case of contamination. The thickness of the reactor is 30mm and is almost entirely filled with the aqueous phase. It is constructed of 0.5 mm 1.4404 stainless steel sheets. 1.4404 is a stainless steel with 10% of nickel to withstand H_2 embrittlement and a cost-effective option for H_2 applications, also it is available at 0.5mm thickness. A 3.2 mm thick purpose-build glass panel, for solar collectors and solar cells, seals the front of the photoreactor. This glass panel offers high transmissibility and rough surface texture to reduce reflection to the surrounding area. The photo reactor panel is also connected to 2 tubes with the aqueous loop to

allow for the distribution of the PhotoSomes, flushing of the system and replacement of water. These panels are connected to a 300 mm gas pipe. To guarantee a uniform distribution of the PhotoSomes in the reactor panel, a split stream of the replacement N_2 can be bubblelized into the reactor and in tandem with the rising gas bubbles created by water splitting should provide sufficient turbulation and movement in the reactor. The panels are placed in a square configuration of about 300 m to 300 m. 2 rows of panels are connected on one of 72, about 600 m long gas pipes that in turn are again connected to 2 large main collector pipes that finally connect to the gas loop. This configuration helps to reduce gas speed and subsequent pressure drops and compressor power consumption. A pressure drop of 0.1 bar is estimated. The panels are supported by 2.4 m of 30 x30x2 mm tubing per panel.

Cost 1.4044 according to feedback from a supplier amounts to 5.50 €/kg and the glass panel is estimated at 8 € per m^2 according to an industry contact. The tubing cost for the subframe was available online at 9 € per m. Welding is considered at 8 € per meter. The land cost is estimated at 2.5 €/m^2.

A rudimentary FEM analysis of the sheet-metal half shell with 0.5 mm thickness and without the glass panel was undertaken to estimate the required sheet metal thickness as a glued connection would need further research. Based on a static load of 300 N/m^2 from the water column and a snow load, according to the *ÖNORM B 1991 – 1-3:2022 05 15* of 1 kN/m^2 the max stresses of 84 N/mm^2 don't exceed the yield stress of >255 N/mm^2. A thinner sheet metal size is not available.

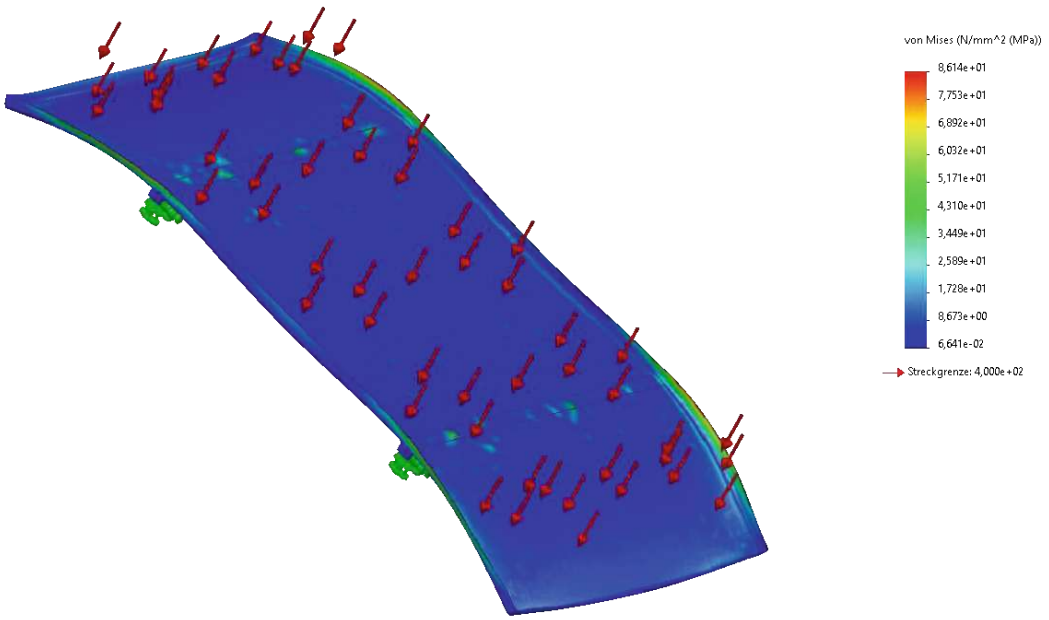

Fig. 32 FEM analysis of the PhotoSome photoreactor metal half-shell

COST PARMETERS PHOTOREACTOR					
PARAMETER	**VALUE**	**UNIT**	**PARAMETER**	**INFO**	**SOURCE**
K_{LAND}	2.5	€/m²	cost of land	Cheapest agricultural land price in Austria: Großmürbisch at 1.05€/m²	[186]
A_{panel}	2.00	m²	panel size	Assumption	
L_{welds}	120	mm	length welds per panel	Assumption	
m_{PANEL}	8.6	kg	weight of a panel	0.5mm sheet metal thickness	
K_{GLASS}	8 €	€/m²	cost of glass panel	Glass Supplier (confidential) 3.2mm	
$K_{1.4404}$	5.5 €	€/kg	Price 1.4404 - SHEET METAL 0,5mm	supplier Info	
K_{WELD}	8	€/m	cost of welds		[187]
K_{TUBING}	9	€/m	cost of tubing - subframe	cost tubing 30x30x2	
$l_{SUBFRAME}$	2.4	m	length subframe per panel	Assumption	
m_{water}	4.65E+03	kg/day	water consumption water splitting	daily amount of water	
t_{PR}	365	days		operation time	
K_{WATER}	1.83	€/m³	cost water	Reference upper Austria	[188]

Tab. 21 Cost parameters PR

7.6. The Production of PhotoSomes

The production of PhotoSomes was designed around the presumption that the isolation of the membrane particles and the formulation of the PhotoSomes requires 50% of the weight of lipids as initial biomatter. As the PhotoSomes need to be replaced every 6 months, the production was designed to this time frame. The cultivation of *synechoccus elongatus* is a continuous process with a harvest step after each cultivation of 2 weeks followed by a freezing of the biomatter. All other downstream steps are designed for a single downstream and formulation batch every 6 months.

7.6.1. Cultivation of cyanobacteria PBR

The cultivation of UTEX 2973 *synechoccus elongatus* was designed on a biomass yield of 0.65 $g_{DW}/_{L}$ over 14 days and for 12 batches over 6 months.

$$V_{PBR} = \frac{m_{cyano}}{12 * Yield_{cyano}}, \qquad (Eq\ 7.1)$$

The cost calculation was designed on the basis of a 5000 €/m³ [158] a power requirement of 2 kW/m³[189] for tubular bio reactors. Substrate cost is assumed at 0 € as it is a waste stream.

7.6.2. Harvest of cyanobacteria DS

The harvest of cyanobacteria was designed to a harvest time of 12 hours. This includes the removal of biomass and separation time. A 75% biomass separation efficiency was assumed. The cost analysis is based on the system price for an Alfa Laval Alfie 500 DS of 11000 € with a separation flow of 500 L/h.

7.6.3. Resuspension and holding step HS.

The resuspension of the separated biomass was designed for a max. biomass concentration of 200 g/L in the HPH feed.

The cost analysis for this unit operation is based on a commercial freezer *LIEBHERR Gefriergerät GGPv 1470 ProfiLine Gefriergerät* available online for 5800 € and 3333 kWh/yr energy consumption[190].

7.6.4. High Pressure Homogenization

The high-pressure homogenization is designed for 3 runs at 1200 bar. Based on the High-Pressure Homogenizer DeBEE 2000-20-120 with a max. flowrate of 2 L/min. The High-Pressure Homogenizer DeBEE 2000-20-120 costs 175 000 $ with a power consumption of 2 kW.

7.6.5. Microfiltration F1

This microfiltration removes unbroken cells and larger cell debris prior to centrifugation. First experiments for cell disruption showed particles in the range of 150 nm. However, lacking experimental data for this unit operation, a membrane an average flux of 10% of a pure water flux of 500 L/h*m^2 was chosen. The next assumption was a permeate volumetric stream of 25% of the feed stream. The cost estimation is based on a Sani Lab Vibro-Lab3500 Membrane system with 0.2 m^2 Membrane for 11691 €.

7.6.6. Ultra Centrifugation

The Ultra Centrifugation is the final separation step. Based on 1.5L of batch volume, 15 min of centrifugation time and 5 minutes of setup time of each 1.5L run, several runs will be required.

Cost analysis is based on the price of *a Thermo Scientific™ Sorvall WX 80+ Ultracentrifuge* of 74105€

7.6.7. Formulation with a T-shape static mixer

The formulation process requires a ratio of aqueous to organic phase flow of 2. The organic phase is produced by dissolving the dried TEL lipids into isopropanol at a concentration of 20 g/L. Then, the organic phase is injected into the aqueous stream via a simple T-shaped mixer at the required ratio. As the cost of this custom mixing element is not available, the cost was estimated at 3000€ based on supplier feedback for inflow static mixers for a similar fluid and flow. The pressure drops and consequently, the system's power consumption is not considered. The cost of the crude lipids was estimated at 137 € per g and the cost of isopropanol in technical quality at 2 €/L.

7.6.8. Ultrafiltration PhotoSomes F2

As the lipids are provided the supplier in an isopropanol solution and are highly diluted after formulation. This separation is again designed to 50 L/(h*m^2) 10% of a pure water flow of a MicroNadir® UP030 Ultra filtration membrane. The cost of the system was extrapolated based on membrane surface from a pilot scale 40 m^2 Sani Lab Pilot Vibro I membrane filtration system costing 143600 €.

7.7. Gas Separation

The gas separation was designed for high H_2 capture. The process is constrained by the flammability limits and limiting oxygen concentrations. The initial feed of the photo reactor is a 4 vol% H_2, 2 vol% O_2 and 94 vol% N_2. By closing the gas loop, the feedback streams increase the O_2 concentration and changes the gas composition. In the case of the PSA system the O_2 concentration in the loop is limited by the separation efficiency of MSS1. To avoid exceeding the LOC in stream 4 the O_2 concentration in the loop is limited and therefore also the H_2 concentration.

7.7.1. The structure of the gas separation

The excel *file GASSEPARTION_PSA* or *EHC.xlsx* consists of several sheets as seen in *Fig. 30 PhotoSome Calculation Model – Information flow*. The sheet GASSEPARATION_MASTER connects all unit operations and flow and allows for iteration to close the mass balances. After each iteration a scale-up factor was calculated to meet the required H_2 output and a new gas composition in the loop. To

start the next iterations the scale-up factor of the previous iteration is multiplied to the other the prior scale-up factors and the new gas loop composition is copied into the feed stream 2. This avoids issues with circular reference. 4 iterations are sufficient to close the balances.

7.7.2. The Membrane Model

The membrane H_2 separation was modeled after a paper of Alsayegh et al.[150].

For this study, a simplified short cut model was applied with the following assumptions.

- The system is in steady state.
- Free flow on the permeate side.
- Solution diffusion mechanism for the hollow fiber model.
- No temperature and pressure drop along and the membrane.
- No interaction between the components (flux coupling).
- Constant selectivity and permeability along the membrane .

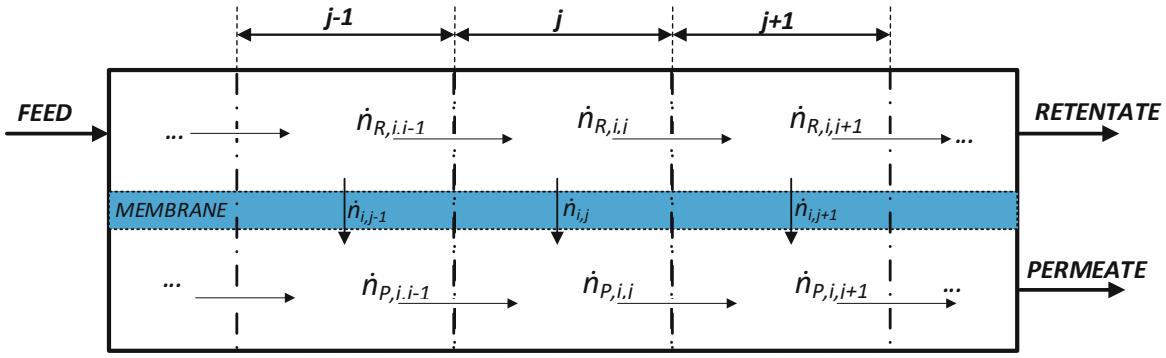

Fig. 33 Membrane Model

It splits the membrane into 10 segments with equal membrane area. The free flow conditions allows to set the permeate pressure to 0 and assume a constant pressure difference between retentate and permeate side. The retentate flow between 2 elements $\dot{n}_{R,i,j}$ is reduced by the transmembrane flux $\dot{n}_{i,j}$ of each component of the prior element. The permeate flow $\dot{n}_{P,i,j}$ is the sum of the transmembrane flows of all prior elements.

Transmembrane flux:

$$\dot{n}_{i,j} = Q_i * \left(x_{i,j} * p_f - y_{i,j} * p_p\right) * A_{mebrane,ele}, \quad (Eq\ 7.2)$$

Retentate and permeate flows:

$$\dot{n}_{R,i,j} = \dot{n}_{R,i,j-1} - \dot{n}_{i,j-1}, \quad (Eq\ 7.3)$$

$$\dot{n}_{P,i,j} = \dot{n}_{R,i,j-1} + \dot{n}_{i,j-1}, \quad (Eq\ 7.4)$$

Composition of permeate and retentate:

$$x_{i,j} = \frac{\dot{n}_{R,i,j}}{\sum_i \dot{n}_{R,i,j}}, \quad (Eq\ 7.5)$$

$$x_{i,j} = \frac{\dot{n}_{P,i,j}}{\sum_i \dot{n}_{P,i,j}}, \quad (Eq\ 7.6)$$

7.7.3. Membranes

The separation MSS1 and MSS2 were equipped with a UBE® Membrane – similar to Alsayeghs study. The O_2/N_2 separations of O2S, N2R and MAS are equipped with the higher performing generic PI membrane. The following formulas calculated the permeance and selectivity.

$$[GPU] = 3.35 * 10^{-10} \frac{mol}{m^2 * s * Pa}, \quad (Eq\ 7.7)$$

$$S_{i\_j} = \frac{P_i}{P_J}, \quad (Eq\ 7.8)$$

MEMBRANE PERFORMANCE DATA						
	UBE®			generic PI		
	Permeance	Permeance	Selectivity	Permeance	Permeance	Selectivity
Component:	[GPU]	[mol/(m².s.Pa)]	Q_{H2}/Q_i	[GPU]	[mol/(m².s.Pa)]	Qo_2/Q_i
H_2	140	4.69E-08	-	N.A.	N.A.	N.A.
O_2	8.4	2.81E-09	16.7	65	2.18E-08	-
N_2	1.7	5.70E-10	4.9	10.32	3.46E-09	6.3
Source:	[150]			[175]		

Fig. 34 Membrane performance data

The cost analysis for the gas permeation was based on the structured method. Melin et al.[184, p. 494] provides the template shown in Tab. *19 COST TEMPLATE for GASPERMEATION*. To account for cost estimations for gas permeation from 2006 - 2023. The cost factors were adjusted to account for inflation by *Verbraucherpreisindex 2005* by Statistik Austria [185]. The membrane cost of 55 €/m² was sourced from the paper of Alsayegh et al. [150].

7.7.4. PSA

The pressure swing adsorption was designed with the "Massenbilanz" short-cut method from the Book *"Adsorptionstechnik by Dieter Bathen, Marc Breitbach,"* [191, p. 236] for 5A zeolite adsorbents. 5A shows superior performance to carbon molecular sieves and all necessary parameters for design were available by a study of purification of waste H_2 to fuel cell grade. [179]

The initial assumption was for a 4-column design to allow continuous operation with 900s of adsorption time. The adsorption occurs at $4 \cdot 10^5$ Pa, desorption at $1 \cdot 10^5$ Pa. at 293.15 K, by assuming a gas flow velocity in the PSA column and a scale-up safety factor according to *Bathen and Breitenbach* and with the 5A bulk density, it is possible to calculate the adsorber cross-section, adsorbents mass and column dimensions. With the amount of adsorbed H_2, a PSA yield and H_2 loss are calculated with the following formulas.

SCALE-UP PARAMETER PSA					
PARAMETER	VALUE	UNIT	PARAMETER	INFO	SOURCE
$p_{PSA,ad}$	400000	Pa	Pressure PSA adsorption	according to 5A Data	[179]
$p_{PSA,de}$	100000	Pa	Pressure PSA desorption	according to 5A Data	[179]
T_{ad}	293.15	K	Temperature adsorption	according to 5A Data	[179]
t_{ad}	900	s	Adsorption Time	Assumption - 4 column design	
ρ_{5A}	0.66	g/cm^3	Bulk density adsorbents 5A		[192]
$X_{5A,H2}$	0.11	mol/kg_{5A}	H_2 loading of adsorbents 5A at 4 bar, 293.15K		[179]
$X_{5A,N2}$	1.5	mol/kg_{5A}	N_2 loading of adsorbents 5A at 4 bar, 293.15K		[179]
σ_{PSA}	1.2		Scale-Up safety factor	Assumption according to Adsorptionstechnik, Dieter Bathen, Marc Breitbach, S 236	[191]
$v_{\_PSA}$	0.4	m/s	Gas flow velocity in PSA column	Assumption according to Adsorptionstechnik, Dieter Bathen, Marc Breitbach, S 236	[191]

Tab. 22 PARAMETERS PSA

Calculation of column cross section:

$$A_{PSA} = \frac{\dot{V}_{8a}}{v_{PSA}}, \quad (Eq\ 7.9)$$

Required mass adsorbents:

$$m_{5A,column} = \dot{n}_{8a,N2} \cdot t_{ad} \cdot \frac{\sigma_{PSA}}{X_{5A,N2}}, \quad (Eq\ 7.10)$$

Dimensions of one PSA column:

$$h_{PSA} = \frac{m_{5A,column}}{\varrho_{5A} \cdot A_{PSA}}, \quad (Eq\ 7.11)$$

$$d_{PSA} = \sqrt{\frac{A_{PSA} * 4}{\pi}}, \quad (Eq\ 7.12)$$

H_2 losses and PSA yield:

$$m_{H2,ads,column} = m_{H2,loss} = X_{5A,H2} * m_{5A,column}, \quad (Eq\ 7.13)$$

$$m_{9,H2} = m_{8a,H2} - m_{H2,ads,column}, \quad (Eq\ 7.14)$$

$$Y_{H2,PSA} = \frac{m_{9,H2}}{m_{8a,H2}}, \quad (Eq\ 7.15)$$

The cost estimation was based on cost function for cylindrical, rust-free tanks for pressure below 1 MPa form "Handbuch Verfahrenstechnik und Anlagenbau"[193, pp. 848–849] and cost for the Adsorbents 5A.

$$K_{PSA,column} = C_{PSA} * {V_{C,i}}^{a_{PSA}} * n_{PSA} * f_{in,PSA} * r_{\$/€} \quad (Eq\ 7.16)$$

$$K_{5A,column} = C_{5A} * m_{5A,column} \quad (Eq\ 7.17)$$

COST PARAMETER PSA					
PARAMETER	VALUE	UNIT	PARAMETER	INFO	SOURCE
V_{ci}	0.5012	m^3	volume of 4 columns		[193]
n_{PSA}	4		number of columns		
C_{5A}	92	€/kg	cost 5A		[194]
C_{PSA}	9200			Cylindrical Tank, rust-free, < 1 MPa,	[193]
$f_{in,PSA}$	2.56		[$] cost base 1986-2023	inflation index	[195]
$r_{\$/€}$	0.86		conversion $/€, 20.07.23		
a_{PSA}	0.72				[193]

Tab. 23 COST PARAMETERS PSA

7.7.5. Pumps and compressors

The gas compressors and vacuum pumps are modeled with the same equations. To simplify the model one stage systems without interstage cooling and isentropic and adiabatic compression are used to calculate the outlet temperature and power requirement for these unit operations.

$$T_{out} = T_{in} * \left(\frac{p_{out}}{p_{in}}\right)^{\left(\frac{\kappa-1}{\kappa}\right)}, \quad (Eq\ 7.18)$$

$$\eta_i = \frac{T_{out} - T_{in}}{T_{real} - T_{in}}, \quad (Eq\ 7.19)$$

$$T_{real} = \frac{T_{out} - T_{in} + T_{in} * \eta_i}{\eta_i}, \quad (Eq\ 7.20)$$

To account for the different compositions of gas mixtures in the process, the heat capacity was calculated by:

$$c_{p,gasmixture} = \sum_{i=0}^{I} x_i * c_{p,i}, \quad (Eq\ 7.21)$$

$$P_{comp\ or\ vac} = \dot{n} * c_{p,gasmixture} * (T_{real} - T_{in}), \quad (Eq\ 7.22)$$

The water/fluid pumps are calculated with:

$$P_{pump} = \dot{m} * (p_{OUT} - p_{IN}) * \eta_i, \quad (Eq\ 7.23)$$

SCALE-UP PARAMETERS PUMPS				
PARAMETER	VALUE	UNIT	INFO	SOURCE
K	1.4	-	isentropic compression	[150]
$c_{p,H2}$	29	J/(mol*K)	at 333 K	[196]
$c_{p,O2}$	29.59	J/(mol*K)	at 333 K	[196]
$c_{p,N2}$	29.145	J/(mol*K)	at 333 K	[196]
$c_{p,H2O}$	4180	J/(kg*K)	at 333 K	[196]
R_M	8.314	J/(mol*K)	universal gas constant	[150]
η_{comp}	0.8	-	compressors	[150]
η_{vac}	0.5	-	vacuum pumps	[150]
η_{pump}	0.5	-	pumps	[197]

Tab. 24 PARAMETERS COMP, VAC, PUMPS

The cost estimation for the compressor and vacuum pump is based on the formula provided by Melin in *Tab. 19*[184], the cost function for the pump is found in "*Handbuch Verfahrenstechnik und Anlagenbau"*[193, p. 757]. Both have been adjusted for inflation from their respective publication year.

Cost function pump:

$$K_{pump} = 6720 * P_{PUMP}\,[in\ kW]^{0.28} * f_{in}, \qquad (Eq\ 7.24)$$

Cost function compressor and vacuum pump:

$$K_{comp\ or\ vac} = 1130 * P_{comp\ or\ vac}\,[in\ kW]^{0.7433} * f_{in}, \qquad (Eq\ 7.25)$$

7.7.6. Heat exchangers

The compressed gas streams from compressors and vacuum pumps are too hot for the gas permeation process. Also, these streams must be cooled down to reduce the risk of explosion. A water flow with a fixed inlet and outlet temperature in a counter – current design with the gas stream, is used to calculate the required amount of cooling water and heat exchange area.

$$c_{p,gasmixture} = \sum_{i=0}^{I} x_i * c_{p,i}\,, \qquad (Eq\ 7.26)$$

$$\dot{Q}_{cool,HE} = \dot{n} * c_{p,gasmixture} * \left(T_{real,j} - T_{in,i}\right), \qquad (Eq\ 7.27)$$

$$\dot{Q}_{cool} = \dot{m}_{water} * c_{p,water} * \left(T_{water,out} - T_{water,in}\right), \qquad (Eq\ 7.28)$$

$$\dot{Q}_{cool} = \alpha * A_{HEATEXCHANGER} * \Delta T_{lm}, \qquad (Eq\ 7.29)$$

The logarithmic mean temperature is calculated by:

$$\Delta T_{lm} = \frac{\Delta T_A - \Delta T_B}{\ln\left(\frac{\Delta T_A}{\Delta T_B}\right)}, \quad (Eq\ 7.30)$$

$$\Delta T_A = T_{in,gas} - T_{out_{water}}, \quad (Eq\ 7.31)$$

$$\Delta T_B = T_{out,gas} - T_{in\_water} \quad (Eq\ 7.32)$$

The required cooling water flow and heat exchanger area are then calculated by:

$$\dot{m}_{water} = \frac{\dot{Q}_{cool}}{c_{p,water} * \left(T_{water,out} - T_{water,in}\right)}, \qquad (Eq\ 7.33)$$

$$A_{HEATEXCHANGER} = \frac{\dot{Q}_{cool}}{\alpha * \Delta T_{lm}}, \qquad (Eq\ 7.34)$$

The same set of equation was used to calculate the heat exchanger and dryer HE8:

HEAT EXCHANGERS + DRYER				
PARAMETER	VALUE	UNIT	INFO	SOURCE
$c_{p,H2}$	29	(J/mol*K)	at 333 K	[196]
$c_{p,O2}$	29.59	(J/mol*K)	at 333 K	[196]
$c_{p,N2}$	29.145	(J/mol*K)	at 333 K	[196]
$c_{p,H2O}$	4180	(J/kg*K)	at 333 K	[196]
$\alpha_{high\ pressure}$	220	[W/(m² · K)]	heat transfer coefficient, at 4 bar; after compressor	[150]
α_{vac}	110	[W/(m² · K)]	heat transfer coefficient, at 1 bar, after vacuum pump	[150]

Tab. 25 PARAMETERS HEATEXCHANGERS

The cost function heat exchanger (including filters, dryers etc.) provided by Melin in *Tab. 19* [184]. Was also applied for stand-alone dryer and heat exchangers (ones that are not included in a cost analysis of a gas permeation unit operation). The inflation 2007-2023 was consider by a factor 1.506.

$$K_{HE} = 60 * \dot{V}_{FEED} \left[in \frac{{m_n}^3}{h} \right]^{0.7433} * f_{in}, \qquad (Eq\ 7.35)$$

7.7.7. DE-OXO - Catalyst

Given the lack of data and research, scaling up the DE-OXO catalyst was challenging. Based on the presumption of a 100% conversion rate of oxygen and no condensation on the catalyst surface were assumed.

This exothermic reaction produces steam and heats up the outlet gas stream of the catalyst. It's temperature increase is calculated by.

$$\Delta T_{DEOXO,OUT} = \frac{\Delta H_{H2O} * \dot{n}_{O2,in}}{c_{p,gasmixture} * \dot{n}_{Total}}, \qquad (Eq\ 7.36)$$

The amount of steam is calculated by:

$$\dot{n}_{H2O,out} = \frac{\dot{n}_{O2,in}}{2}, \qquad (Eq\ 7.37)$$

The cost comparison has proven even more difficult. Without data for residence time, catalyst loading and exact catalyst composition, design or requesting a quote for a custom ceramic honeycomb catalyst was not possible. Compared to an oxidation catalyst of a commercial vehicle the flow through the DE – OXO catalyst is about 40%. A quick online search showed that these commercial vehicle catalysts are priced at about 3000€. To account for the added cost of a one-off custom catalyst, an estimated price of 30000€ was selected.

7.7.8. EHC

The scale-up of the EHC system faced a similar issue as the DE-OXO system. Even though first "proof – of concept" experiments have provided some data – it's still far from the performance of a hypothetical fully optimized and commercialized system.

Previous septation project have shown that industry accepts an energy consumption of 10% LHV for H_2 separation technology. A commercialized system would need to reach this efficiency. Therefore, the EHC – unit operation was designed to a 80% capture rate at 10% LHV H_2 energy consumption. As a multi-stack system will show a pressure drop on the retentate side, a pressure drop of 2 bar was estimated. Without an actual stack design, a component-based cost analysis wasn't practical. As the EHC resembles more a PEM fuel-cell than a PEM electrolyze and the H_2 output is similar, a 1 MW fuel cell system, for 2 540 000$, was used as main cost parameter.

7.8. RESULTS

The results of the scale-up and cost analysis of the PSA and EHC – concept are presented in the following flowcharts.

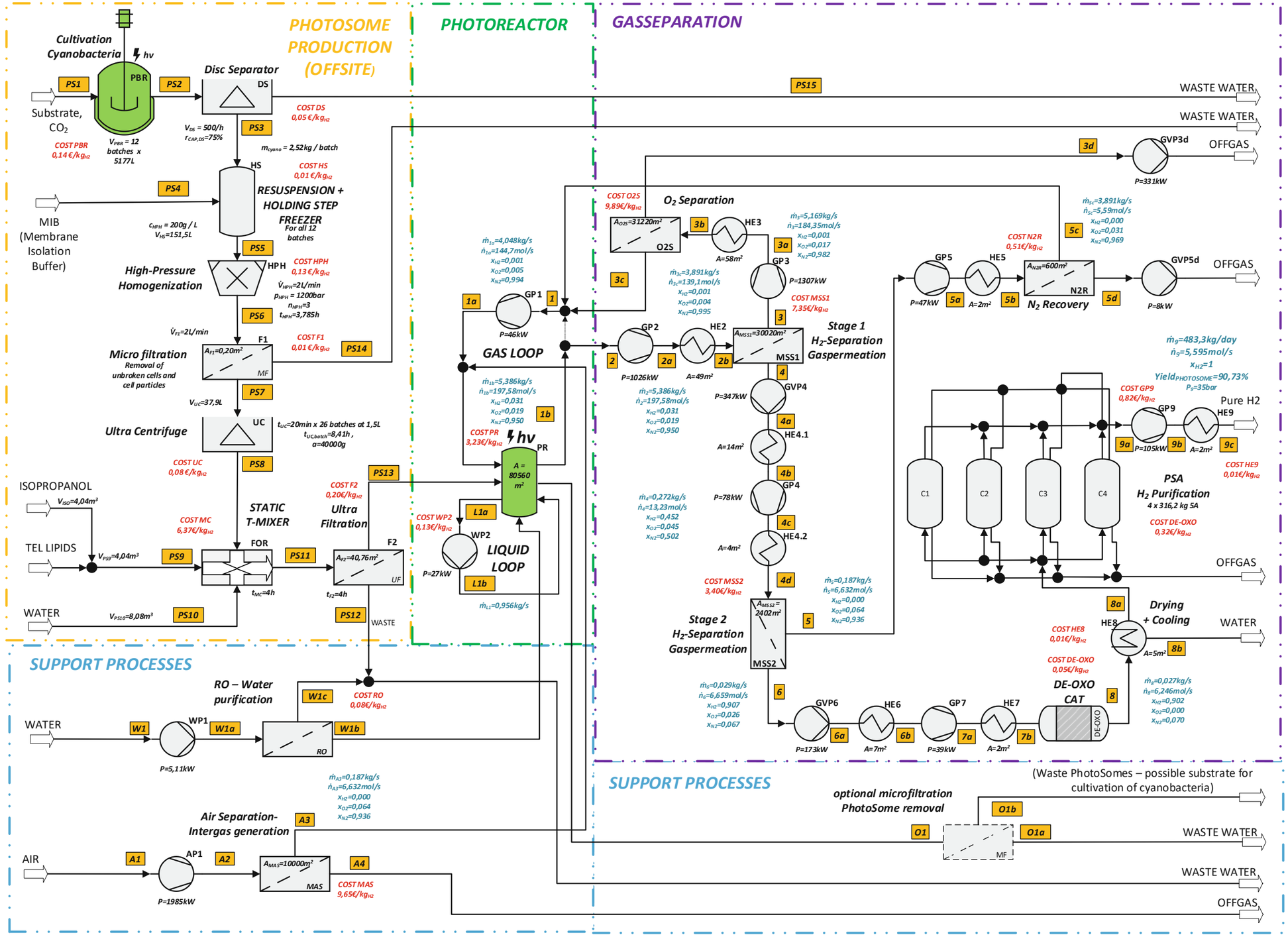

Fig. 35 Results PhotoSomes PSA CONCEPT

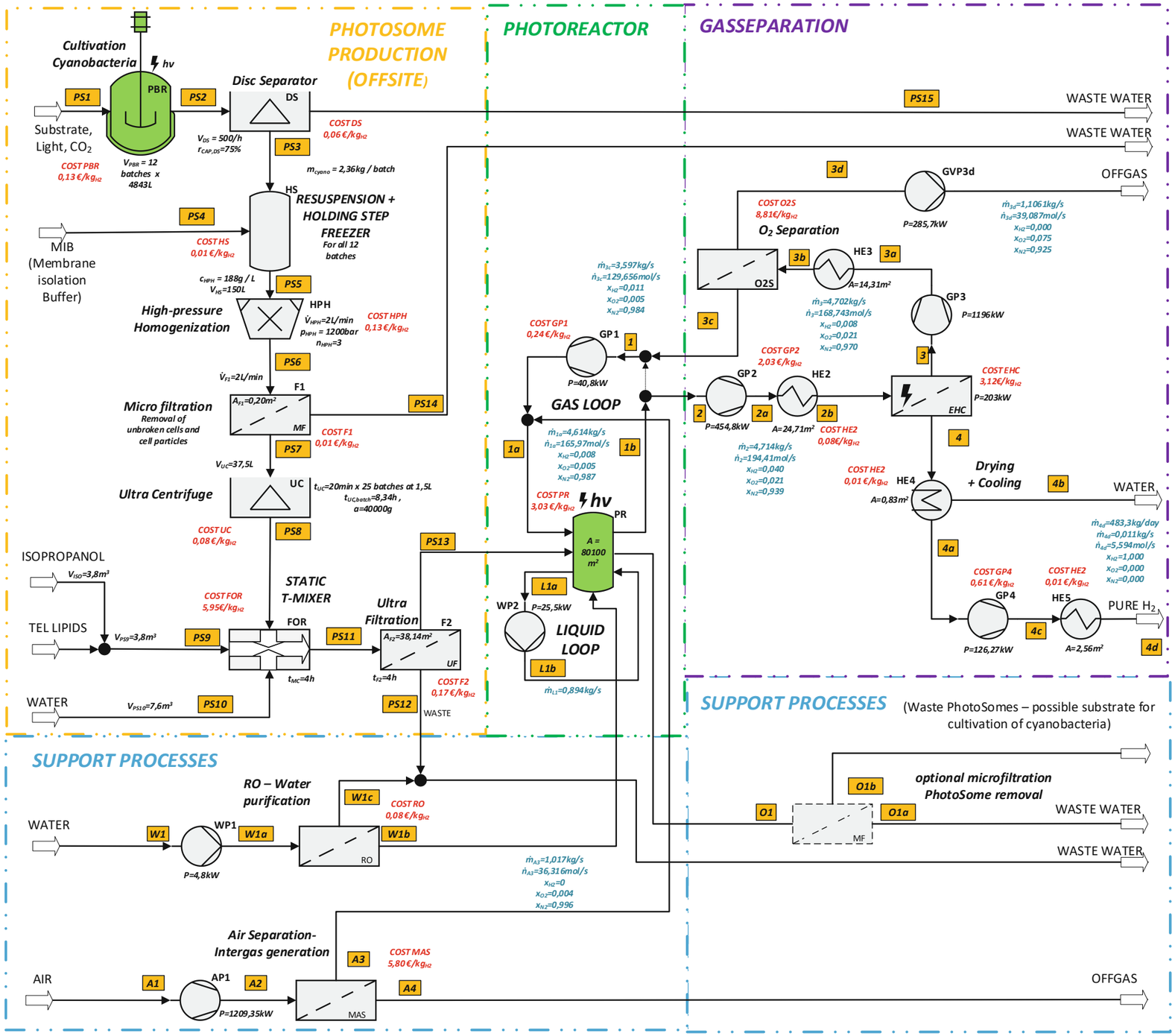

Fig. 36 RESULTS EHC CONCEPT

The following Sankey diagrams present the gas flow of the gas separation.

SANKEY DIAGRAMMS PSA – CONCEPT

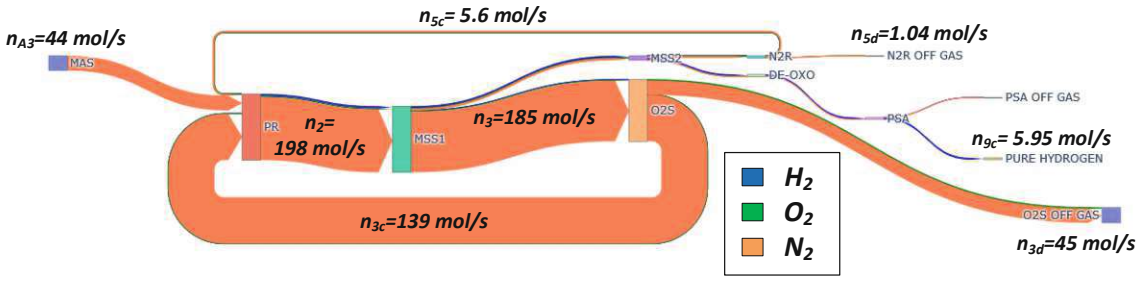

Fig. 37 SANKEY FLOW DIAGRAM PHOTOSOME PSA MOLAR FLOW

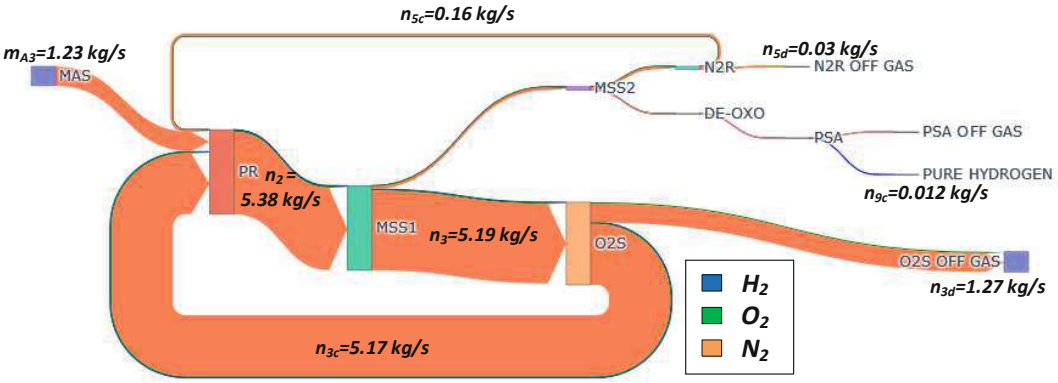

Fig. 38 SANKEY FLOW DIAGRAM PHOTOSOME PSA MASS FLOW

SANKEY DIAGRAMMS EHC – CONCEPT

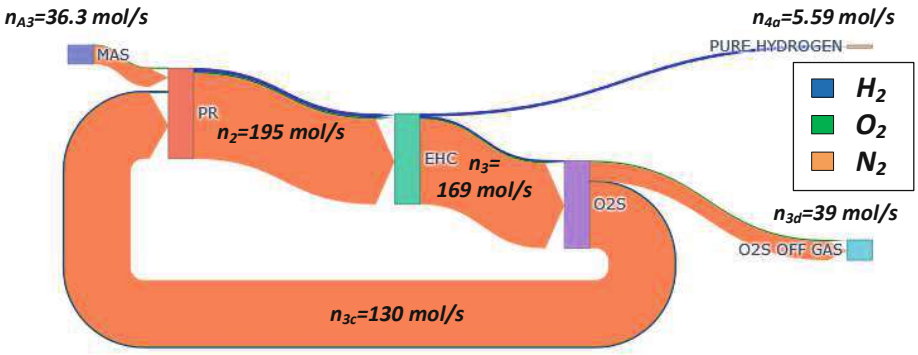

Fig. 39 SANKEY FLOW DIAGRAM PHOTOSOME EHC MOLAR FLOW

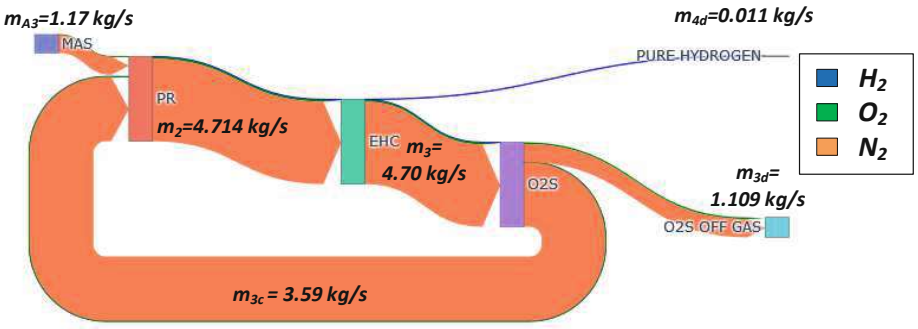

Fig. 40 SANKEY FLOW DIAGRAM PHOTOSOME EHC MASS FLOW

Comparison of power consumption in operation of both concepts:

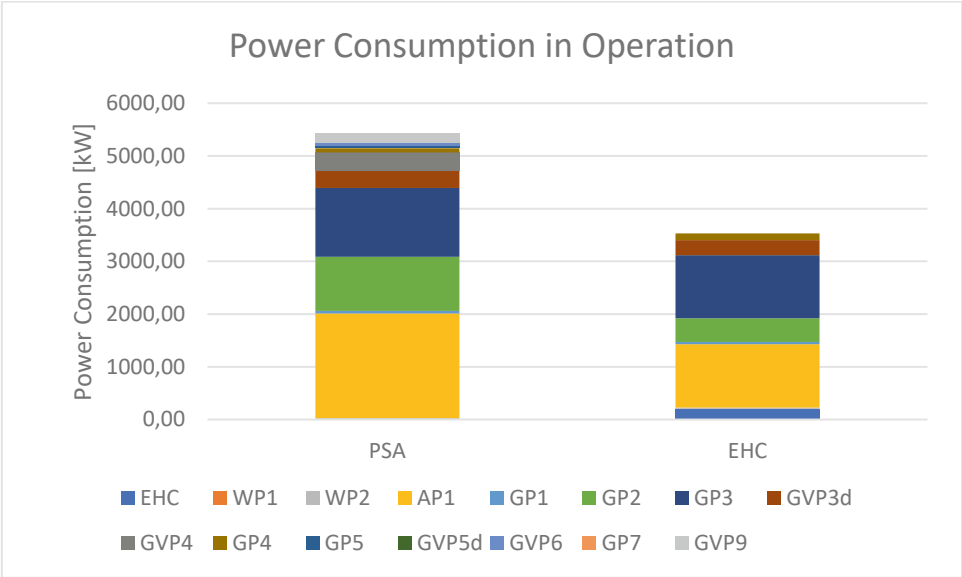

Tab. 26 Power consumption of both concept

The power requirement for the PSA – Concept amounts to 5.429 MW and 3.532 MW for the EHC during water splitting operation. This results into a daily energy consumption of 65.04 MWh/d for the PSA CONCEPT and 42.38 MWh/d for the EHC CONCEPT.

7.9. RESULTS of COST analysis

The cost per kg H_2 amounts to 41.16 € for the PSA – concept and 30.49€ for the EHC – concept. The gas separation accounts for the largest cost share in both concepts. 74% of the H_2 production cost of the EHC concept and 76% of the H_2 production cost of the PSA is derived from operating expenses.

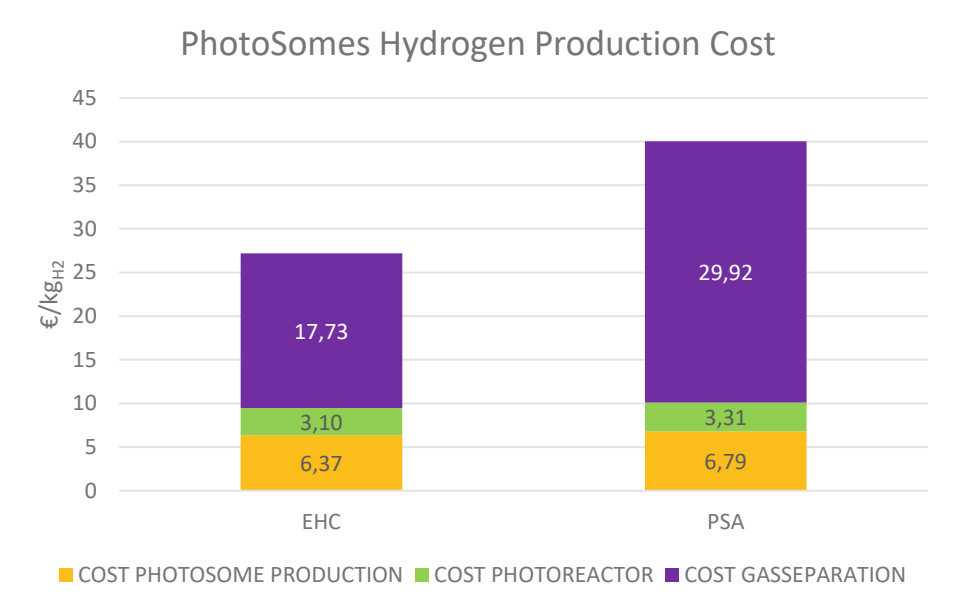

Tab. 27 Hydrogen production cost of PhotoSome concepts

COST OF PhotoSome Process				
	EHC		***PSA***	
COST PHOTOSOME PRODUCTION	€ 6.37	€/kgH_2	€ 6.79	€/kgH_2
COST PHOTOREACTOR	€ 3.10	€/kgH_2	€ 3.31	€/kgH_2
COST GASSEPARATION	€ 17.73	€/kgH_2	€ 29.92	€/kgH_2
COST per kg of H_2	€ 30.49	€/kgH_2	€ 41.16	€/kgH_2
COST GASSEPARATION OPEX	€ 3 977 238.81	€/a	€ 5 524 785.18	€/a
COST GASSEPARATION CAPEX	€ 1 386 602.42	€/a	€ 1 737 391.68	€/a
OPEX per kg of H_2	€ 22.54	€/kgH_2	€ 31.32	€/kgH_2
CAPEX per kg of H_2	€ 7.86	€/kgH_2	€ 9.85	€/kgH_2

Tab. 28 Results Cost analysis

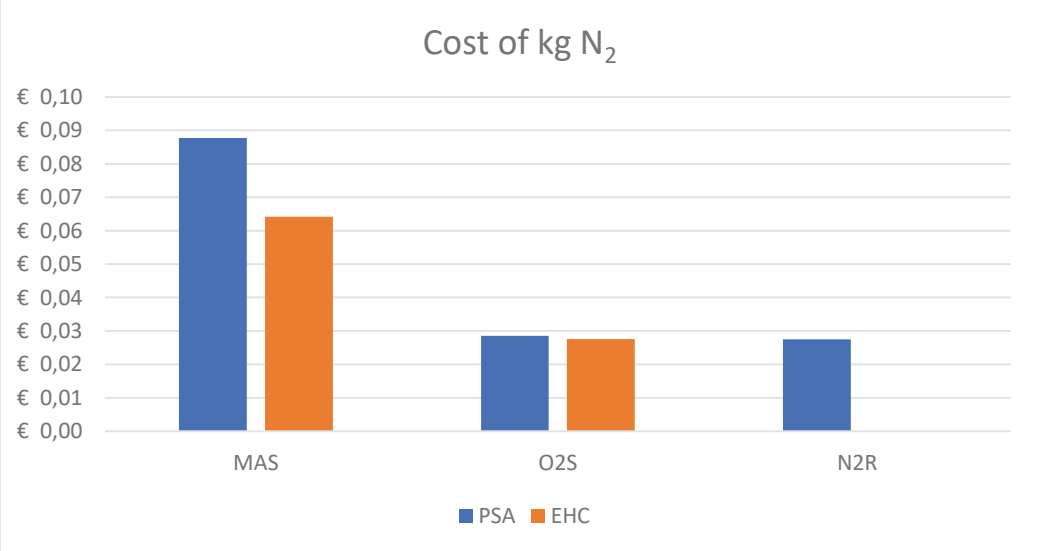

Tab. 29 Production cost of nitrogen

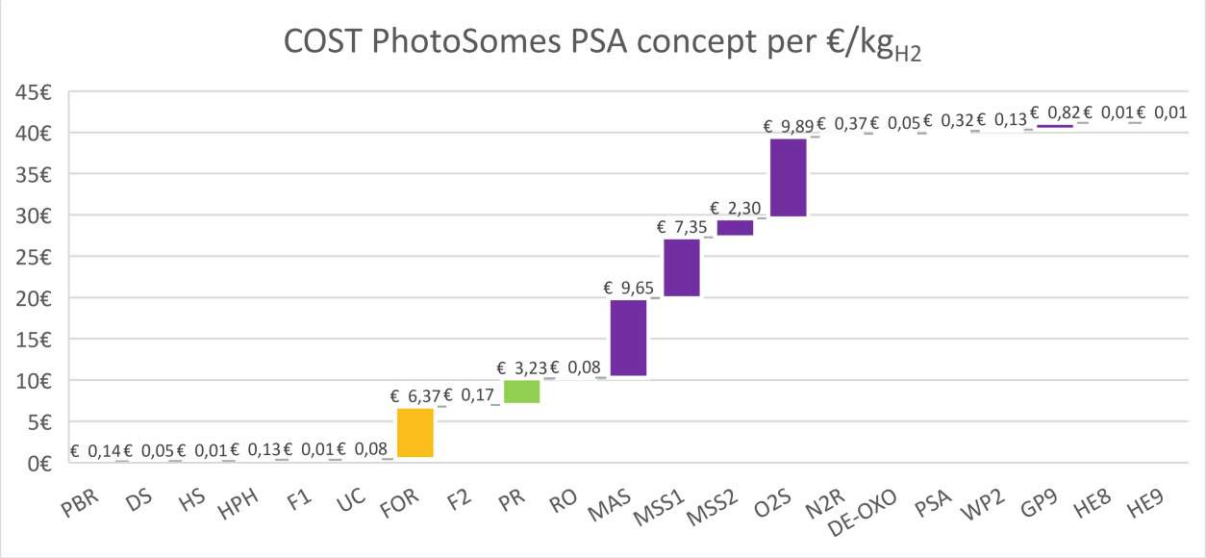

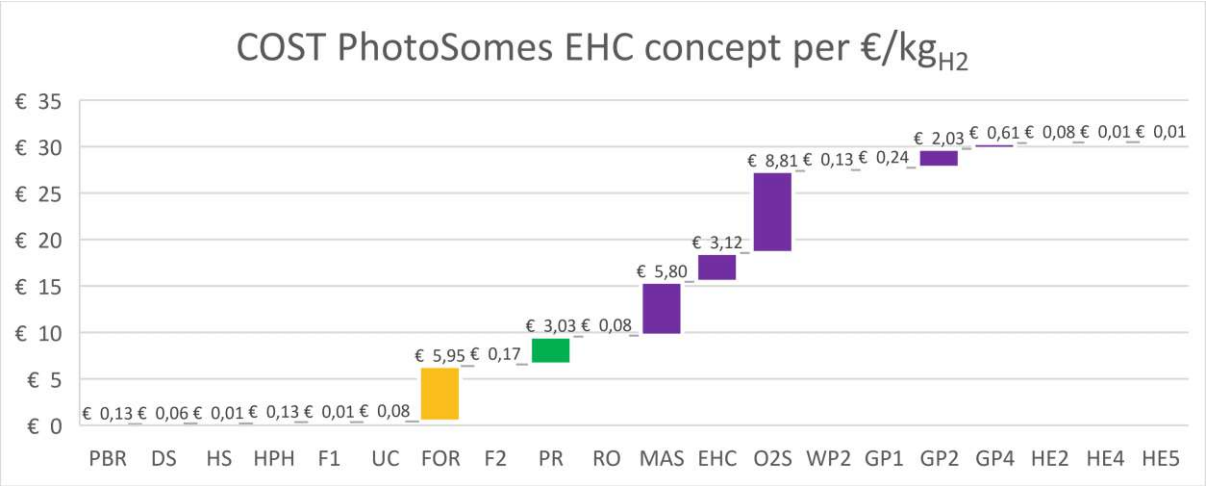

Tab. 30 Results Cost analysis PhotoSome - Unit Operations

The cost of TEL lipids amounts to 98.5 % of the cost for FOR at 5.87€/kg H_2 for EHC Concept and 6.27 €/kgH_2 for PSA Concept. The main cost drivers are the cost of electricity and the cost of lipids.

8. Discussion

8.1. Discussion of the literature study

Green H_2 will play a vital role in the decarbonization of industrial production. Global H_2 production will increase more than 4-fold by 2050 to slightly over 400 Mt/yr [198, p. 110]. Decarbonization of the H_2 value chain and meeting this massive future demand will require a tremendous effort and quick implementation of green H_2 production sites. However, besides already established technologies such as electrolysis or ones based on prior established technologies like solar-thermo-chemical H_2, novel green H_2 production technologies are still in their infancy.

The H_2 value chain is still under development, and the standards, regulations and best practices surrounding H_2 as well. Regulations have been developed with current mature technologies in mind. If H_2 fuel standards such as ISO 14678 remain as demanding as they are currently or will evolve to consider new technologies remains to be seen. This might allow for higher inert gas concentrations and lower unnecessary separation efforts as this should not decrease the performance of PEM fuel cells.

Photocatalytic H_2 methods are capable of overall water splitting, have reached TRL 5 and first pilot plants have been constructed. However, without achieving a net energy gain. SAPS haven't yet left the lab. Although some catalysts have lifetimes in the range of months, STH efficiencies below 5% and the separation of H_2 from the oxyH_2 gas mixture remain obstacles to commercialization.

As for SAPS, most are not capable of unassisted, bias-free overall water splitting. The few systems that are capable of overall water splitting rely on a second artificial photosensitizer like TiO_2 or Ru-ppy dye [114] [108] and do not require a sacrificial electron doner. Lipid-based systems have been developed but also require a second artificial photosensitizer [77].

Comparing the listed SAPSs has been a challenge. Not all studies provide the same performance parameters, only a few also provide STH efficiency. Input parameters such as spectrum, light intensity, environmental parameters can vary. Unassisted, bias-free pure water splitting at neutral visible light conditions is impossible with most systems. None of the listed SAPSs has exceeded the TRL 3. The most extended operating times have been achieved with semiconductor enzyme hybrids with up to 72h [105], [106]. The highest visible light STH of 5.4% has been achieved by Mersch et al. with a PS2 based PEC system by immobilizing PS2 on a IO-mesoITO anode and coupling it with a IO-mesoITO [NiFeSe]-H_2ase photocathode with an applied bias of 0.8V [33]. Most systems are limited by electron transfer. Thylakoid-based systems face quick photodegradation. None of the papers mention any strategies for scale-up. Liposome-based SAPSs have been constructed [77].

8.2. Discussion of the PhotoSomes as a SAPS

The PhotoSomes still surround several open questions. First, the random integration into the bilipid layer of the liposome and electron transfer regarding high electron transfer efficiencies. In order to improve this transfer, the catalytic center needs to be as close as possible to the photosensitizer. Direct electron transfer is more preferred than redox mediated electron transport for instance, by chinones. This location issue is further exacerbated by the orientations problem. Yet, it is unclear how the fragments orient themselves during formulation relative to the center of the liposome. The challenges of fragment orientation, mismatched PS2/PS1 ratio and position of the fragment are discussed in detail on page 47.

A possible improvement could be the recombinant expression of H_2ase next to PS1 to improve electron transfer. Weiner et al. for instant successfully express a ferredoxin-H_2ase fusion enzyme in *Chlamydomonas reinhardtii* [199]. This could potentially replace redox mediated with direct electron transport. A complementary approach to improve the electron transport in the liposome could be the

encapsulation of a redox mediator, for instance MV^{2+}, within the aqueous compartment to supplement the electron transport in the bilipid layer. This would allow for electron extraction at several points of the electron transfer chain in case of insufficient electron transfer via the bilipid layer and could connect the photosensitizer with the H_2ase. However, this redox carrier could inactivate the thylakoid fragments and damage the liposome, also it might be challenging to scale-up this construct as MV^{2+} is toxic.

The performance of the PhotoSome could also be improved by a complementary photosensitizer in the green or ultraviolet spectra like SiO_2 with 320 nm absorption similar to Chen et al. experiment[77]. If one takes into account that photosynthesis is a process, highly optimized by evolution, any additional steps or losses in the electron transfer chain will probably lead to insufficient potential for water splitting as the remaining overpotential at the Fb site to H^+/H_2 potential is only -0.16V vs SHE to allow for water splitting as shown in *Fig. 10*.

Secondly, the question how the liposome can protect the photosystems and H_2ase if TEL lipids are forming the PhotoSome together with residual conventional lipids of thylakoid membrane fragments. Also, since the photoinhibition repair mechanism for PS2 is part of the cell metabolism, it begs the question how a compartmentalized system with only certain components of the photosynthetic system will affect the lifetime. H_2ase should not be a limiting factor, even though O_2 stable variants, such as NiFeSe H_2ase show lower TON, O_2 sensitive variants can be engineered to withstand higher O_2 levels. In chapter "*4 PhotoSomes – liposome based SAPSs*" this has been discussed in detail.

How the PhotoSomes are influenced by surfactants and isopropanol required for the formulation is unclear yet.

Looking back at the literature study, thylakoid membranes-based SAPS inactivated within hours and thylakoid membrane-based PV-cells are reaching days to weeks at best, lets the assumption of a PhotoSome lifetime of 6 months seem quite excessive at this point.

8.3. Discussion of the experimental oxy-H_2 Separation by an EHC

The experiments with the EHC showed clearly that separation of H_2 of a diluted oxyH_2 mixture is possible even though at high energy consumption. This could be the result of setting the separation potential too high and of oxidation on the current collector plates. The separation efficiency and capture rate need to be improved. For further experiments, better and broader analytics are necessary to determine retentate and permeate composition. This will allow a detailed analysis of the corrosion issue. Other membrane assemblies and catalysts should be studied.

8.4. Discussion of the Process Design.

The scale-up of all suspended photocatalytic processes is challenging because of the separation of H_2. Without gas separation by design, e.g. spatially separated H_2 and O_2 evolution site designs, like 2 separate photoelectrodes, gas separation of diluted oxyH_2 remains the only feasible option. However, besides N_2 and CO_2 there is another option as dilution gas – Air! Only H_2 concentration must remain outside the flammability limits. This would result in higher partial O_2 pressures in the feed compared to the CO_2 or N_2 designs. Currently, gas permeation membranes can't offer sufficient selectivity to separate H_2 above the UFL in one stage. A two-stage process would also exceed the LOC in the intermediate step. Given this would allow for an open gas loop design, this approach should be revisited when higher-performing membranes with higher O_2-N_2 selectivities get available.

One should not be misled by the simplification taken in this approach. The inherent unsteadiness of renewable energy sources is a challenge for the process design. This begs the question of how to deal with quickly changing gas production rates and how to provide a level gas flow to the gas separation system. Further, there is still the question of the freezing issue in winter. The system could be either heated, insulated or chemically optimized. Heating such a large system seems too expensive, an

insulated photoreactor by vacuum – similar to vacuum pipe collectors – is also expensive and chemical components in the aqueous solutions such as salt provide a corrosion risk and would be an additional expense. The photo reactor could be emptied over the winter, increasing downtime and cost of the systems.

Heat could also pose a problem depending on the system's location, especially in hot regions a cooling system for the photo reactor could be required. In these areas, sufficient water supply poses an additional obstacle.

8.5. Discussion of the scale-up and cost analysis.

A wide range of estimations was necessary for the scale-up and cost analysis.

Starting with the photo reactor. The required amount of PhotoSomes might need to be higher for 2 reasons. The 20-layer model based on full coverage of at least one TEL to absorb all impacting sunlight will only provide sufficient effective photon capture under perfect uniform distribution in the PR and under perpendicular sunlight. At other angles, sunlight might not be fully absorbed. Also, positive effects due to shading leading to lower oversaturation and light inhibition are impossible. The cost analysis for the PR was only designed on very rough weight figures for the materials. Improved designs based on glass or plastics could further reduce cost.

The RO was designed for a flowrate to fill the PR in nearly 80 hours. Flushing the system might not be possible in case of contamination with this rather low flow. A CIP system for the PR was dismissed on purpose. As the PR has a volume of close to 2400m^3 and geometry won't allow for a spraying system, fully filling the system with CIP chemicals seems unrealistic. The system needs to rely on its self-decontamination ability.

The PhotoSome Production is designed for 2 batches per year. With commercial equipment, the process times are in the range of hours at best. Even though broken down to €/kgH_2 the cost of these unit operations is already low, running the equipment only 2 days a year is not economical. All unit operations of the PhotoSome production, except for the T-shape mixer for formulation, should be already at available at most downstream contractors. Outsourcing, or if enough demand is generated a central dedicated PhotoSome production facility is preferable to a delocalized PhotoSome production facility next to each PhotoSome PR.
Initial expectations that the isolation of compounds would limit the PhotoSome production could not be verified. The quantities are still small enough for a lab technician to process with a regular UC. 15 minutes of sedimentation time in the UC might be short, but even if process times amount to 60 minutes, this would only lead to an increase of the UC cost by a factor of 4 to from 0.08€ to 0.32€/kg$_{H2}$ which still pales in comparison to the cost of crude TEL per kg H_2 of around 6€. However, a concept with isolated photosensitizers and H_2ase might need longer sedimentation times. Continuous flow ultracentrifuges should be capable of lifting this limitation but given their high price point close to 1000000€ should be fully utilized.

In case the ultrafiltration F2 is not sufficient for the removal of the organic phase to allow for the formation of the PhotoSome an additional solvent evaporation unit operation might be required.

As insufficient data is available, buffers, surfactants and other additives for the isolation and formulation have not been considered in the process and cost analysis.. Concerning the formulation step the main limiting factor for the PhotoSome production is the price point of the TEL lipids.

The gas separation was also based on a range of assumptions and simplifications. First of all, the pressure drop of almost 3 bars in the retentate after each membrane separation is an estimation and might be too high. Secondly, the vacuum pumps were necessary to allow for free flow conditions in

the membrane model, but because of the high compression ratio of 20 from 0.05 bar to 1 bar, the energy consumption is quite high. A system based on a transmembrane pressure of 4 bar with a feed pressure of 5 bar might need less energy and is cheaper. Experimental data would help to improve this membrane separation step.

Since the gas compression is isentropic without cooling, the gas temperature at the outlets is high, especially at the vacuum pumps, exceeding 1100 K. Improved gas compression with intercooling should improve the power consumption further. The effect of these high temperatures on the flammability limits of the gas mixture have yet to be considered.

The gas separation was modeled with dry gas flows, however a fully saturated feed gas stream from the PR should be expected. As data on the wet diluted oxyH_2 gas mixture was unavailable, a rough estimation based on air with the help of a Mollier diagram showed a saturation at 1 bar and 40 °C of 1.1 kg H_2O/kg Air. The moisture permeability could be significant, increasing gas flows and energy consumption of the compression in the gas loop.

Also, the simplification of the PI-membrane is questionable. Lacking data, a 100% H_2 rejection (permeability of 0) was assumed for the operation O_2S and N_2R. This is probably too high and should be optimized with experimental data. However, given the costs of recovered N_2 from the UP O2S and N2R for both concepts are slightly below 30 €/t, about the same of the literature reference value for onsite N_2, shows the feasibility of gas loops, however the cost of N_2 from the MAS is more than 2 times more expensive. As onsite N_2 is around 33€/t, this could be an indicator that optimization of the MAS could lead to a cost optimization for the PSA concept in the range of 6 €/kgH_2 and the EHC concept around 4 €/kgH_2. N_2 – Air capture PSA system might be more feasible here. As clearly shown in the Sankey diagrams Fig. 37 to Fig. 40, the biggest obstacle in the gas separation remains the high gas flow in the gas loop due to the dilution below 4vol% H_2, equivalent to a hydrogen mass fraction of only w_{H2} = 0.003, compared to the final product stream creating high energy costs and large separation systems.

In theory, the Austrian standard for piped natural gas ÖVGW GB210:2011 would allow to inject low purity H_2-N_2 gas mixtures in the gas grid. It is a question of dilution. Hydrogen can be mixed to up to 10% into the grid. Nitrogen concentrations of up to 5% are allowed. However, oxygen may not exceed 0.001% over 24h and the injected gas needs to be dry to prevent corrosion. There are further considerations about caloric value. At best, this would only replace the PSA UP with 0.32€/kgH_2 offering only minor cost benefits. The decision to compare a PhotoSome system capable of fuel cell grade hydrogen with other technologies is therefore justified.

The PSA can maybe replace the DE-OXO catalyst, but this would require a further safety analysis of the PSA purification step and additional experimental effort with the permeate gas mixture of MSS2 of the PSA-Concept. As the power requirement of the EHC concept exceeds 3 MW and the PSA-concept 5 WM and as the daily energy consumption of 65.04 MWh/d for the PSA CONCEPT is 2.71 times and 42.38 MWh/d for the EHC CONCEPT is 1.76 times higher than that of the 1 MW electrolyzer system, the PhotoSome system does not operate at a net energy gain and is therefore already not feasible.

The cost estimate resulted in 41.16 €/kgH_2 for the PSA System and 30.49 €/kgH_2 far exceeding the analysis of Pinaud et la. From 2011 of 1.64 €/kgH_2 [31] and also missing the goal of 3 €/kgH_2 that green H_2 needs to hit by 2050. Pinaud et al. achieved in their theoretical analysis this low price in a large-scale baggie system with a 10% STH and a mean solar input of 5.25 kWh/ (m^2 * day) about 50% higher than in this study. They also state that baggies of 323 m x 12.2 m x 0.1 m in size may present practical limitations in that a failure in the mechanical integrity due to weather, bird damage, etc. of a single baggie would result in a significant release of electrolyte and plant capacity. The undiluted

oxyH_2 gas mixture is compressed by an oil-free piston compressor and purified by a PSA system. They disregard the safety issues of separating an oxyH_2 gas mixture. A 300 m long 12 m wide baggy, essentially a balloon, partially filled with oxyH_2 poses a significant safety hazard.

The gas permeation with the UP MSS1 and MSS2 was modeled after a paper by Alsayegh et la.[150]. They achieved a 92% recovery and 92.5% purity at a cost of 8.20 $\$_{2017}/kgH_2$ at lower energy prices of 0.084 €/kWh and plant lifetime of 15 years. This is comparable to MSS1 and MSS2 of the PSA CONCEPT that combined lead to a production cost of 9.65 €/kgH_2.

The main constraints for the PhotoSome concepts are the cost of the TEL lipids, the cost of stainless steel for the photo reactors and the safety hazard of separating an oxyH_2 gas mixture with the necessary H_2 dilution below 4% and the subsequent large, energy-intensive separation process. At this point, the H_2 production by a single suspended PhotoSome catalyst is not feasible.

The goal of this thesis is a feasibility study of a potential scale-up of the semi-artificial photosynthetic particulate, suspended fully biological lipid-based PhotoSome process. An overview of the H_2 value chain with current and future H_2 demand, standards and requirements was given. H_2 production methods have been described, especially for green H_2 have been compared on their level of development and cost effectiveness with a focus on solar H_2 and photocatalytic production methods. A holistic review of H_2 producing semi-artificial photosynthetic photocatalytic publications has been written. A safe PhotoSome process has been designed with 2 different approaches for gas separation. A cost analysis for both approaches has been undertaken. This is the first holistic cost analysis of an intertizised suspended photocatalytic H_2 production process, including inert gas production. The biggest obstacles to the scale-up have been identified. At this point the PhotoSome technology is not feasible for H_2 production because of an energy-intensive gas separation.

The goals of this thesis have been achieved.

At this point the PhotoSome technology is not feasible for H_2 production because of energy-intensive gas separation and cost of TEL lipids.

9. Outlook:

For further consideration of the PhotoSome process experimental data for all unit operations is required! A second cost analysis should include a sensitivity study showing the impact of changes in electricity prices and solar intensity.

For further development of the PhotoSome system, the focus should be on higher-value products. As SAPS can produce more complex, high value products, not yet possible with photocatalytic systems that will be needed in the green H_2 economy such as acetate and formate. This way, the formation of an explosive gas mixture is avoided in the first place and energy and cost-intensive separation is unnecessary.

If PhotoSome prove to be long-term stable and the cost of crude TEL lipids is further reduced, a dual baggie set-up for H_2 production with 2 different PhotoSome catalysts – spatially separating O_2 and H_2 evolution should be revisited as this would double the cost of PhotoSomes and the PR but would replace the gas separation.

References

[1] A. Pannwitz *et al.*, "Roadmap towards solar fuel synthesis at the water interface of liposome membranes," *Chem. Soc. Rev.*, vol. 50, no. 8, pp. 4833–4855, Apr. 2021, doi: 10.1039/D0CS00737D.

[2] IPCC, "Climate Change 2022 Mitigation of Climate Change Summary for Policymakers." https://www.ipcc.ch/report/ar6/wg3/downloads/report/IPCC_AR6_WGIII_SPM.pdf (accessed Jun. 16, 2023).

[3] Z. Liu, Z. Deng, S. J. Davis, C. Giron, and P. Ciais, "Monitoring global carbon emissions in 2021," *Nat. Rev. Earth Environ.*, vol. 3, no. 4, Art. no. 4, Apr. 2022, doi: 10.1038/s43017-022-00285-w.

[4] H. Ritchie, M. Roser, and P. Rosado, "CO_2 and Greenhouse Gas Emissions," *Our World Data*, May 2020, Accessed: Jun. 16, 2023. [Online]. Available: https://ourworldindata.org/co2-and-greenhouse-gas-emissions

[5] "The Future of Hydrogen – Analysis," *IEA*. https://www.iea.org/reports/the-future-of-hydrogen (accessed Jun. 16, 2023).

[6] C. S. Tao, J. Jiang, and M. Tao, "Natural resource limitations to terawatt-scale solar cells," *Sol. Energy Mater. Sol. Cells*, vol. 95, no. 12, pp. 3176–3180, Dec. 2011, doi: 10.1016/j.solmat.2011.06.013.

[7] S. Shammugam, E. Gervais, T. Schlegl, and A. Rathgeber, "Raw metal needs and supply risks for the development of wind energy in Germany until 2050," *J. Clean. Prod.*, vol. 221, pp. 738–752, Jun. 2019, doi: 10.1016/j.jclepro.2019.02.223.

[8] B. Sørensen, Ed., "Chapter 2 - Hydrogen," in *Hydrogen and Fuel Cells (Second Edition)*, in Sustainable World. Boston: Academic Press, 2012, pp. 5–94. doi: 10.1016/B978-0-12-387709-3.50002-4.

[9] IEA, "Global Hydrogen Review 2022 – Analysis," *IEA*, Accessed: Jun. 17, 2023. [Online]. Available: https://www.iea.org/reports/global-hydrogen-review-2022

[10] C. Acar and I. Dincer, "3.1 Hydrogen Production," in *Comprehensive Energy Systems*, I. Dincer, Ed., Oxford: Elsevier, 2018, pp. 1–40. doi: 10.1016/B978-0-12-809597-3.00304-7.

[11] IEA, *Global Hydrogen Review 2021*. Paris: Organisation for Economic Co-operation and Development, 2021. Accessed: Jun. 17, 2023. [Online]. Available: https://www.oecd-ilibrary.org/energy/global-hydrogen-review-2021_39351842-en

[12] R. Łukajtis *et al.*, "Hydrogen production from biomass using dark fermentation," *Renew. Sustain. Energy Rev.*, vol. 91, pp. 665–694, Aug. 2018, doi: 10.1016/j.rser.2018.04.043.

[13] KPMG, "The hydrogen trajectory - KPMG Belgium," *KPMG*, Nov. 24, 2022. https://kpmg.com/be/en/home/insights/2021/03/eng-the-hydrogen-trajectory.html (accessed Jun. 17, 2023).

[14] E. Nurkanovic, "Costs of Hydrogen : Through history and currently from different technologies and energy sources," Thesis, Wien, 2020. Accessed: Jun. 17, 2023. [Online]. Available: https://repositum.tuwien.at/handle/20.500.12708/1252

[15] B. C. Tashie-Lewis and S. G. Nnabuife, "Hydrogen Production, Distribution, Storage and Power Conversion in a Hydrogen Economy - A Technology Review," *Chem. Eng. J. Adv.*, vol. 8, p. 100172, Nov. 2021, doi: 10.1016/j.ceja.2021.100172.

[16] R. Lan and S. Tao, "Ammonia as a Suitable Fuel for Fuel Cells," *Front. Energy Res.*, vol. 2, 2014, Accessed: Jun. 17, 2023. [Online]. Available: https://www.frontiersin.org/articles/10.3389/fenrg.2014.00035

[17] Fraunhofer-Zentrum für Energiespeicher und Systeme ZESS, "POWERPASTE - chemische Wasserstoffspeicherung," *Fraunhofer-Zentrum für Energiespeicher und Systeme ZESS*. https://www.fraunhofer.de/de/schwerpunkte/zess_wasserstofftechnologien/powerpaste-hydrierung_von_magnesium.html (accessed Jun. 17, 2023).

[18] G. N. B. Durmus, C. O. Colpan, and Y. Devrim, "A review on the development of the electrochemical hydrogen compressors," *J. Power Sources*, vol. 494, p. 229743, May 2021, doi: 10.1016/j.jpowsour.2021.229743.

[19] J. Völpel, "Reinheit von Wasserstoff: Wer nutzt welche Bezeichnung?," *EMCEL*, Sep. 16, 2020. https://emcel.com/de/reinheit-von-wasserstoff/ (accessed Jun. 17, 2023).
[20] U. Lubenau and D. Baumann, "Wasserstoffqualitätsanforderungen", Accessed: Jun. 17, 2023. [Online]. Available: https://www.dbi-gruppe.de/files/PDFs/Dokumente/11_GWB/2020_Bericht%20GWB_31.pdf
[21] F. Calise, M. Dentice D'Accadia, M. Santarelli, A. Lanzini, and D. Ferrero, *Solar hydrogen production: processes, systems and technologies*. London, United Kingdom: Academic Press, an imprint of Elsevier, 2019. Accessed: Jun. 17, 2023. [Online]. Available: https://www.sciencedirect.com/science/book/9780128148532
[22] M. Nasser, T. F. Megahed, S. Ookawara, and H. Hassan, "A review of water electrolysis–based systems for hydrogen production using hybrid/solar/wind energy systems," *Environ. Sci. Pollut. Res.*, vol. 29, no. 58, pp. 86994–87018, Dec. 2022, doi: 10.1007/s11356-022-23323-y.
[23] G. Chen, X. Tu, G. Homm, and A. Weidenkaff, "Plasma pyrolysis for a sustainable hydrogen economy," *Nat. Rev. Mater.*, vol. 7, no. 5, Art. no. 5, May 2022, doi: 10.1038/s41578-022-00439-8.
[24] S. S. Rashwan, I. Dincer, and A. Mohany, "A review on the importance of operating conditions and process parameters in sonic hydrogen production," *Int. J. Hydrog. Energy*, vol. 46, no. 56, pp. 28418–28434, Aug. 2021, doi: 10.1016/j.ijhydene.2021.06.086.
[25] A. Inayat *et al.*, "Integrated adsorption steam gasification for enhanced hydrogen production from palm waste at bench scale plant," *Int. J. Hydrog. Energy*, vol. 46, no. 59, pp. 30581–30591, Aug. 2021, doi: 10.1016/j.ijhydene.2020.12.008.
[26] L. Cao *et al.*, "Biorenewable hydrogen production through biomass gasification: A review and future prospects," *Environ. Res.*, vol. 186, p. 109547, Jul. 2020, doi: 10.1016/j.envres.2020.109547.
[27] G. Melitos, X. Voulkopoulos, and A. Zabaniotou, "Waste to Sustainable Biohydrogen Production Via Photo-Fermentation and Biophotolysis − A Systematic Review," *Renew. Energy Environ. Sustain.*, vol. 6, p. 45, 2021, doi: 10.1051/rees/2021047.
[28] C. Putatunda *et al.*, "Current challenges and future technology in photofermentation-driven biohydrogen production by utilizing algae and bacteria," *Int. J. Hydrog. Energy*, vol. 48, no. 55, pp. 21088–21109, Jun. 2023, doi: 10.1016/j.ijhydene.2022.10.042.
[29] C. A. Rodriguez, M. A. Modestino, D. Psaltis, and C. Moser, "Design and cost considerations for practical solar-hydrogen generators," *Energy Environ. Sci.*, vol. 7, no. 12, pp. 3828–3835, Nov. 2014, doi: 10.1039/C4EE01453G.
[30] R. A. Grimme, C. E. Lubner, and J. H. Golbeck, "Maximizing H2 production in Photosystem I/dithiol molecular wire/platinum nanoparticle bioconjugates," *Dalton Trans.*, no. 45, pp. 10106–10113, Nov. 2009, doi: 10.1039/B909137H.
[31] B. A. Pinaud *et al.*, "Technical and economic feasibility of centralized facilities for solar hydrogen production via photocatalysis and photoelectrochemistry," *Energy Environ. Sci.*, vol. 6, no. 7, pp. 1983–2002, Jun. 2013, doi: 10.1039/C3EE40831K.
[32] K. A. Brown, S. Dayal, X. Ai, G. Rumbles, and P. W. King, "Controlled Assembly of Hydrogenase-CdTe Nanocrystal Hybrids for Solar Hydrogen Production," *J. Am. Chem. Soc.*, vol. 132, no. 28, pp. 9672–9680, Jul. 2010, doi: 10.1021/ja101031r.
[33] D. Mersch *et al.*, "Wiring of Photosystem II to Hydrogenase for Photoelectrochemical Water Splitting," *J. Am. Chem. Soc.*, vol. 137, no. 26, pp. 8541–8549, Jul. 2015, doi: 10.1021/jacs.5b03737.
[34] L. S. F. Frowijn and W. G. J. H. M. van Sark, "Analysis of photon-driven solar-to-hydrogen production methods in the Netherlands," *Sustain. Energy Technol. Assess.*, vol. 48, p. 101631, Dec. 2021, doi: 10.1016/j.seta.2021.101631.
[35] J. E. Lee, I. Shafiq, M. Hussain, S. S. Lam, G. H. Rhee, and Y.-K. Park, "A review on integrated thermochemical hydrogen production from water," *Int. J. Hydrog. Energy*, vol. 47, no. 7, pp. 4346–4356, Jan. 2022, doi: 10.1016/j.ijhydene.2021.11.065.
[36] M. Mehrpooya, B. Ghorbani, and M. Khodaverdi, "Hydrogen production by thermochemical water splitting cycle using low-grade solar heat and phase change material energy storage system," *Int. J. Energy Res.*, vol. 46, no. 6, pp. 7590–7609, 2022, doi: 10.1002/er.7662.

[37] S. Valizadeh *et al.*, "Valorization of biomass through gasification for green hydrogen generation: A comprehensive review," *Bioresour. Technol.*, vol. 365, p. 128143, Dec. 2022, doi: 10.1016/j.biortech.2022.128143.
[38] S. Dahiya, S. Chatterjee, O. Sarkar, and S. V. Mohan, "Renewable hydrogen production by dark-fermentation: Current status, challenges and perspectives," *Bioresour. Technol.*, vol. 321, p. 124354, Feb. 2021, doi: 10.1016/j.biortech.2020.124354.
[39] L. Cabrol, A. Marone, E. Tapia-Venegas, J.-P. Steyer, G. Ruiz-Filippi, and E. Trably, "Microbial ecology of fermentative hydrogen producing bioprocesses: useful insights for driving the ecosystem function," *FEMS Microbiol. Rev.*, vol. 41, no. 2, pp. 158–181, Mar. 2017, doi: 10.1093/femsre/fuw043.
[40] İ. Ergal *et al.*, "Biohydrogen production beyond the Thauer limit by precision design of artificial microbial consortia," *Commun. Biol.*, vol. 3, no. 1, Art. no. 1, Aug. 2020, doi: 10.1038/s42003-020-01159-x.
[41] G. Balachandar, J. L. Varanasi, V. Singh, H. Singh, and D. Das, "Biological hydrogen production via dark fermentation: A holistic approach from lab-scale to pilot-scale," *Int. J. Hydrog. Energy*, vol. 45, no. 8, pp. 5202–5215, Feb. 2020, doi: 10.1016/j.ijhydene.2019.09.006.
[42] A. Ghimire *et al.*, "A review on dark fermentative biohydrogen production from organic biomass: Process parameters and use of by-products," *Appl. Energy*, vol. 144, pp. 73–95, Apr. 2015, doi: 10.1016/j.apenergy.2015.01.045.
[43] H. Song, S. Luo, H. Huang, B. Deng, and J. Ye, "Solar-Driven Hydrogen Production: Recent Advances, Challenges, and Future Perspectives," *ACS Energy Lett.*, vol. 7, no. 3, pp. 1043–1065, Mar. 2022, doi: 10.1021/acsenergylett.1c02591.
[44] F. B. Oflaz and H. Koku, "Pilot-scale outdoor photofermentative hydrogen production from molasses using pH control," *Int. J. Hydrog. Energy*, vol. 46, no. 57, pp. 29160–29172, Aug. 2021, doi: 10.1016/j.ijhydene.2020.10.086.
[45] M. Roeb *et al.*, "Test operation of a 100kW pilot plant for solar hydrogen production from water on a solar tower," *Sol. Energy*, vol. 85, no. 4, pp. 634–644, Apr. 2011, doi: 10.1016/j.solener.2010.04.014.
[46] M. Lee, S. Haas, V. Smirnov, T. Merdzhanova, and U. Rau, "Scalable Photovoltaic-Electrochemical Cells for Hydrogen Production from Water - Recent Advances," *ChemElectroChem*, vol. 9, no. 24, p. e202200838, 2022, doi: 10.1002/celc.202200838.
[47] J. Jia *et al.*, "Solar water splitting by photovoltaic-electrolysis with a solar-to-hydrogen efficiency over 30%," *Nat. Commun.*, vol. 7, no. 1, Art. no. 1, Oct. 2016, doi: 10.1038/ncomms13237.
[48] S. E. Braslavsky, "Glossary of terms used in photochemistry, 3rd edition (IUPAC Recommendations 2006)," *Pure Appl. Chem.*, vol. 79, no. 3, pp. 293–465, Jan. 2007, doi: 10.1351/pac200779030293.
[49] N. Zhang, "Photocatalytic Overall Water Splitting," in *Photo- and Electro-Catalytic Processes*, John Wiley & Sons, Ltd, 2022, pp. 521–539. doi: 10.1002/9783527830084.ch15.
[50] R. Hemam, O. Bisen, S. Nanda, R. Nandan, and K. Nanda, "Internal versus external quantum efficiency of luminescent materials, photovoltaic cells, photodetectors and photoelectrocatalysis," *Curr. Sci.*, vol. 121, Jul. 2021, doi: 10.18520/cs/v121/i7/894-898.
[51] Y. Sun *et al.*, "Chapter 14 - Applications of MXenes and their composites in catalysis and photoelectrocatalysis," in *Mxenes and their Composites*, K. K. Sadasivuni, K. Deshmukh, S. K. K. Pasha, and T. Kovářík, Eds., in Micro and Nano Technologies. Elsevier, 2022, pp. 449–498. doi: 10.1016/B978-0-12-823361-0.00007-1.
[52] B.-J. Ng, L. K. Putri, X. Y. Kong, Y. W. Teh, P. Pasbakhsh, and S.-P. Chai, "Z-Scheme Photocatalytic Systems for Solar Water Splitting," *Adv. Sci.*, vol. 7, no. 7, p. 1903171, 2020, doi: 10.1002/advs.201903171.
[53] Kelvinsong, *English: Diagram of a cyanobacterium. Based on 1, 2 3, and 4. Designed to be viewed at 680×380 px.* 2013. Accessed: Jun. 17, 2023. [Online]. Available: https://commons.wikimedia.org/wiki/File:Cyanobacterium.svg#/media/File:Cyanobacterium-inline.svg
[54] R. Kourist and S. Schmidt, Eds., "The Autotrophic Biorefinery: Raw Materials from Biotechnology," in *The Autotrophic Biorefinery*, De Gruyter, 2021. doi: 10.1515/9783110550603.

[55] K. Xiao *et al.*, "Panoramic insights into semi-artificial photosynthesis: origin, development, and future perspective," *Energy Environ. Sci.*, vol. 15, no. 2, pp. 529–549, Feb. 2022, doi: 10.1039/D1EE03094A.
[56] Q. Wang *et al.*, "Particulate Photocatalyst Sheets Based on Carbon Conductor Layer for Efficient Z-Scheme Pure-Water Splitting at Ambient Pressure," *J. Am. Chem. Soc.*, vol. 139, no. 4, pp. 1675–1683, Feb. 2017, doi: 10.1021/jacs.6b12164.
[57] Q. Wang *et al.*, "Scalable water splitting on particulate photocatalyst sheets with a solar-to-hydrogen energy conversion efficiency exceeding 1%," *Nat. Mater.*, vol. 15, no. 6, Art. no. 6, Jun. 2016, doi: 10.1038/nmat4589.
[58] D. Zhao *et al.*, "Boron-doped nitrogen-deficient carbon nitride-based Z-scheme heterostructures for photocatalytic overall water splitting," *Nat. Energy*, vol. 6, no. 4, Art. no. 4, Apr. 2021, doi: 10.1038/s41560-021-00795-9.
[59] G. Zhang, Z.-A. Lan, L. Lin, S. Lin, and X. Wang, "Overall water splitting by Pt/g-C3N4 photocatalysts without using sacrificial agents," *Chem. Sci.*, vol. 7, no. 5, pp. 3062–3066, Apr. 2016, doi: 10.1039/C5SC04572J.
[60] Q. Wang *et al.*, "Oxysulfide photocatalyst for visible-light-driven overall water splitting," *Nat. Mater.*, vol. 18, no. 8, Art. no. 8, Aug. 2019, doi: 10.1038/s41563-019-0399-z.
[61] T. Takata *et al.*, "Photocatalytic water splitting with a quantum efficiency of almost unity," *Nature*, vol. 581, no. 7809, Art. no. 7809, May 2020, doi: 10.1038/s41586-020-2278-9.
[62] H. Nishiyama *et al.*, "Photocatalytic solar hydrogen production from water on a 100-m2 scale," *Nature*, vol. 598, no. 7880, Art. no. 7880, Oct. 2021, doi: 10.1038/s41586-021-03907-3.
[63] J. Liu *et al.*, "Metal-free efficient photocatalyst for stable visible water splitting via a two-electron pathway," *Science*, vol. 347, no. 6225, pp. 970–974, Feb. 2015, doi: 10.1126/science.aaa3145.
[64] L. Liao *et al.*, "Efficient solar water-splitting using a nanocrystalline CoO photocatalyst," *Nat. Nanotechnol.*, vol. 9, no. 1, Art. no. 1, Jan. 2014, doi: 10.1038/nnano.2013.272.
[65] Y. Goto *et al.*, "A Particulate Photocatalyst Water-Splitting Panel for Large-Scale Solar Hydrogen Generation," *Joule*, vol. 2, no. 3, pp. 509–520, Mar. 2018, doi: 10.1016/j.joule.2017.12.009.
[66] A. Ruiz-Aguirre *et al.*, "Assessment of pilot-plant scale solar photocatalytic hydrogen generation with multiple approaches: Valorization, water decontamination and disinfection," *Energy*, vol. 260, p. 125199, Dec. 2022, doi: 10.1016/j.energy.2022.125199.
[67] L. Wang, X. Zheng, L. Chen, Y. Xiong, and H. Xu, "Van der Waals Heterostructures Comprised of Ultrathin Polymer Nanosheets for Efficient Z-Scheme Overall Water Splitting," *Angew. Chem. Int. Ed.*, vol. 57, no. 13, pp. 3454–3458, 2018, doi: 10.1002/anie.201710557.
[68] Y. Lin, W. Su, X. Wang, X. Fu, and X. Wang, "LaOCl-Coupled Polymeric Carbon Nitride for Overall Water Splitting through a One-Photon Excitation Pathway," *Angew. Chem. Int. Ed.*, vol. 59, no. 47, pp. 20919–20923, 2020, doi: 10.1002/anie.202008397.
[69] H. Zou *et al.*, "Pyrochlore-structural Nd2Ta2O5N2 photocatalyst with an absorption edge of over 600 nm for Z-scheme overall water splitting," *Chem. Commun.*, vol. 58, no. 76, pp. 10719–10722, Sep. 2022, doi: 10.1039/D2CC02903K.
[70] S. Hu, C. Xiang, S. Haussener, A. D. Berger, and N. S. Lewis, "An analysis of the optimal band gaps of light absorbers in integrated tandem photoelectrochemical water-splitting systems," *Energy Environ. Sci.*, vol. 6, no. 10, pp. 2984–2993, Sep. 2013, doi: 10.1039/C3EE40453F.
[71] W.-H. Cheng *et al.*, "Monolithic Photoelectrochemical Device for Direct Water Splitting with 19% Efficiency," *ACS Energy Lett.*, vol. 3, no. 8, pp. 1795–1800, Aug. 2018, doi: 10.1021/acsenergylett.8b00920.
[72] A. Landman *et al.*, "Decoupled Photoelectrochemical Water Splitting System for Centralized Hydrogen Production," *Joule*, vol. 4, no. 2, pp. 448–471, Feb. 2020, doi: 10.1016/j.joule.2019.12.006.
[73] M. Ahmed and I. Dincer, "A review on photoelectrochemical hydrogen production systems: Challenges and future directions," *Int. J. Hydrog. Energy*, vol. 44, no. 5, pp. 2474–2507, Jan. 2019, doi: 10.1016/j.ijhydene.2018.12.037.
[74] X. Fang, S. Kalathil, and E. Reisner, "Semi-biological approaches to solar-to-chemical conversion," *Chem. Soc. Rev.*, vol. 49, no. 14, pp. 4926–4952, Jul. 2020, doi: 10.1039/C9CS00496C.

[75] S. I. Kim, Y. J. Kim, H. Hong, J. Yun, and W. Ryu, "Electrosprayed Thylakoid–Alginate Film on a Micro-Pillar Electrode for Scalable Photosynthetic Energy Harvesting," *ACS Appl. Mater. Interfaces*, vol. 12, no. 49, pp. 54683–54693, Dec. 2020, doi: 10.1021/acsami.0c15993.
[76] L. M. Utschig, S. R. Soltau, K. L. Mulfort, J. Niklas, and O. G. Poluektov, "Z-scheme solar water splitting via self-assembly of photosystem I-catalyst hybrids in thylakoid membranes," *Chem. Sci.*, vol. 9, no. 45, pp. 8504–8512, Nov. 2018, doi: 10.1039/C8SC02841A.
[77] Z. Chen, H. Zhang, and P. Guo, "Semi-artificial Photosynthetic CO2 Reduction through Purple Membrane Re-engineering with Semiconductor," *J. Am. Chem. Soc.*, vol. 141, no. 30, pp. 11811–11815, Jul. 2019, doi: 10.1021/jacs.9b05564.
[78] J. Warnan *et al.*, "Solar H2 evolution in water with modified diketopyrrolopyrrole dyes immobilised on molecular Co and Ni catalyst–TiO2 hybrids," *Chem. Sci.*, vol. 8, no. 4, pp. 3070–3079, Mar. 2017, doi: 10.1039/C6SC05219C.
[79] C. E. Lubner, R. Grimme, D. A. Bryant, and J. H. Golbeck, "Wiring Photosystem I for Direct Solar Hydrogen Production," *Biochemistry*, vol. 49, no. 3, pp. 404–414, Jan. 2010, doi: 10.1021/bi901704v.
[80] C. A. Caputo, M. A. Gross, V. W. Lau, C. Cavazza, B. V. Lotsch, and E. Reisner, "Photocatalytic Hydrogen Production using Polymeric Carbon Nitride with a Hydrogenase and a Bioinspired Synthetic Ni Catalyst," *Angew. Chem. Int. Ed.*, vol. 53, no. 43, pp. 11538–11542, 2014, doi: 10.1002/anie.201406811.
[81] W. Wang, J. Chen, C. Li, and W. Tian, "Achieving solar overall water splitting with hybrid photosystems of photosystem II and artificial photocatalysts," *Nat. Commun.*, vol. 5, no. 1, Art. no. 1, Aug. 2014, doi: 10.1038/ncomms5647.
[82] F. Zhao *et al.*, "Light Induced H2 Evolution from a Biophotocathode Based on Photosystem 1 – Pt Nanoparticles Complexes Integrated in Solvated Redox Polymers Films," *J. Phys. Chem. B*, vol. 119, no. 43, pp. 13726–13731, Oct. 2015, doi: 10.1021/acs.jpcb.5b03511.
[83] H. Shen *et al.*, "A Whole-Cell Inorganic-Biohybrid System Integrated by Reduced Graphene Oxide for Boosting Solar Hydrogen Production," *ACS Catal.*, vol. 10, no. 22, pp. 13290–13295, Nov. 2020, doi: 10.1021/acscatal.0c03594.
[84] H. Nagakawa *et al.*, "Efficient hydrogen production using photosystem I enhanced by artificial light harvesting dye," *Photochem. Photobiol. Sci.*, vol. 18, no. 2, pp. 309–313, Feb. 2019, doi: 10.1039/C8PP00426A.
[85] J. Maly *et al.*, "Reversible immobilization of engineered molecules by Ni-NTA chelators," *Bioelectrochemistry*, vol. 63, no. 1, pp. 271–275, Jun. 2004, doi: 10.1016/j.bioelechem.2003.10.024.
[86] J. Maly *et al.*, "Monolayers of photosystem II on gold electrodes with enhanced sensor response—effect of porosity and protein layer arrangement," *Anal. Bioanal. Chem.*, vol. 381, no. 8, pp. 1558–1567, Apr. 2005, doi: 10.1007/s00216-005-3149-9.
[87] N. Terasaki, M. Iwai, N. Yamamoto, T. Hiraga, S. Yamada, and Y. Inoue, "Photocurrent generation properties of Histag-photosystem II immobilized on nanostructured gold electrode," *Thin Solid Films*, vol. 516, no. 9, pp. 2553–2557, Mar. 2008, doi: 10.1016/j.tsf.2007.04.127.
[88] C. Tapia *et al.*, "Wiring of Photosystem I and Hydrogenase on an Electrode for Photoelectrochemical H2 Production by using Redox Polymers for Relatively Positive Onset Potential," *ChemElectroChem*, vol. 4, no. 1, pp. 90–95, 2017, doi: 10.1002/celc.201600506.
[89] A. Badura *et al.*, "Photo-Induced Electron Transfer Between Photosystem 2 via Cross-linked Redox Hydrogels," *Electroanalysis*, vol. 20, no. 10, pp. 1043–1047, 2008, doi: 10.1002/elan.200804191.
[90] M. Kato, T. Cardona, A. W. Rutherford, and E. Reisner, "Covalent Immobilization of Oriented Photosystem II on a Nanostructured Electrode for Solar Water Oxidation," *J. Am. Chem. Soc.*, vol. 135, no. 29, pp. 10610–10613, Jul. 2013, doi: 10.1021/ja404699h.
[91] M. Kato, T. Cardona, A. W. Rutherford, and E. Reisner, "Photoelectrochemical Water Oxidation with Photosystem II Integrated in a Mesoporous Indium–Tin Oxide Electrode," *J. Am. Chem. Soc.*, vol. 134, no. 20, pp. 8332–8335, May 2012, doi: 10.1021/ja301488d.

[92] E. Reisner, J. C. Fontecilla-Camps, and F. A. Armstrong, "Catalytic electrochemistry of a [NiFeSe]-hydrogenase on TiO2 and demonstration of its suitability for visible-light driven H2 production," *Chem. Commun.*, no. 5, pp. 550–552, Jan. 2009, doi: 10.1039/B817371K.
[93] E. Reisner, D. J. Powell, C. Cavazza, J. C. Fontecilla-Camps, and F. A. Armstrong, "Visible Light-Driven H2 Production by Hydrogenases Attached to Dye-Sensitized TiO2 Nanoparticles," *J. Am. Chem. Soc.*, vol. 131, no. 51, pp. 18457–18466, Dec. 2009, doi: 10.1021/ja907923r.
[94] I. J. Iwuchukwu *et al.*, "Optimization of photosynthetic hydrogen yield from platinized photosystem I complexes using response surface methodology," *Int. J. Hydrog. Energy*, vol. 36, no. 18, pp. 11684–11692, Sep. 2011, doi: 10.1016/j.ijhydene.2011.06.068.
[95] J. K. Hurst, "In Pursuit of Water Oxidation Catalysts for Solar Fuel Production," *Science*, vol. 328, no. 5976, pp. 315–316, Apr. 2010, doi: 10.1126/science.1187721.
[96] H. Dau and I. Zaharieva, "Principles, Efficiency, and Blueprint Character of Solar-Energy Conversion in Photosynthetic Water Oxidation," *Acc. Chem. Res.*, vol. 42, no. 12, pp. 1861–1870, Dec. 2009, doi: 10.1021/ar900225y.
[97] W. Wang *et al.*, "Spatially Separated Photosystem II and a Silicon Photoelectrochemical Cell for Overall Water Splitting: A Natural–Artificial Photosynthetic Hybrid," *Angew. Chem.*, vol. 128, no. 32, pp. 9375–9379, 2016, doi: 10.1002/ange.201604091.
[98] R. I. Pinhassi *et al.*, "Hybrid bio-photo-electro-chemical cells for solar water splitting," *Nat. Commun.*, vol. 7, no. 1, Art. no. 1, Aug. 2016, doi: 10.1038/ncomms12552.
[99] N. K. Allam, C.-W. Yen, R. D. Near, and M. A. El-Sayed, "Bacteriorhodopsin/TiO2 nanotube arrays hybrid system for enhanced photoelectrochemical water splitting," *Energy Environ. Sci.*, vol. 4, no. 8, pp. 2909–2914, Aug. 2011, doi: 10.1039/C1EE01447A.
[100] S. Balasubramanian, P. Wang, R. D. Schaller, T. Rajh, and E. A. Rozhkova, "High-Performance Bioassisted Nanophotocatalyst for Hydrogen Production," *Nano Lett.*, vol. 13, no. 7, pp. 3365–3371, Jul. 2013, doi: 10.1021/nl4016655.
[101] P. Wang, A. Y. Chang, V. Novosad, V. V. Chupin, R. D. Schaller, and E. A. Rozhkova, "Cell-Free Synthetic Biology Chassis for Nanocatalytic Photon-to-Hydrogen Conversion," *ACS Nano*, vol. 11, no. 7, pp. 6739–6745, Jul. 2017, doi: 10.1021/acsnano.7b01142.
[102] K. A. Brown, M. B. Wilker, M. Boehm, G. Dukovic, and P. W. King, "Characterization of Photochemical Processes for H2 Production by CdS Nanorod–[FeFe] Hydrogenase Complexes," *J. Am. Chem. Soc.*, vol. 134, no. 12, pp. 5627–5636, Mar. 2012, doi: 10.1021/ja2116348.
[103] T. Sakai, D. Mersch, and E. Reisner, "Photocatalytic Hydrogen Evolution with a Hydrogenase in a Mediator-Free System under High Levels of Oxygen," *Angew. Chem. Int. Ed.*, vol. 52, no. 47, pp. 12313–12316, 2013, doi: 10.1002/anie.201306214.
[104] M. B. Wilker, K. E. Shinopoulos, K. A. Brown, D. W. Mulder, P. W. King, and G. Dukovic, "Electron Transfer Kinetics in CdS Nanorod–[FeFe]-Hydrogenase Complexes and Implications for Photochemical H2 Generation," *J. Am. Chem. Soc.*, vol. 136, no. 11, pp. 4316–4324, Mar. 2014, doi: 10.1021/ja413001p.
[105] C. A. Caputo, L. Wang, R. Beranek, and E. Reisner, "Carbon nitride–TiO2 hybrid modified with hydrogenase for visible light driven hydrogen production," *Chem. Sci.*, vol. 6, no. 10, pp. 5690–5694, Sep. 2015, doi: 10.1039/C5SC02017D.
[106] G. A. M. Hutton *et al.*, "Carbon Dots as Versatile Photosensitizers for Solar-Driven Catalysis with Redox Enzymes," *J. Am. Chem. Soc.*, vol. 138, no. 51, pp. 16722–16730, Dec. 2016, doi: 10.1021/jacs.6b10146.
[107] C. Tapia, S. Zacarias, I. A. C. Pereira, J. C. Conesa, M. Pita, and A. L. De Lacey, "In Situ Determination of Photobioproduction of H2 by In2S3-[NiFeSe] Hydrogenase from Desulfovibrio vulgaris Hildenborough Using Only Visible Light," *ACS Catal.*, vol. 6, no. 9, pp. 5691–5698, Sep. 2016, doi: 10.1021/acscatal.6b01512.
[108] D. H. Nam *et al.*, "Solar Water Splitting with a Hydrogenase Integrated in Photoelectrochemical Tandem Cells," *Angew. Chem. Int. Ed.*, vol. 57, no. 33, pp. 10595–10599, 2018, doi: 10.1002/anie.201805027.

[109] K. Holá *et al.*, "Carbon Dots and [FeFe] Hydrogenase Biohybrid Assemblies for Efficient Light-Driven Hydrogen Evolution," *ACS Catal.*, vol. 10, no. 17, pp. 9943–9952, Sep. 2020, doi: 10.1021/acscatal.0c02474.

[110] L. Zhang, G. Morello, S. B. Carr, and F. A. Armstrong, "Aerobic Photocatalytic H2 Production by a [NiFe] Hydrogenase Engineered to Place a Silver Nanocluster in the Electron Relay," *J. Am. Chem. Soc.*, vol. 142, no. 29, pp. 12699–12707, Jul. 2020, doi: 10.1021/jacs.0c04302.

[111] H. Krassen, A. Schwarze, B. Friedrich, K. Ataka, O. Lenz, and J. Heberle, "Photosynthetic Hydrogen Production by a Hybrid Complex of Photosystem I and [NiFe]-Hydrogenase," *ACS Nano*, vol. 3, no. 12, pp. 4055–4061, Dec. 2009, doi: 10.1021/nn900748j.

[112] C. E. Lubner *et al.*, "Solar hydrogen-producing bionanodevice outperforms natural photosynthesis," *Proc. Natl. Acad. Sci.*, vol. 108, no. 52, pp. 20988–20991, Dec. 2011, doi: 10.1073/pnas.1114660108.

[113] C. E. Lubner, M. Heinnickel, D. A. Bryant, and J. H. Golbeck, "Wiring photosystem I for electron transfer to a tethered redox dye," *Energy Environ. Sci.*, vol. 4, no. 7, pp. 2428–2434, Jul. 2011, doi: 10.1039/C1EE01043C.

[114] K. P. Sokol *et al.*, "Bias-free photoelectrochemical water splitting with photosystem II on a dye-sensitized photoanode wired to hydrogenase," *Nat. Energy*, vol. 3, no. 11, Art. no. 11, Nov. 2018, doi: 10.1038/s41560-018-0232-y.

[115] K. P. Sokol *et al.*, "Photoreduction of CO2 with a Formate Dehydrogenase Driven by Photosystem II Using a Semi-artificial Z-Scheme Architecture," *J. Am. Chem. Soc.*, vol. 140, no. 48, pp. 16418–16422, Dec. 2018, doi: 10.1021/jacs.8b10247.

[116] F. Wang, W.-G. Wang, X.-J. Wang, H.-Y. Wang, C.-H. Tung, and L.-Z. Wu, "A Highly Efficient Photocatalytic System for Hydrogen Production by a Robust Hydrogenase Mimic in an Aqueous Solution," *Angew. Chem. Int. Ed.*, vol. 50, no. 14, pp. 3193–3197, 2011, doi: 10.1002/anie.201006352.

[117] F. Wen, X. Wang, L. Huang, G. Ma, J. Yang, and C. Li, "A Hybrid Photocatalytic System Comprising ZnS as Light Harvester and an [Fe2S2] Hydrogenase Mimic as Hydrogen Evolution Catalyst," *ChemSusChem*, vol. 5, no. 5, pp. 849–853, 2012, doi: 10.1002/cssc.201200190.

[118] Y. Honda, H. Hagiwara, S. Ida, and T. Ishihara, "Application to Photocatalytic H2 Production of a Whole-Cell Reaction by Recombinant Escherichia coli Cells Expressing [FeFe]-Hydrogenase and Maturases Genes," *Angew. Chem. Int. Ed.*, vol. 55, no. 28, pp. 8045–8048, 2016, doi: 10.1002/anie.201600177.

[119] B. Wang *et al.*, "Enhanced Biological Hydrogen Production from Escherichia coli with Surface Precipitated Cadmium Sulfide Nanoparticles," *Adv. Energy Mater.*, vol. 7, no. 20, p. 1700611, 2017, doi: 10.1002/aenm.201700611.

[120] Z. Jiang *et al.*, "AgInS2/In2S3 heterostructure sensitization of Escherichia coli for sustainable hydrogen production," *Nano Energy*, vol. 46, pp. 234–240, Apr. 2018, doi: 10.1016/j.nanoen.2018.02.001.

[121] K. Gurunathan, "Photobiocatalytic production of hydrogen using sensitized TiO2–MV2+ system coupled Rhodopseudomonas capsulata," *J. Mol. Catal. Chem.*, vol. 156, no. 1, pp. 59–67, May 2000, doi: 10.1016/S1381-1169(99)00417-3.

[122] M. Grit and D. J. A. Crommelin, "Chemical stability of liposomes: implications for their physical stability," *Chem. Phys. Lipids*, vol. 64, no. 1, pp. 3–18, Sep. 1993, doi: 10.1016/0009-3084(93)90053-6.

[123] A. Akbarzadeh *et al.*, "Liposome: classification, preparation, and applications," *Nanoscale Res. Lett.*, vol. 8, no. 1, p. 102, Feb. 2013, doi: 10.1186/1556-276X-8-102.

[124] N. P. Ulrih, D. Gmajner, and P. Raspor, "Structural and physicochemical properties of polar lipids from thermophilic archaea," *Appl. Microbiol. Biotechnol.*, vol. 84, no. 2, pp. 249–260, Aug. 2009, doi: 10.1007/s00253-009-2102-9.

[125] K. Nakayama, T. Yamaoka, and S. Katoh, "Chromatographic separation of photosystems I and II from the thylakoid membrane isolated from a thermophilic blue-green alga," *Plant Cell Physiol.*, vol. 20, no. 8, pp. 1565–1576, Dec. 1979, doi: 10.1093/oxfordjournals.pcp.a075959.

[126] J. O. Calkins, Y. Umasankar, H. O'Neill, and R. P. Ramasamy, "High photo-electrochemical activity of thylakoid–carbon nanotube composites for photosynthetic energy conversion," *Energy Environ. Sci.*, vol. 6, no. 6, pp. 1891–1900, May 2013, doi: 10.1039/C3EE40634B.
[127] R. I. Pinhassi *et al.*, "Photosynthetic Membranes of Synechocystis or Plants Convert Sunlight to Photocurrent through Different Pathways due to Different Architectures," *PLOS ONE*, vol. 10, no. 4, p. e0122616, Apr. 2015, doi: 10.1371/journal.pone.0122616.
[128] D. Pankratov, G. Pankratova, and L. Gorton, "Thylakoid membrane–based photobioelectrochemical systems: Achievements, limitations, and perspectives," *Curr. Opin. Electrochem.*, vol. 19, pp. 49–54, Feb. 2020, doi: 10.1016/j.coelec.2019.09.005.
[129] M. Rasmussen, A. Wingersky, and S. D. Minteer, "Comparative study of thylakoids from higher plants for solar energy conversion and herbicide detection," *Electrochimica Acta*, vol. 140, pp. 304–308, Sep. 2014, doi: 10.1016/j.electacta.2014.02.121.
[130] M. Rasmussen and S. D. Minteer, "Investigating the mechanism of thylakoid direct electron transfer for photocurrent generation," *Electrochimica Acta*, vol. 126, pp. 68–73, Apr. 2014, doi: 10.1016/j.electacta.2013.06.081.
[131] R. Takeuchi, A. Suzuki, K. Sakai, Y. Kitazumi, O. Shirai, and K. Kano, "Construction of photo-driven bioanodes using thylakoid membranes and multi-walled carbon nanotubes," *Bioelectrochemistry*, vol. 122, pp. 158–163, Aug. 2018, doi: 10.1016/j.bioelechem.2018.04.001.
[132] A.-I. Bunea *et al.*, "Micropatterned Carbon-on-Quartz Electrode Chips for Photocurrent Generation from Thylakoid Membranes," *ACS Appl. Energy Mater.*, vol. 1, no. 7, pp. 3313–3322, Jul. 2018, doi: 10.1021/acsaem.8b00500.
[133] G. Pankratova *et al.*, "Three-Dimensional Graphene Matrix-Supported and Thylakoid Membrane-Based High-Performance Bioelectrochemical Solar Cell," *ACS Appl. Energy Mater.*, vol. 1, no. 2, pp. 319–323, Feb. 2018, doi: 10.1021/acsaem.7b00249.
[134] H. Kanso, G. Pankratova, P. Bollella, D. Leech, D. Hernandez, and L. Gorton, "Sunlight photocurrent generation from thylakoid membranes on gold nanoparticle modified screen-printed electrodes," *J. Electroanal. Chem.*, vol. 816, pp. 259–264, May 2018, doi: 10.1016/j.jelechem.2018.03.030.
[135] C. Han *et al.*, "Organic quinones towards advanced electrochemical energy storage: recent advances and challenges," *J. Mater. Chem. A*, vol. 7, no. 41, pp. 23378–23415, Oct. 2019, doi: 10.1039/C9TA05252F.
[136] M. Havaux, "Plastoquinone In and Beyond Photosynthesis," *Trends Plant Sci.*, vol. 25, no. 12, pp. 1252–1265, Dec. 2020, doi: 10.1016/j.tplants.2020.06.011.
[137] K. H. Grumbach, "Distribution of Chlorophylls, Carotenoids and Quinones in Chloroplasts of Higher Plants," *Z. Für Naturforschung C*, vol. 38, no. 11–12, pp. 996–1002, Dec. 1983, doi: 10.1515/znc-1983-11-1220.
[138] S. Khorobrykh, T. Tsurumaki, K. Tanaka, T. Tyystjärvi, and E. Tyystjärvi, "Measurement of the redox state of the plastoquinone pool in cyanobacteria," *FEBS Lett.*, vol. 594, no. 2, pp. 367–375, 2020, doi: 10.1002/1873-3468.13605.
[139] W. Lubitz, H. Ogata, O. Rüdiger, and E. Reijerse, "Hydrogenases," *Chem. Rev.*, vol. 114, no. 8, pp. 4081–4148, Apr. 2014, doi: 10.1021/cr4005814.
[140] F. Lu, P. R. Smith, K. Mehta, and J. R. Swartz, "Development of a synthetic pathway to convert glucose to hydrogen using cell free extracts," *Int. J. Hydrog. Energy*, vol. 40, no. 30, pp. 9113–9124, Aug. 2015, doi: 10.1016/j.ijhydene.2015.05.121.
[141] N. Petrova, S. Stoichev, M. Paunov, S. Todinova, S. G. Taneva, and S. Krumova, "Structural organization, thermal stability, and excitation energy utilization of pea thylakoid membranes adapted to low light conditions," *Acta Physiol. Plant.*, vol. 41, no. 12, p. 188, Nov. 2019, doi: 10.1007/s11738-019-2979-6.
[142] M. Kato, J. Z. Zhang, N. Paul, and E. Reisner, "Protein film photoelectrochemistry of the water oxidation enzyme photosystem II," *Chem. Soc. Rev.*, vol. 43, no. 18, pp. 6485–6497, Aug. 2014, doi: 10.1039/C4CS00031E.
[143] Y. Nishiyama and N. Murata, "Revised scheme for the mechanism of photoinhibition and its application to enhance the abiotic stress tolerance of the photosynthetic machinery," *Appl.*

Microbiol. Biotechnol., vol. 98, no. 21, pp. 8777–8796, Nov. 2014, doi: 10.1007/s00253-014-6020-0.

[144] D. Dervishogullari, E. A. Gizzie, G. K. Jennings, and D. E. Cliffel, "Polyviologen as Electron Transport Material in Photosystem I-Based Biophotovoltaic Cells," *Langmuir*, vol. 34, no. 51, pp. 15658–15664, Dec. 2018, doi: 10.1021/acs.langmuir.8b02967.

[145] K. D. Wolfe, D. Dervishogullari, J. M. Passantino, C. D. Stachurski, G. K. Jennings, and D. E. Cliffel, "Improving the stability of photosystem I–based bioelectrodes for solar energy conversion," *Curr. Opin. Electrochem.*, vol. 19, pp. 27–34, Feb. 2020, doi: 10.1016/j.coelec.2019.09.009.

[146] D. Takagi, S. Takumi, M. Hashiguchi, T. Sejima, and C. Miyake, "Superoxide and Singlet Oxygen Produced within the Thylakoid Membranes Both Cause Photosystem I Photoinhibition," *Plant Physiol.*, vol. 171, no. 3, pp. 1626–1634, Jul. 2016, doi: 10.1104/pp.16.00246.

[147] Z.-H. Hu, Y.-N. Xu, Y.-D. Gong, and T.-Y. Kuang, "Effects of heat treatment on the protein secondary structure and pigment microenvironment in photosystem 1 complex," *Photosynthetica*, vol. 43, no. 4, pp. 529–534, Dec. 2005, doi: 10.1007/s11099-005-0085-z.

[148] D. O. Hall and K. Rao, *Photosynthesis*. Cambridge University Press.

[149] "Solar resource maps of Austria." https://solargis.com/maps-and-gis-data/download/austria (accessed Jun. 24, 2023).

[150] S. Alsayegh, J. R. Johnson, B. Ohs, J. Lohaus, and M. Wessling, "Systematic optimization of H2 recovery from water splitting process using membranes and N2 diluent," *Int. J. Hydrog. Energy*, vol. 42, no. 9, pp. 6000–6011, Mar. 2017, doi: 10.1016/j.ijhydene.2016.11.186.

[151] S. Alsayegh, J. R. Johnson, B. Ohs, J. Lohaus, and M. Wessling, "Systematic optimization of H2 recovery from water splitting process using membranes and N2 diluent," *Int. J. Hydrog. Energy*, vol. 42, no. 9, pp. 6000–6011, Mar. 2017, doi: 10.1016/j.ijhydene.2016.11.186.

[152] I. A. Zlochower and G. M. Green, "The limiting oxygen concentration and flammability limits of gases and gas mixtures," *J. Loss Prev. Process Ind.*, vol. 22, no. 4, pp. 499–505, Jul. 2009, doi: 10.1016/j.jlp.2009.03.006.

[153] X. Hu, Q. Xie, J. Zhang, Q. Yu, H. Liu, and Y. Sun, "Experimental study of the lower flammability limits of H2/O2/CO2 mixture," *Int. J. Hydrog. Energy*, vol. 45, no. 51, pp. 27837–27845, Oct. 2020, doi: 10.1016/j.ijhydene.2020.07.033.

[154] A. Di Benedetto, V. Di Sarli, E. Salzano, F. Cammarota, and G. Russo, "Explosion behavior of CH4/O2/N2/CO2 and H2/O2/N2/CO2 mixtures," *Int. J. Hydrog. Energy*, vol. 34, no. 16, pp. 6970–6978, Aug. 2009, doi: 10.1016/j.ijhydene.2009.05.120.

[155] V. Schroeder and K. Holtappels, "Explosion Characteristics of Hydrogen-Air and Hydrogen-Oxygen Mixtures at Elevated Pressures," *Int Conf Hydrog. Saf Pisa Italy 2005*, 2005.

[156] S. P. Medvedev, B. E. Gel'fand, A. N. Polenov, and S. V. Khomik, "Flammability Limits for Hydrogen–Air Mixtures in the Presence of Ultrafine Droplets of Water (Fog)," *Combust. Explos. Shock Waves*, vol. 38, no. 4, pp. 381–386, Jul. 2002, doi: 10.1023/A:1016277028276.

[157] P. G. Holborn, P. Battersby, J. M. Ingram, A. F. Averill, and P. F. Nolan, "Modelling the effect of water fog on the upper flammability limit of hydrogen–oxygen–nitrogen mixtures," *Int. J. Hydrog. Energy*, vol. 38, no. 16, pp. 6896–6903, May 2013, doi: 10.1016/j.ijhydene.2013.03.091.

[158] F. G. A. Fernández, J. M. F. Sevilla, and E. M. Grima, "9 Principles of photobioreactor design," in *Microalgal Biotechnology: Potential and Production*, De Gruyter, 2012, pp. 151–180. doi: 10.1515/9783110225020.151.

[159] J. Yu *et al.*, "Synechococcus elongatus UTEX 2973, a fast growing cyanobacterial chassis for biosynthesis using light and CO2," *Sci. Rep.*, vol. 5, no. 1, p. 8132, Jan. 2015, doi: 10.1038/srep08132.

[160] R. Hasan, "Growth characterization data of Synechococcus elongatus UTEX 2973 in mixed wastewater and in BG11 synthetic growth media," vol. 1, Oct. 2022, doi: 10.17632/wc4p9x5248.1.

[161] J. S. Tan *et al.*, "A review on microalgae cultivation and harvesting, and their biomass extraction processing using ionic liquids," *Bioengineered*, vol. 11, no. 1, pp. 116–129, Jan. 2020, doi: 10.1080/21655979.2020.1711626.

[162] A. Waghmare, K. Nagula, A. Pandit, and S. Arya, "Hydrodynamic cavitation for energy efficient and scalable process of microalgae cell disruption," *Algal Res.*, vol. 40, p. 101496, Jun. 2019, doi: 10.1016/j.algal.2019.101496.
[163] D. N. Dani and J. K. Sainis, "Isolation and characterization of a thylakoid membrane module showing partial light and dark reactions," *Biochim. Biophys. Acta BBA - Biomembr.*, vol. 1669, no. 1, pp. 43–52, May 2005, doi: 10.1016/j.bbamem.2005.01.001.
[164] S. K. Sahoo, "Chapter 3 - Formulation and characterization of liposomes," in *Liposomal Encapsulation in Food Science and Technology*, C. Anandharamakrishnan and S. Dutta, Eds., Academic Press, 2023, pp. 39–63. doi: 10.1016/B978-0-12-823935-3.00010-2.
[165] Z. Huang *et al.*, "Progress involving new techniques for liposome preparation," *Asian J. Pharm. Sci.*, vol. 9, no. 4, pp. 176–182, Aug. 2014, doi: 10.1016/j.ajps.2014.06.001.
[166] "POLYMUN - Excellence in Biopharmaceuticals and Liposomes, Contract Development and Manufacturing." https://www.polymun.com/liposomes/technology/ (accessed Sep. 21, 2023).
[167] D. Lombardo and M. A. Kiselev, "Methods of Liposomes Preparation: Formation and Control Factors of Versatile Nanocarriers for Biomedical and Nanomedicine Application," *Pharmaceutics*, vol. 14, no. 3, Art. no. 3, Mar. 2022, doi: 10.3390/pharmaceutics14030543.
[168] J. Miyake, M. Miyake, and Y. Asada, "Biotechnological hydrogen production: research for efficient light energy conversion," *J. Biotechnol.*, vol. 70, no. 1, pp. 89–101, Apr. 1999, doi: 10.1016/S0168-1656(99)00063-2.
[169] "eHORA - Natural Hazard Overview & Risk Assessment Austria." https://hora.gv.at/ (accessed Sep. 17, 2023).
[170] L. Vermaak, H. W. J. P. Neomagus, and D. G. Bessarabov, "Recent Advances in Membrane-Based Electrochemical Hydrogen Separation: A Review," *Membranes*, vol. 11, no. 2, Art. no. 2, Feb. 2021, doi: 10.3390/membranes11020127.
[171] B. Castro-Dominguez, P. Leelachaikul, A. Takagaki, T. Sugawara, R. Kikuchi, and S. T. Oyama, "Supported perfluorotributylamine liquid membrane for H2/O2 separation," *J. Membr. Sci.*, vol. 448, pp. 262–269, Dec. 2013, doi: 10.1016/j.memsci.2013.08.003.
[172] S. Alsayegh, J. R. Johnson, X. Wei, B. Ohs, J. Lohaus, and M. Wessling, "CO2 aided H2 recovery from water splitting processes," *Int. J. Hydrog. Energy*, vol. 42, no. 34, pp. 21793–21805, Aug. 2017, doi: 10.1016/j.ijhydene.2017.07.023.
[173] H. Xia *et al.*, "Adsorption separation of O2/N2 by Li-RHO zeolite with high oxygen selectivity," *Microporous Mesoporous Mater.*, vol. 350, p. 112442, Feb. 2023, doi: 10.1016/j.micromeso.2023.112442.
[174] X. Chen, S. Kaliaguine, and D. Rodrigue, "Correlation between Performances of Hollow Fibers and Flat Membranes for Gas Separation," *Sep. Purif. Rev.*, vol. 47, May 2017, doi: 10.1080/15422119.2017.1324490.
[175] N. F. Himma, A. K. Wardani, N. Prasetya, P. T. P. Aryanti, and I. G. Wenten, "Recent progress and challenges in membrane-based O2/N2 separation," *Rev. Chem. Eng.*, vol. 35, no. 5, pp. 591–625, Jul. 2019, doi: 10.1515/revce-2017-0094.
[176] T. Kim, Y. Song, J. Kang, S. K. Kim, and S. Kim, "A review of recent advances in hydrogen purification for selective removal of oxygen: Deoxo catalysts and reactor systems," *Int. J. Hydrog. Energy*, vol. 47, no. 59, pp. 24817–24834, Jul. 2022, doi: 10.1016/j.ijhydene.2022.05.221.
[177] G. J. Kim, J. H. Shin, and S. Chang Hong, "Study on the role of Pt and Pd in Pt–Pd/TiO2 bimetallic catalyst for H2 oxidation at room temperature," *Int. J. Hydrog. Energy*, vol. 45, no. 35, pp. 17276–17286, Jul. 2020, doi: 10.1016/j.ijhydene.2020.03.062.
[178] B. D. Mukri and M. S. Hegde, "High rates of catalytic hydrogen combustion with air over coated cordierite monolith," *J. Chem. Sci.*, vol. 129, no. 9, pp. 1363–1372, Sep. 2017, doi: 10.1007/s12039-017-1345-8.
[179] M. Yáñez, F. Relvas, A. Ortiz, D. Gorri, A. Mendes, and I. Ortiz, "PSA purification of waste hydrogen from ammonia plants to fuel cell grade," *Sep. Purif. Technol.*, vol. 240, p. 116334, Jun. 2020, doi: 10.1016/j.seppur.2019.116334.
[180] International Energy Agency, *Direct Air Capture: A key technology for net zero*. OECD, 2022. doi: 10.1787/bbd20707-en.

[181] "Weigh the benefits of on-site nitrogen generation," *Plant Engineering*, Mar. 07, 2011. https://www.plantengineering.com/articles/weigh-the-benefits-of-on-site-nitrogen-generation/ (accessed Sep. 10, 2023).
[182] F. Fritsch, "Design and Testing of a Membrane - Based Electrochemical Hydrogen Compressor." Oct. 2022.
[183] M. Mukaddam, E. Litwiller, and I. Pinnau, "Gas Sorption, Diffusion, and Permeation in Nafion," *Macromolecules*, vol. 49, no. 1, pp. 280–286, Jan. 2016, doi: 10.1021/acs.macromol.5b02578.
[184] T. Melin and R. Rautenbach, Eds., "Gaspermeation," in *Membranverfahren: Grundlagen der Modul- und Anlagenauslegung*, in VDI-Buch. Berlin, Heidelberg: Springer, 2007, pp. 447–506. doi: 10.1007/978-3-540-34328-8_13.
[185] "Wertsicherungsrechner." https://www.statistik.at/Indexrechner/Controller (accessed Sep. 11, 2023).
[186] "Listenansicht mit österreichweiten Grundstückspreisen in übersichtlicher Listenform - bodenpreise.at." https://www.bodenpreise.at/Home/List (accessed Sep. 25, 2023).
[187] S. B. Panuschka, "Universität für Bodenkultur Department für Agrarbiotechnologie Institut für Umweltbiotechnologie".
[188] "Land Oberösterreich - Was kostet ...," *Land Oberösterreich*. https://www.land-oberoesterreich.gv.at (accessed Sep. 25, 2023).
[189] C. Posten, "Design principles of photo-bioreactors for cultivation of microalgae," *Eng. Life Sci.*, vol. 9, pp. 165–177, Jun. 2009, doi: 10.1002/elsc.200900003.
[190] "LIEBHERR Gefriergerät GGPv 1470 ProfiLine Gefriergerät (3333 kWh/Jahr, 1056 l, 2120 mm hoch) online kaufen," *MediaMarkt*. https://www.mediamarkt.at/de/product/_liebherr-gefrierger%C3%A4t-ggpv-1470-profiline-1654908.html (accessed Aug. 22, 2023).
[191] D. Bathen and Breitbach, Marc, *Adsorptionstechnik : mit 141 Abbildungen*. Springer, 2001.
[192] "China molecular sieve - PSA Hydrogen Adsorber Molecular Sieve 5A Zeolite-Xintao Technology." https://www.xtadsorbents.com/psa-hydrogen-adsorber-molecular-sieve-5a-zeolite-4946.html (accessed Jul. 04, 2023).
[193] H. G. Hirschenberg, *Handbuch Verfahrenstechnik und Anlagenbau*. Springer, 1999.
[194] "Molecular sieve A5 (0.5 nm, 5 Å) 3-5 mm (0.12-0.20 in) | VWR." https://ie.vwr.com/store/product/2339087/molecular-sieve-a5-0-5-nm-5-a-3-5-mm-0-12-0-20-in (accessed Sep. 25, 2023).
[195] "CPI Inflation Calculator." https://data.bls.gov/cgi-bin/cpicalc.pl?cost1=1&year1=198601&year2=202306 (accessed Sep. 12, 2023).
[196] "NIST Chemistry WebBook." https://webbook.nist.gov/chemistry/ (accessed Sep. 13, 2023).
[197] W. Bohl and W. Elmendorf, *Strömungsmaschinen 1 - Aufbau und Wirkungsweise*, 11th ed. 2013.
[198] IEA, "Energy Technology Perspectives 2020," *Energy Technol. Perspect.*, 2020, [Online]. Available: https://iea.blob.core.windows.net/assets/7f8aed40-89af-4348-be19-c8a67df0b9ea/Energy_Technology_Perspectives_2020_PDF.pdf
[199] I. Weiner *et al.*, "Overcoming the expression barrier of the ferredoxin-hydrogenase chimera in Chlamydomonas reinhardtii supports a linear increment in photosynthetic hydrogen output," *Algal Res.*, vol. 33, pp. 310–315, Jul. 2018, doi: 10.1016/j.algal.2018.06.011.

Table of Figures